NTNU
Norwegian University of
Science and Technology

Master's thesis

2021

Arsène Amoureux

Master's thesis

NTNU
Norwegian University of
Science and Technology
Faculty of Engineering
Department of Marine Technology

Arsène Amoureux

Linear analysis and multidisciplinary design optimization of the floater OO-Star

June 2021

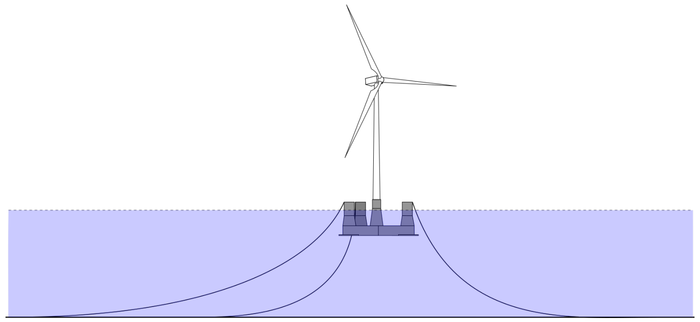

NTNU
Norwegian University of
Science and Technology

NTNU

Norwegian University of
Science and Technology

Linear analysis and multidisciplinary design optimization of the floater OO-Star

Arsène Amoureux

Marine Structures
Submission date: June 2021
Supervisor: Erin Bachynski-Polić

Norwegian University of Science and Technology
Department of Marine Technology

Department of Marine Technology - NTNU

Linear analysis and multidisciplinary design optimization of the floater OO-Star

Arsène Amoureux

Supervisor: Erin Bachynski-Polić

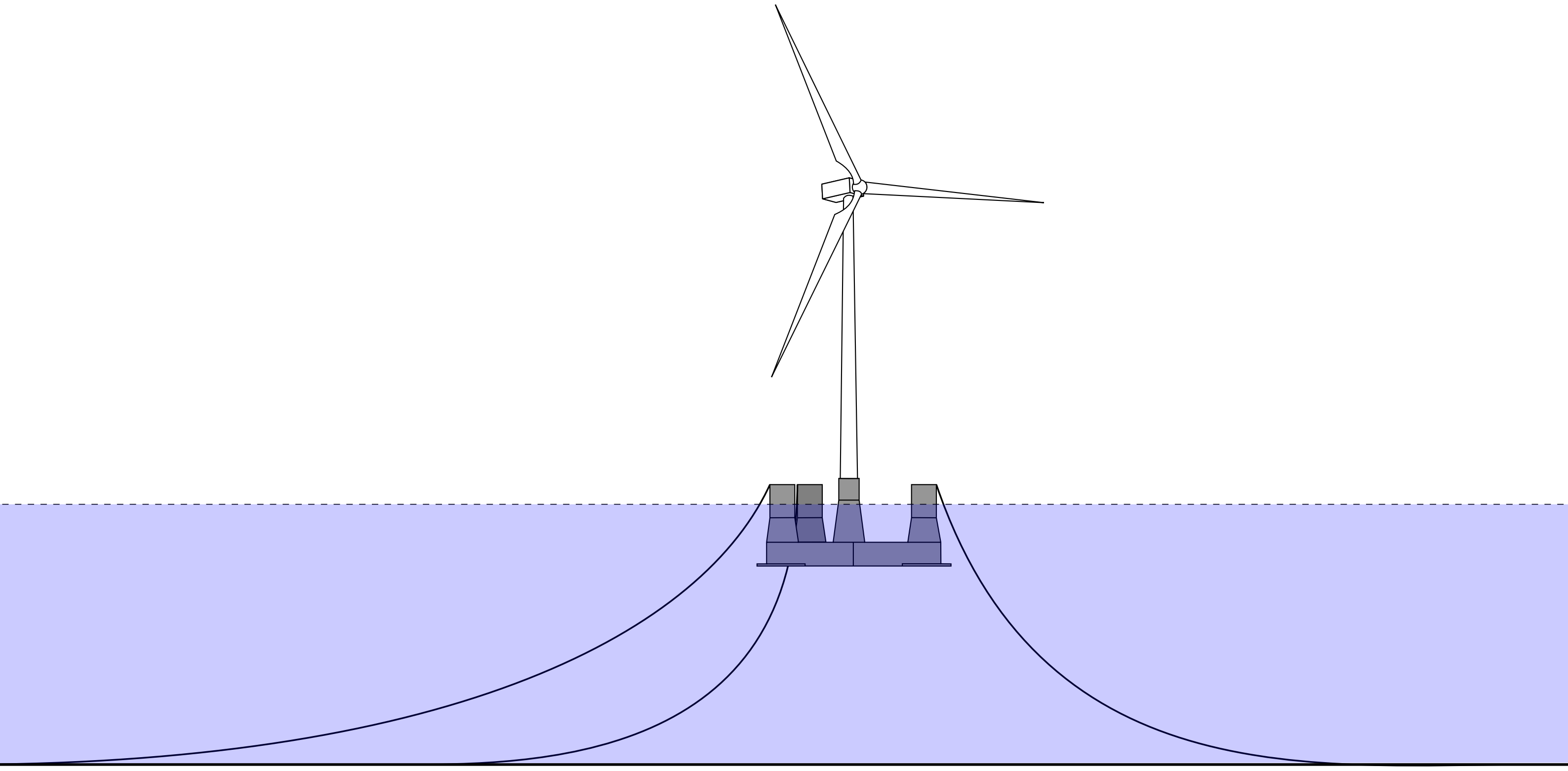

June, 2021

Abstract

In this report, in the continuity of B.de Renty's Master's thesis de Renty (2020), a linear framework for the analysis and the optimization of floating wind turbines with automated diffraction/radiation computations, is proposed. A trial example is built for a simple spar floater with two design variables. Then, a linearized model of a semi-submersible floating wind turbine based on the geometry of the floater OO-Star – for which most technical documents are availabe thanks to the project LIFES 50+ – and mounted by the DTU 10 MW turbine is being studied. The implementation is made within the framework OpenMDAO. A modal approach is set up, relying on the first three non-orthogonal modes of the stucture, namely surge, pitch and the first bending mode of the tower. The agreement between the eigenfrequencies obtained from this formulation and those computed in a more classical way is good. The aerodynamics is modelled through BEM method and effective wind speeds to account for rotor frequency and blade passing effects. A first order PI controller is used for monitoring the blade pitch angle above rated wind speed. Response spectra are compared to those computed by SIMA from one-hour time domain simulations, for three different geometries of the floater and three environmental conditions. Good trends are observed but the lack of aerodynamic damping due to the simple controller, the overestimation of the 3P excitation associated with effective wind speed formulation and the too simple mooring model lead to overestimations in surge, pitch and tower bending stress. Two design variables are selected and are used to perform an exploration of the design space, where good trends are captured with the same overestimations as for the response spectra. Some elements to improve the model are proposed in the end. In the future, such a tool could help in the first design phase of any new floater.

Table of Contents

List of Figures

List of Tables

1 Introduction

In our modern world threatened by resource depletion and climate change and which has been relying on fossil fuels for the last centuries, the need for carbon-neutral energy production systems is indisputable. Two subcategories of energies stand out at that point: nuclear power and renewable energies. For the latter, these energies – which are all subproducts of solar energy– are available at different rates; their distribution is shown in figure 2.

The development of large scale wind energy extractors, most commonly called wind turbines, started some years ago on land. Offshore wind turbines have then started to emerge, first as bottom fixed systems. But the will to harness even better winds – that is to say stronger and more regular– has led to a great enthusiasm towards floating solutions. A few designs are under development across the world and so far only two commercial or pre-commercial floating wind farms have been installed: namely Hywind Scotland from Equinor and WindFloat Atlantic from Principle Power.

This technology being still in its maturation phase, it requires efforts to become a competitive alternative to carbon intensive energy production systems, and therefore to find its developpers. A first way to reduce the share of the installation cost in the total cost, and therefore to decrease the levelized cost of energy (LCoE), is to scale up the turbines. The largest so far installed have a rated power of 8.3 MW (WindFLoat), but larger turbines have already been designed, like Haliade-X, a 12 MW turbine from General Electrics, and some even larger ones are planned. In order to support these huge converters, one needs larger substructures, which will therefore be exposed to larger loads, and will lead to new challenges as for the manufacturing and the installation. Knowing that the cost of the substructure represents from 15% to 30% of the total CAPEX of a floating wind turbine (FWT) (see Ashuri et al. Ashuri et al. (2016)), one can see the importance of designing cheaper platforms without impairing their performance.

This is where optimization comes into play. Its use in numerical models offers a powerful tool to design structures in a cost-efficient way.

A first approach to find an optimal design is to perform a parametric study, that is to say an overview of the design space defined by a set of parameters initially chosen. In this manner, Tracy Tracy (2007) explored a variety of FWT designs by mean of frequency analyses. Bachynski and Moan Bachynski and Moan (2012) also performed a parametric study of tension leg platforms (TLP), distinguishing five different designs and featuring fully coupled time-domain simulations. One of the early attempts to optimize large floating structures giving prominence to actual computer-aided optimization techniques is due to Clauss and Birk G.F.Clauss and L.Birk (1996), who made use of an adaptation of the so-called "Direct Search Method", a gradient-free algorithm, to reduce the motions and the loads exerted on three main types of offshore structures: TLPs, semisubmersibles and gravity base structures. More recently but in the same field, Park et al. Park et al. (2015) performed a multi-objective design optimization of a floating production unit using simulated annealing method so as to reduce its motions. The objective is a weighted function of the 3h heave most probable extreme value and the structural weight.

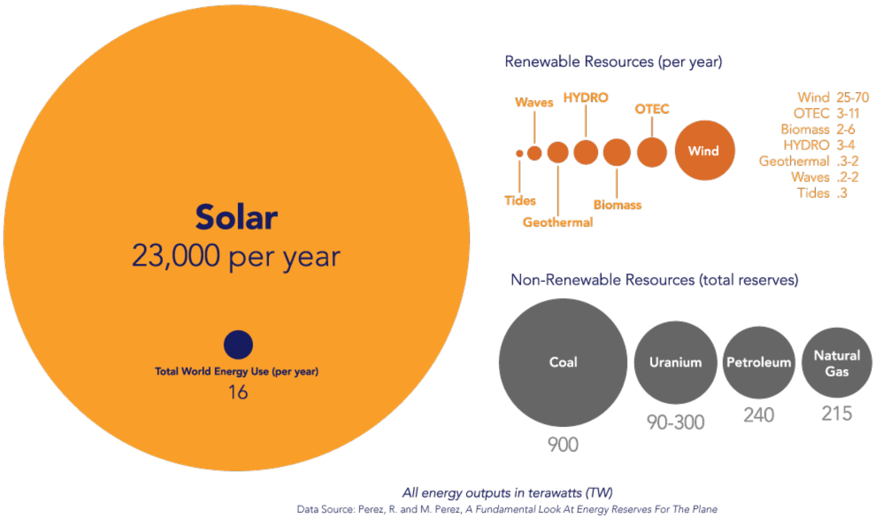

All energy outputs in terawatts (TW)

Data Source: Perez, R. and M. Perez, *A Fundamental Look At Energy Reserves For The Plane*

Figure 2: Finite and renewable planet energy reserves as of 2015 (from Perez and Perez (2015), rendered by freeingenergy.com)

Moving to wind turbines (WT), Karimi et al. Karimi et al. (2017) explored the three stability classes of FWTs through the use of a spar, a TLP and a semisubmersible platform parametrized by nine design variables. An objective function accounting for respectively the cost of both the platform and the mooring system and the fore-aft nacelle acceleration, is used. The optimization on this linearized model is performed by a genetic algorithm and Pareto fronts are discussed. Häfele and Rolfes Häfele and R.Rolfes (2016) used a particle swarm algorithm in order to reduce the cost of a jacket substructure for the NREL 5 MW turbine, sumbmitted to some equality constraints with regards to utilization factors. Despite promising results, their methodolgy is computationally very expensive.

There are only a few attempts in the field of FWT optimization which have been performed through gradient-based methods, which are known to be fast and efficient when the number of design variables is large, as long as analytical derivatives are provided and when the design space does not display too many local minima. One attempt is from Chew et al. Chew et al. (2015). In their paper, a jacket substructure is optimized according to 22 design variables selected to be the diameters and thicknesses of the jacket members. The optimization is performed by the Sequential quadratic programming (SQP) method and both ULS and FLS criteria are checked, with two different load cases. The gradients are computed analytically by mean of the analytical direct differentiation method (DDM). Another use of a gradient-based algorithm was made by Fylling and Berthelsen Fylling and Berthelsen (2011), who optimized the shape, power cables and mooring lines of a spar buoy, with gradients computed by finite differences. The objective function was the total price of these three elements.

The previous studies which have been highlighted focused on the design of the platform and/or its mooring lines, disregarding the behaviour of the tower, control system and rotor. Now, to predict more accurately the global response of the system, coupling effects between the floater, the tower, the controller and the blades (hydro-aero-servo-elastic models) have to be taken into account. Lemmer et al. Lemmer et al. (2017) performed the optimization of the INNWIND.EU TripleSpar concept floater by mean of the gradient-free Pattern Search method, including a self-tuning controller. The objective was a combination of damage-equivalent loads and capital expenditure (CAPEX). Sandner et al. Sandner et al. (2014) achieved an integrated optimization of a set of spar-type FWTs featuring a PI-controller. The optimal configuration was found throughout a stepwise narrowing of the design space. The cost function is a linear combination of standard deviation of the rotor speed and the standard deviation of the tower bending degree of freedom (dof), which accounts for stress in the tower.

In Ashuri et al. (2014), Ashuri et al. made use of the OpenMDAO framework to carry out the optimization of the 5 MW NREL wind turbine, accounting for the aerodynamic and structural design of the rotor and tower simultaneously. Their work led to a decrease by 2.3% of the LCoE for a turbine located in a representative site in the Netherlands.

Even closer to our scope, Hegseth et al. Hegseth et al. (2020a) developed an aero-hydro-servo-elastic model of a 10 MW spar FWT to perform an integrated design optimization of the platform, tower, mooring system and blade pitch controller. The importance of the integrated formulation is highlighted in the results for the tower and the controller, affected by the design of the platform. This model is able to capture reasonably well the trends compared to nonlinear time-domain analyses, but it is restricted to this type of geometry, for which the hydrodynamic behaviour is rather simple.

The aim of this peoject is to extrapolate this methodology to semi-submersibles, which requires a more refined approach for the hydrodynamics. The floater OO-Star from the company Dr.Techn.Olav Olsen AS will be the basis for the analyis. It carry the DTU 10 MW reference wind turbine.

2 Theoretical aspects for the design of FWT

This section aims at giving an updated insight on the technology of floating offshore wind turbines (FOWTs) and at developing on key theoretical aspects which will be used as a base for this work.

In a first part, a literature review about the different concepts of FOWTs will be addressed.

Then, some theoretical hydrodynamic elements will be explained in details. A special focus will be made on potential flow theory and dynamic modelling.

Later, some aspects of multidisciplinary design optimization (MDO) will be reviewed and explained.

2.1 A review of FOWT concepts

The main feature of FOWTs – which makes them a big center of interest nowadays – is their ability to be installed in deeper water than their bottom fixed counterparts which cannot be installed in some coasts, such as US west coast are also Japan coast. Besides, larger water depth is often associated with larger distance from the shore, and therefore increased wind quality.

This technology borrows a lot from oil&gas engineering, which started designing offshore oil rigs in the beginning of 20^{th} century (first offshore oil rig, Ferry Lake No.1, built in 1911), and has therefore accumulated knowledge on offshore structures. Logically, as mentioned by Butterfield et al. Butterfield et al. (2005) these two industries face a lot of common challenges, but their respective priorites and drivers are different however.

The reason why the design of these structures is challenging is their exposition to a large variety of loads, as presented in figure 3, most of which are nonlinear and feature very disparate probabilities of occurence.

It is however still possible to analyze such structures globally first, in order to categorize different classes of designs. The most common criteria used to distinguish subcategories of floaters is the way they achieve static stability to overcome the thrust force being applied on the rotor. From conventional static analysis of marine structures, one knows that a requirement for static stability around a given x axis is that the metacentric height GM of the floating structure is positive. It is given by the following equation:

$$GM = KB + BM - KG, \text{ with } BM = \frac{I_{xx}}{\nabla}, \tag{2.1}$$

where I_{xx} is the second moment of area along x axis and ∇ is the displacement of the structure.

Butterfiel et al. Butterfield et al. (2005) proposed three means by which offshore

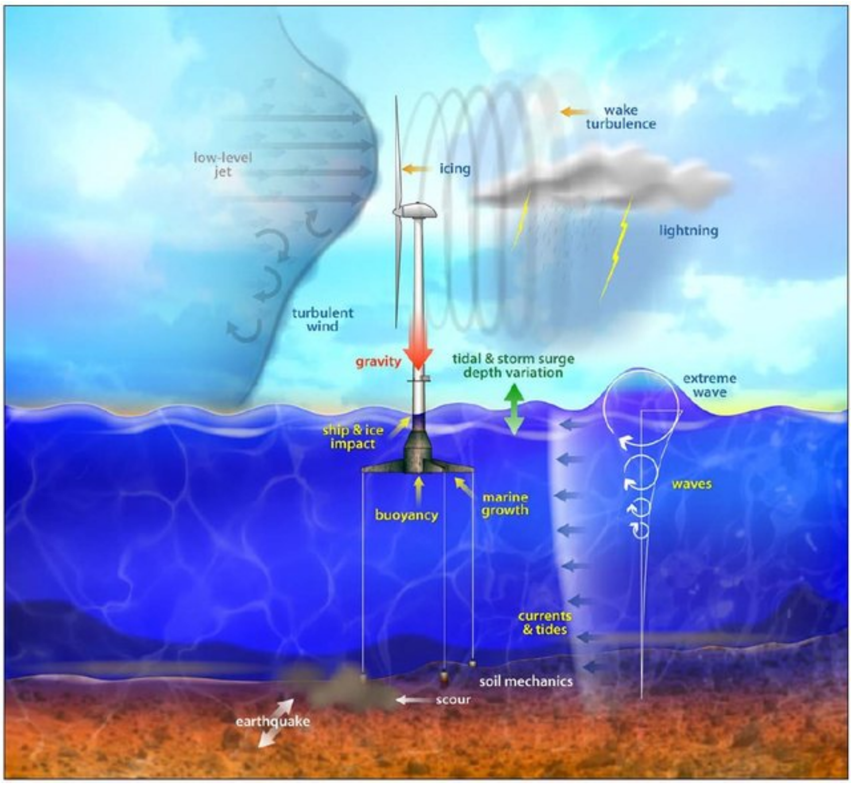

Figure 3: Loads on a FOW (Credits: J.Jonkman, NREL)

platforms perform static stability; you can refer to figure 4 to get an illustration of these concepts.

- Ballasts: heavy weight placed at the bottom of the structure such that its center of gravity is located under its center of buoyancy, conferring of righting moment that ensures high inertia for pitch and roll motions. In addition, the draft of these structures is large enough to reduce wave excitation in heave. A typical example for such platforms is the spar concept.
- Mooring lines: platforms featuring this technology rely on the tension of mooring lines, which provide them with increased stiffness for their motions. The leading concept for this type of platforms is called ”Tension Leg Platforms” (TLP). Equation 2.1 does not apply in this case because of the new location of the center buoyancy
- Buoyancy: This concept relies on a large, or at least distributed, waterplane area which confers large restoring forces to the platform.

Jonkman and Matha compared the fully-coupled dynamic responses of a barge, a TLP and a spar with a land-based NREL 5 MW in J.M.Jonkman and D.Matha (2011). The study highlights the increased ultimate and fatigue loads undergone by the floating concepts compared to their land-based counterparts due to dynamic coupling between the platform motions and the turbine. Some instable behaviours were also reported and need to be addressed. Consequently, FWT have to be de-

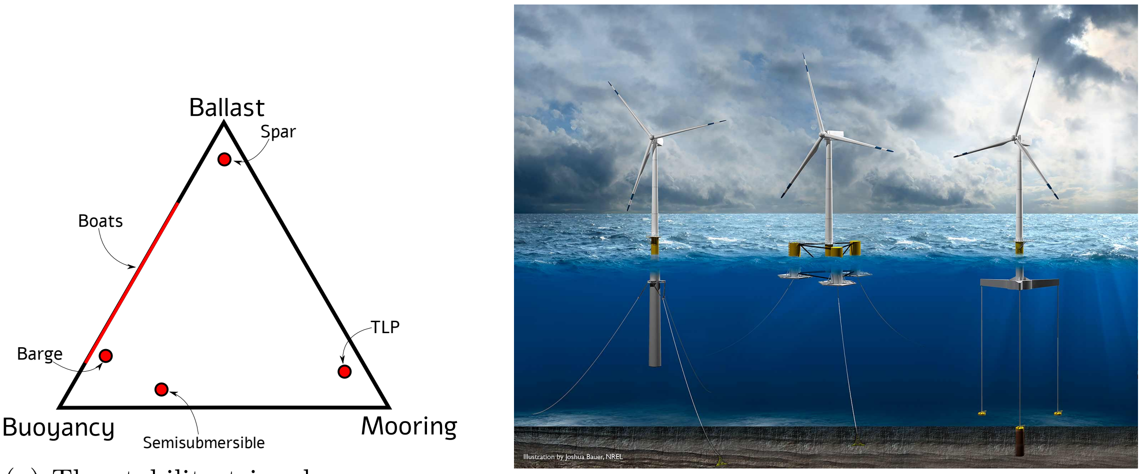

(a) The stability triangle (Credits: Thiagarajan and Dagher (2014))

(b) FOWT main concepts (Credits: J.Bauer, NREL)

Figure 4: Design parameters for FOWT

signed in a stronger way than land-based ones; one then needs to know which parts to modify and to what extent so as to deliver safe and cost-efficient technologies.

2.2 Design guidelines/practices

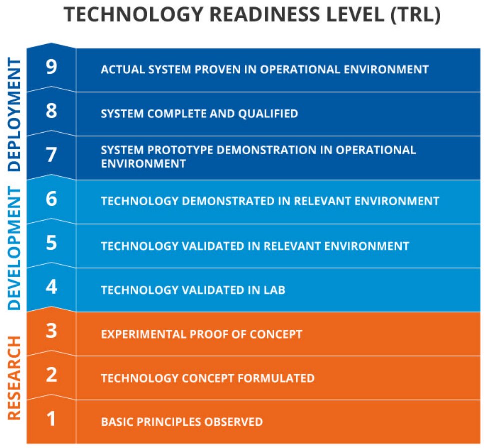

Figure 5: Description of the 9 steps of the TRL indicator (Credits: TWI)

LIFES50+ was a collaborative program initiated by SINTEF Ocean and funded by European Union throughout the project "Horizon 2020". Its aims was to select two concepts of platform with a technology readiness level (TRL) of 5 (see figure 5) mounted with a 10 MW turbine to reduce production, installation and operational and maintenance (O&M) costs. The focus was made on turbines installed at water depths ranged from 50 m to 200 m. It resulted in a large number of deliverables which provide design drivers for FWT concepts and therefore an increased scientific and industrial knowledge on numerical and experimental design methodologies.

In particular, an extensive use of deliverable D4.5 A.Pegalajar-Jurado et al. (2018) will be made, as it provides key elements for the present study.

Most commonly, the driving parameter for the design of FWT is the so-called Levelized Cost of Energy (LCoE). The details to compute this parameter, which characterizes the economic efficiency of a power system, can be found in deliverable D2.2 Benveniste et al. (2016). For a given lifetime n in years, the LCoE is computed according to:

$$LCoE = \frac{\text{Life cycle cost}}{\text{Electrical energy provided}} = \frac{C_0 + \displaystyle\sum_{t=1}^{n} \frac{O\&M_t}{(1+r)^t} + \frac{D}{(1+r)^n}}{\displaystyle\sum_{t=1}^{n} \frac{E_t - L_t}{(1+r)^t}}, \tag{2.2}$$

where C_0 is the initial investment in the power plant (capital cost), t is the time in years, $O\&M_t$ represents the O& M cost at year t, D is the decommissioning cost, E_t is the total energy generated during year t, L_t the energy loss during generation, collection and transmission at year t. Due to economic inflation, the value of money decreases with time, which is represented by the discount rate r such that $V_t = \frac{V_0}{(1+r)^t}$ where we denote the value V_t at year t.

2.3 Numerical modelling of FWT

To avoid expensive infrastructures to perform analyses of a FWT concept, any designer needs appropriate numerical tools thanks to which a numerical model will be built and extensively used (even though for the last stage of the design process, experimental validations are required).

2.3.1 Hydrodynamic modelling

Most commonly, a first approach to model the hydrodynamics of a given floater is by mean of first order potential flow theory for large structures such as semi-submersibles and barges, or using MacCamy&Fuchs formula for simple cylindrical geometries such as spars (see Hegseth et al. (2020a) as an example). For slender structures such as mooring lines, Morison equation is widely used.

To check the importance of higher order effects on the design, higher order formulations of potential flow theories are available; the second order formulation is the most common application of hydrodynamic nonlinearities and causes additional excitations of the structure due to sum and difference frequency effects.

Ultimately, viscous effects are mostly accounted for by Morison's drag term.

2.3.2 Aerodynamic modelling

The standard procedure for aerodynamic modelling is to use Blade Element Momentum (BEM) method which is based, on the one hand, on the conservations of mass, momentum and mechanical energy of the steady-state, homogeneous and incompressible air flow crossing a rigid actuator disk corresponding to the rotor of the turbine, and on the other hand on the local study of a strip of the same disk. The iterative combination of the two enables one to update the induced velocity, angle of attack and force coefficients on the blades. Four main corrections are applied to account for the 3D effects at the tip of the blades, du to the finite number of blades (Prandtl's correction), the compressibility of air (Glauert's correction), vortex shedding causinga a time lag in the change of the induced velocity (dynamic wake) and finally transient dynamic behaviours for fast-pitching blades (dynamic stall). Generalized dynamic wake, which relies on Euler's equations and a potential modellization of the pressure field can be an alternative. Finally, tower shadow effects should preferably be incorporated in the model to account for the velocity loss in the inlet velocity field close to the tower.

BEM theory This section is described in details in Hansen (2015).

BEM considers an homogeneous, incompressible flow in a steady-state. No frictional drag is taken into account and the rotor is assimilated to a disk (which is to say that it features an infinite number of blades, as displayed in figure 6). Two factors are used, which are mentioned as "induction factors" (respectively axial (or normal) and angular (or tangential)):

$$a_n = \frac{v_0 - v_A}{v_0}, \quad a_t = \frac{\omega}{2\Omega} \tag{2.3}$$

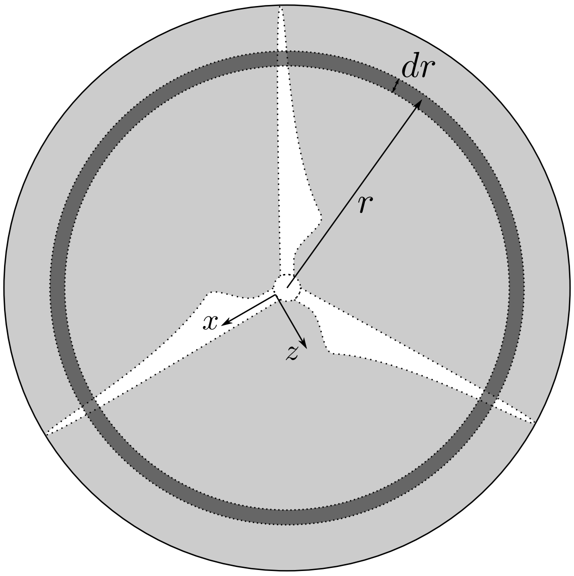

Figure 6: Description of the rotor in BEM

where v_A is the horizontal velocity of the air flow at an infinitesimal distance in front of the rotor, ω is the angular velocity of the wake behind the turbine, and Ω is the rotor angular velocity.

They define together with the wind velocity v_0 and the velocity of the strip dr the induced velocity W and the angle ϕ, sum of the local angle of attack, blade pitch angle and local twist angle, as defined in figure 7:

$$\phi = \arctan \frac{(1 - a_n)v_0}{(1 + a_t)r\omega}. \tag{2.4}$$

Then, combining a global analysis of the rotor based on the conservations of mass, momentum and mechanical energy with a local analysis of a blade strip, two new expressions are found for the two induction factors:

$$a_n = \frac{1}{\dfrac{4\sin^2\phi}{\sigma C_n} + 1}, \quad a_t = \frac{1}{\dfrac{4\cos\phi\sin\phi}{\sigma C_t} + 1}, \tag{2.5}$$

where $\sigma = Bc/2\pi r$ the solidity ratio (B the number of blades, c the local chord), $C_n = C_L \cos\phi + C_D \sin\phi$ and $C_t = C_L \sin\phi - C_D \sin\phi$ (C_L and C_D being the lift and drag coefficients).

The BEM iterative process is then described by:

- Guess a_n and a_t;
- find ϕ with 2.4 and the associated α;
- look for $C_L(\alpha)$ and $C_D(\alpha)$ in look-up tables;

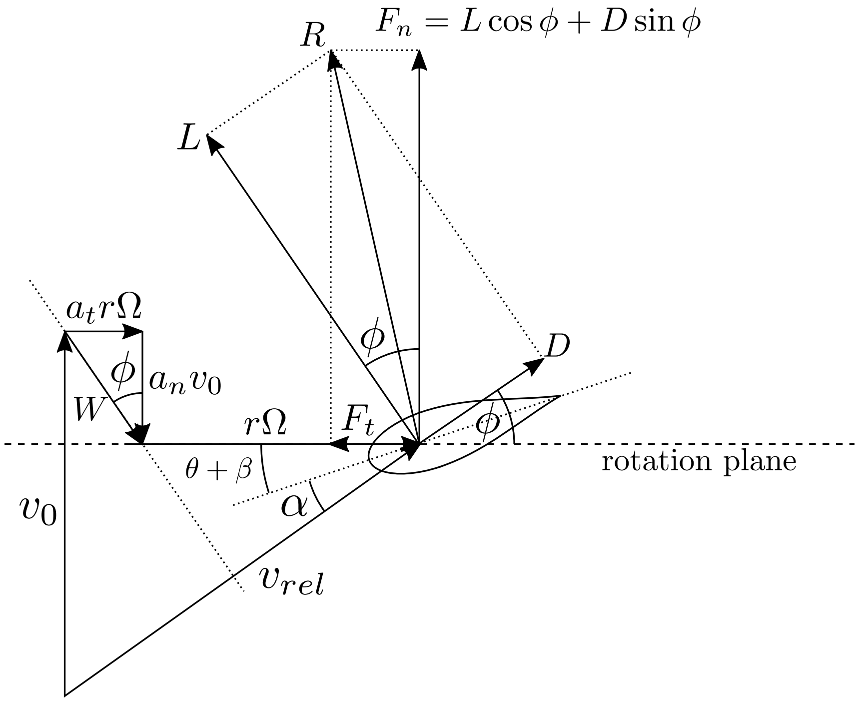

Figure 7: Velocity triangle for BEM (adapted from Hansen (2015))

- recompute a_n and a_t based on 2.5;
- compare them with the initial value and repeat until convergence.

Then, lift and drag forces (per unit span length) on the rotor can be accessed by

$$L = \frac{1}{2}\rho c v_{rel}^2 C_L(\alpha), \;\; D = \frac{1}{2}\rho c v_{rel}^2 C_D(\alpha), \tag{2.6}$$

and the normal and tangential forces on the rotor are found through

$$F_n = L\cos\phi + D\sin\phi, \;\; F_t = L\sin\phi - D\cos\phi. \tag{2.7}$$

2.3.3 Structure modelling

Very commonly, the floater is assumed to be a rigid body.

However, for an extensive analysis, finite element models –based on equilibrium between internal and external loads – are applied. The accuracy of the study notably depends on the type of elements used to describe the structure (truss, beams, shells), their order (linear, quadratic, higher orders), their density and whether or not nonlinear effects are accounted for (geometry dependent stiffness, plastic deformations, nonlinear boundary conditions).

2.4 Potential flow theory

In this study, the hydrodynamic loads and the wave kinematics will be computed by mean of potential flow theory (PFT), very well documented in Molin (2002). This theory defines a linear framework for the hydrodynamics and relies on two main assumptions:

- The fluid is incompressible, therefore with zero divergence: $\overrightarrow{\nabla}.\vec{v} = 0$
- The flow is irrotational: $\overrightarrow{\nabla} \wedge \vec{v} = \vec{0}$

The immediate consequence of these assumptions, under the relation $\Delta = \overrightarrow{\nabla} \cdot \overrightarrow{\nabla}$, is the disregard of the viscosity of the fluid, intervening in the term $\eta \overrightarrow{\Delta} \vec{v}$ in the equation of conservation of momentum. This framework therefore leads in particular to not considering the effects of recirculations in the flow.

The Helmholtz-Hodge Theorem, which states that for any vector field $\vec{A}$ – fulfilling certain hypotheses tested here – there is a vector field $\overrightarrow{\psi}$ and a scalar field ϕ such that $\vec{A} = \overrightarrow{\nabla} \wedge \overrightarrow{\psi} - \overrightarrow{\nabla}\phi$, leads to the fact that the velocity $\vec{v}$ of the flow derives from a scalar potential ϕ: $\vec{v} = -\overrightarrow{\nabla}\phi$.

This theory being applied to water in the present case, which is assumed incompressible and homogeneous, the continuity equation $\frac{\partial \rho}{\partial t} + \overrightarrow{\nabla} \cdot (\rho \vec{v}) = 0$ becomes $\overrightarrow{\nabla} \cdot \vec{v} = 0$. Using the potential introduced previously, we get the governing equation of potential flow theory:

$$\Delta \phi = 0. \tag{2.8}$$

The present study focuses on a structure of such dimensions that the Keulegan-Carpenter number ($K_C = \frac{UT}{D} = 2\pi \frac{A}{D}$ at the free surface) is small enough to keep the flow attached and justifies the use of the potential theory.

2.4.1 Diffraction-radiation problem

The objective here is to get analytical expressions for the free surface elevation, the pressure field and the velocity field, and in a second time, the loads on the floating structure. In order to achieve it, the problem is posed as illustrated by figure 8.

Boundary conditions Two conditions need to be fulfilled at the free surface:

- A fluid particle on the free surface remains on the free surface (kinematic free surface boundary condition (KFSBC)).

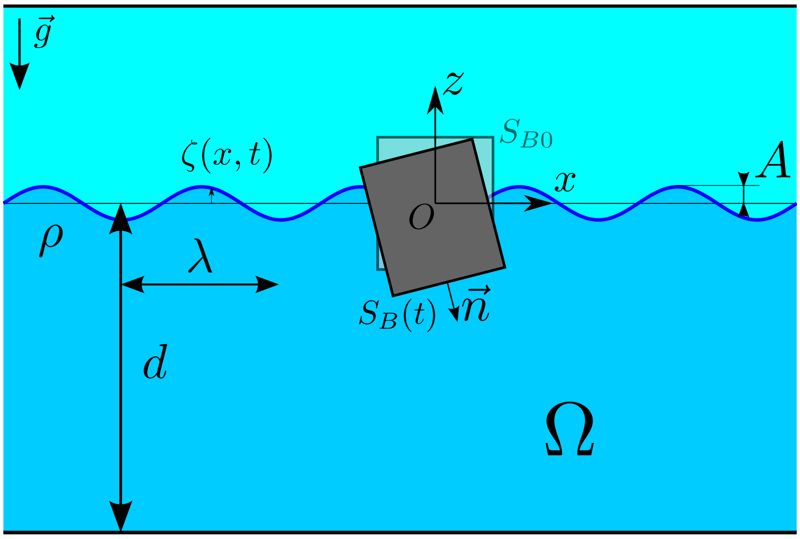

Figure 8: Definition of the environment

- Assuming negligible surface tension effects, the pressure is continuous across the free surface (dynamic free surface boundary condition (DFSBC)).

On the body surface, the normal velocity of the fluid should equal the one of the body. At the sea bed, the vertical velocity is required to be null.

Boundary value problem Then, the following set of equations is obtained:

$$\begin{cases} \Delta\phi = 0 & \forall (x,z) \in \Omega \quad \text{Laplace's equation} \\ \dfrac{\partial \phi}{\partial t} = -g\zeta - \dfrac{1}{2}|\vec{\nabla}\phi|^2 + c(t) & \text{at } z = \eta(x,t), \quad \text{DFSBC} \\ \dfrac{\partial \phi}{\partial z} = \dfrac{\partial \zeta}{\partial t} + \vec{\nabla}\phi \cdot \vec{\nabla}\zeta & \text{at } z = \zeta(x,t), \quad \text{KFSBC} \\ \dfrac{\partial \phi}{\partial z} + \vec{\nabla}\phi \cdot \vec{\nabla} d = 0 & \text{at } z = -d(x) \quad \text{bottom boundary condition} \\ \vec{\nabla}\phi \cdot \vec{n} = v_n & \text{on } S_B(t) \quad \text{body boundary condition} \end{cases} \tag{2.9}$$

where v_n is the body along its local normal direction.

Linearization of the system of equations For linearization to be valid some new assumptions are added and presented below:

- The waves are periodic in space (wave number k) and in time (frequency ω); in this precise case for which we focus on the plane (x, z), the spatial periodicity is a periodicity along x;

- the waves are propagating in the positive x-direction;
- the water depth is constant;
- the steepness is small ($\epsilon = kA \ll 1$) and the depth is sufficiently large (dispersion parameter $\mu = kd \geq O(1)$);
- the motions of the body are small compared to the wave length.

After Taylor-expanding the free surface operators and the body boundary conditions respetively at the mean water level $z = 0$ and on the mean body position S_{B0} , using perturbation series with regard to the steepness ϵ of the potential ϕ and the wave elevation ζ, and only keeping the first order terms ($\propto \epsilon$), these assumptions lead to the following linearized boundary value problem:

$$\begin{cases} \Delta\phi = 0 & \forall(x,z) \in \Omega \\ \dfrac{\partial^2\phi}{\partial t^2} + g\dfrac{\partial\phi}{\partial z} = 0 & \text{at } z = 0 \\ \dfrac{\partial\phi}{\partial z} = \dfrac{\partial\zeta}{\partial t} & \text{at } z = 0 \\ \dfrac{\partial\phi}{\partial z} = 0 & \text{at } z = -d \\ \vec{\nabla}\phi \cdot \vec{n}_0 = v_n & \text{on } S_{B0} \end{cases} \tag{2.10}$$

Now, taking advantage of the linearity of the problem, the potential is dicomposed as a sum of an incident, a scattered and a radiated potentials (see figure 9 from Faltinsen):

$$\phi = \phi_0 + \phi_S + \phi_R. \tag{2.11}$$

The radiated potential is, in turn, broken down into six components corresponding to the six degrees of freedom of the floating rigid body:

$$\phi_R = \sum_{i=1}^{6} \phi_i. \tag{2.12}$$

This way, the last equation of our system, only applied to ϕ_S and ϕ_R reads:

$$\vec{\nabla}\phi_p \cdot \vec{n}_0 = v_{n,p} \quad p = S, \{1, ..., 6\} \tag{2.13}$$

where $v_{n,D} = 0$ and $v_{n,i} = \dot{\eta}_i N_{0,i}$, defining $\vec{N}_0$ as the generalized normal for one point

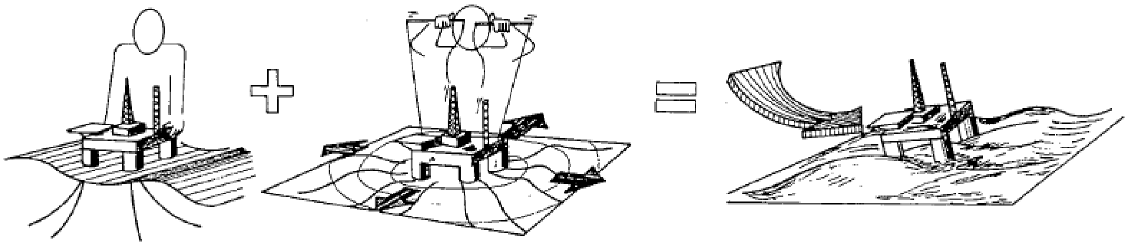

Figure 9: Illustration of the diffraction-radiation problem (Credits: Faltinsen (1993))

(x,y,z) of the structure in the reference frame $Oxyz$ and η_i its i^{th} degree of freedom.[1]

Solving this system for the incident flow, analytical expressions for the velocity and pressure fields can be found, in addition to the free surface elevation:

$$\phi_I(x,z,t) = \frac{Ag}{\omega}.\frac{\cosh k(z+d)}{\cosh kd}\sin(kx-\omega t) \tag{2.14}$$

$$\zeta(x,t) = A\cos(kx-\omega t) \tag{2.15}$$

$$p(x,z,t) = -\rho g z + A\rho g\frac{\cosh k(z+d)}{\cosh kd}\cos(kx-\omega t) \tag{2.16}$$

with $k = 2\pi/\lambda$ the wave number.

2.4.2 Wave loads

In this section, developments regarding the computation of the loads within potential flow theory will be made.

In linear theory, loads are computed by integrating the pressure field surrounding the body on its initial surface S_{B0} (as opposed to the instantaneous surface $S_B(t)$ which would result in higher order loads):

$$\vec{F}_{hydro} = \iint_{S_{B0}} -\rho\left(gz + \frac{\partial\phi}{\partial t}\right)\vec{n}dS \tag{2.17}$$

Practically, to perform the calculation for a structure with an arbitrary shape, one needs to develop a computational procedure, the most famous of which is called BEM.

---

[1] $\vec{N}_0 = \begin{bmatrix} n_{0x} \\ n_{0y} \\ n_{0z} \\ yn_{0z} - zn_{0y} \\ zn_{0x} - xn_{0z} \\ xn_{0y} - yn_{0x} \end{bmatrix}$

Panel method/Boundary element method (BEM) The principle behind this method is the modelization of the flow by a distribution of elementary potentials (so-called "singularities") which satisfy Laplace's equation; the most classical ones are sources, sinks and dipoles. For the sake of simplicity, only sources will be used to illustrate the method. The geometry of the body is split into a given number N of triangles or quadrilaterals, defining the aforementioned panels. Over each of them, the potential of the flow is assumed constant and satisfies a set of integral equations based on Green's theorem, that are discretized and presented below. Because of the harmonic time-dependence of the velocity potential ϕ, it will be treated as a complex valued time-independent potential φ such that:

$$\phi(t) = \Re\left(\varphi e^{i\omega t}\right) \tag{2.18}$$

with ω the frequency of the incident wave, $i^2 = -1$ and t the current time.

For the radiation potential, the discretized integral equation reads:

$$2\pi\varphi\left(\vec{x}_i\right) + \sum_{k=1}^{N} D_{ik}\varphi_k = \sum_{k=1}^{N} S_{ik}\left(\frac{\partial\varphi}{\partial n}\right)_k \tag{2.19}$$

while for the total diffraction potential $\varphi_D = \varphi_0 + \varphi_S$:

$$2\pi\varphi\left(\vec{x}_i\right) + \sum_{k=1}^{N} D_{ik}\varphi_k = 4\pi\varphi_0\left(\vec{x}_i\right) \tag{2.20}$$

where $i \in \{1, ..., N\}$, $\vec{x}_i$ is the collocation point for quadrilateral i, i.e. the point at which the integral equations are enforced, taken as the centroid of the panel.

The two matrices D_{ik} and S_{ik} are defined by:

$$\begin{aligned} D_{ik} &= \iint_{s_k} \frac{\partial G(\vec{\xi}, \vec{x}_i)}{\partial n_{\xi}} d\vec{\xi} \\ S_{ik} &= \iint_{s_k} G\left(\vec{\xi}, \vec{x}_i\right) d\vec{\xi} \end{aligned} \tag{2.21}$$

where s_k is the surface of panel k and $G(\vec{x}, \vec{\xi})$ is the Green function, referred to as the wave source potential. It is the velocity potential at point $\vec{x} = (x, y, z)$ due to a point source of strength -4π located at point $\vec{\xi} = (\xi_1, \xi_2, \xi_3)$. It meets the free-surface and radiation conditions, and it is expressed by:

$$G(\vec{x}, \vec{\xi}) = \frac{1}{r} + \frac{1}{r''} + 2\int_0^{\infty} \frac{(k+K)\cosh k(z+d)\cosh k(\xi_3+d)}{k\sinh kd - K\cosh kd} e^{-kd} J_0(kR) dk \tag{2.22}$$

with $r = \|\vec{x} - \vec{\xi}\|_2$, $(r'')^2 = (x-\xi_1)^2 + (y-\xi_2)^2 + (z+\xi_3+2d)^2$, $K = \omega^2/g$ the infinite water depth value of k, and J_0 the Bessel function of zeroth order.

Ultimately, equations 2.19 and 2.20 are solved for φ.

2.5 Optimization

From purely geometry to finance through engineering and even sport or daily life, optimization has been in human's mind for centuries. First tackled by Euclid in his "Elements", its formalization was performed later, from the 17^{th} century with the emergence of modern differential calculus thanks to Newton and Leibniz.

In this section, some important optimization techniques will be addressed.

2.5.1 Formalism

The formalism will be such that an optimization problem for the objective function f of the variable $x \in \mathbb{R}^n$, submitted to the equality constraints $\widehat{c}(x) = 0_{\widehat{m}}$ and the inequality constraints $c(x) \geqslant 0_m$ will be formulated as:

$$\begin{array}{lll} \text{minimize} & f & \\ \text{with respect to} & x \in \mathbb{R}^n & \\ \text{subject to} & \widehat{c}_j(x) = 0, & j \in [\![1, \widehat{m}]\!] \\ & c_k(x) \geqslant 0, & k \in [\![1, m]\!] \end{array} \tag{2.23}$$

The objective function is a measure of the performance of a system with regards to some parameters that are chosen by the designer. In most engineering fields, the several objectives are at stake – good performance and low costs most commonly. The objective function will then be a trade-off between these sub-objectives.

2.5.2 Optimization methods

Two major types of methods should be distinguished: gradient-free versus gradient-based ones.

The former are easier to use and have for that reason been the most employed in offshore engineering. They have the ability to explore widely the design space, defined by the set of design variables at use and are therefore likely to find the global minimum of f in this region. Among these methods, one could mention particle swarm, genetic algorithms or Nelder-Mead method.

The latter, as their self-explanatory name suggests, rely on the computation of the gradient of f to converge towards a minimum. They consequently require differentiable objective and constraint functions and they need to be provided their respective derivatives with regards to the design variables. In spite of these additional efforts which could dissuade one to use them, they perform way better than their gradient-free counterparts as the number of design variables increases. One drawback is that they are likely to converge towards a local minimum rather than the global one for functions displaying a significantly erratic behaviour.

This study aims at imlementing one of the state-of-the-art gradient-based method, namely Sequential Quadratic Programming (SQP) algorithm.

2.5.3 Sequential Quadratic Programming (SQP)

SQP has been developed in the second half of 20^{th} century first by Robert Wilson, followed by Shih–Ping Han and Michael Powell in 1976. It essentially consists in applying Newton method to solve the Karush, Kuhn and Tucker (KKT) conditions. Some elements will be addressed before actually tackling this method.

KKT conditions The Lagrangian of an optimization problem is defined as

$$\mathcal{L} : (x, \widehat{\lambda}, \lambda, s) \mapsto f(x) - \widehat{\lambda}^{\top} \cdot \widehat{c}(x) - \lambda^{\top} \cdot \big(c(x) - s^2\big) \tag{2.24}$$

where the vectors $\widehat{\lambda}$ and λ are the so-called Lagrangian multipliers for the equality and inequality constraints, and s is the vector of slack variables. It is such that its stationary points are good candidates for being minima of the problem, and it turns the original constrained problem into an unconstrained problem with new variables.

Necessary conditions on for the minimum of f under the equality and inequality constraints form the so-called first order KKT conditions; they require $\mathcal{L}$ to be stationary at that point according to:

$$\nabla_x \mathcal{L} = 0 \Rightarrow \frac{\partial \mathcal{L}}{\partial x_i} = \frac{\partial f}{\partial x_i} - \sum_{j=1}^{\widehat{m}} \widehat{\lambda}_j \frac{\partial \widehat{c}_j}{\partial x_i} - \sum_{k=1}^{m} \lambda_k \frac{\partial c_k}{\partial x_i} = 0, \quad i \in [\![1, n]\!] \tag{2.25}$$

$$\nabla_{\widehat{\lambda}} \mathcal{L} = 0 \Rightarrow \frac{\partial \mathcal{L}}{\partial \widehat{\lambda}_j} = \widehat{c}_j = 0, \quad j \in [\![1, \widehat{m}]\!] \tag{2.26}$$

$$\nabla_{\lambda} \mathcal{L} = 0 \Rightarrow \frac{\partial \mathcal{L}}{\partial \lambda_k} = c_k - s_k^2, \quad k \in [\![1, m]\!] \tag{2.27}$$

$$\nabla_s \mathcal{L} = 0 \Rightarrow \frac{\partial \mathcal{L}}{\partial s_k} = \lambda_k s_k = 0, \quad k \in [\![1, m]\!] \tag{2.28}$$

$$\lambda_k \geqslant 0, \quad k \in [\![1, m]\!] \tag{2.29}$$

Newton's method Newton's method relies on a quadratic approximation of the objective function at the current point x_k from iteration k, resulting from a Taylor series expansion of it with a step d_k:

$$f(x_k + d_k) = f(x_k) + {}^t\nabla f(x_k) \cdot d_k + \frac{1}{2} {}^t d_k \cdot \nabla^2 \cdot f(x_k) d_k + o(\|d_k\|^2) \tag{2.30}$$

Choosing d_k such that $x_{k+1} = x_k + d_k$ is located at the minimum of this quadratic function (i.e. the derivative w.r.t d_k of 2.30 is null), an expression of it is found by solving

$$\nabla^2 f\left(x_k\right) d_k = -\nabla f\left(x_k\right). \tag{2.31}$$

Newton's method is efficient for some functions but can perform very badly in some situations; quasi-Newton's methods were developed to overcome these issues and improve the costly computation of the Hessian.

SQP For a problem with equality constraints only, equation 2.31 applied to the Lagrangian rewrites

$$\nabla^2 \mathcal{L}\left(x_k, \lambda_k\right) d_k = -\nabla \mathcal{L}\left(x_k, \lambda_k\right). \tag{2.32}$$

The detailed equation is found as:

$$\begin{bmatrix} \nabla^2 f(x_k) & -{}^t\nabla c(x_k) \\ \nabla c(x_k) & 0 \end{bmatrix} \cdot \begin{bmatrix} p_{x_k} \\ p_{\lambda_k} \end{bmatrix} = \begin{bmatrix} \nabla f(x_k) - {}^t\nabla c(x_k) \cdot \lambda \\ c(x_k) \end{bmatrix} \tag{2.33}$$

Inequality constraints can be handled considering only active constraints at each iteration, and treating them as equality constraints.

2.5.4 Computation of the derivatives

As illustrated by the previous theoretical developments, the role of the derivatives is crucial in gradient-based methods. It is therefore necessary to compute them accurately.

Different techniques to provide numerical derivatives exist, among which can be cited - ranked by increasing order of precision - first order finite differences (FD), complex step (CS), algorithmic differentiation and analytic methods (the two latter being of the same order). While the first two ones are based on Taylor expansions and are relatively easy to implement, they only approximate the value of the derivatives and can be computationally demanding: they should mostly be used when the function to differentiate acts as a black box for which only the inputs and are outputs are accessible. Algorithmic differentiation is accurate but very tedious to implement; however, it can be a great improvements to FD or CS when the source code of a software is provided. Ultimately, analytic methods are the preferred techniques to deliver analytic derivatives. They are commonly split into two variants: direct method and adjoint method.

In OpenMDAO, each component is defined by its inputs and outputs. In order for the optimization process to be performed correctly, all the derivatives of the outputs with regards to the input variables on which they depend must be specified ("variable" here should be understood litterally as "which varies"; some inputs can also be constants, and in that case, the code does not expect the user to provide it with the corresponding derivatives).

The following is detailed in Ang (2019). For a given function $f : \mathbf{X} \longmapsto \mathbf{Y} = f(\mathbf{X})$ which transforms a $m \times n$ matrix $\mathbf{X}$ into a $p \times q$ matrix $\mathbf{Y} = f(\mathbf{X})$, the derivative of f with regards to $\mathbf{X}$ is defined as

$$\nabla_{\mathbf{X}} f = \frac{\partial f}{\partial \mathbf{X}} = \frac{\partial \operatorname{vec}(f)}{\partial \operatorname{vec}(\mathbf{X})} \tag{2.34}$$

where the vec operator expands any matrix $\mathbf{X}$ columnwise:

$$\operatorname{vec}(\mathbf{X}) = [X_{11}, X_{21}, \dots X_{m1}, X_{12}, X_{22}, \dots X_{m2}, \dots, X_{1n}, X_{2n}, \dots X_{mn}]^\top .$$

The differential-derivative equation is then

$$\operatorname{vec}(df) = (\nabla_{\mathbf{X}} f)^\top \operatorname{vec}(d\mathbf{X}) = \left(\frac{\partial f}{\partial \mathbf{X}}\right)^\top \operatorname{vec}(d\mathbf{X}). \tag{2.35}$$

One has to recall that the derivative of a function $g : \mathbf{u} \longmapsto \mathbf{v} = g(\mathbf{u})$ which transforms a $m \times 1$ vector $\mathbf{u}$ into a $n \times 1$ vector $\mathbf{v}$ is defined as

$$\nabla_{\mathbf{u}} g = \begin{bmatrix} \frac{\partial g_1}{\partial u_1} & \frac{\partial g_2}{\partial u_1} & \cdots & \frac{\partial g_n}{\partial u_1} \\ \frac{\partial g_1}{\partial u_2} & \frac{\partial g_2}{\partial u_2} & \cdots & \frac{\partial g_n}{\partial u_2} \\ \vdots & \vdots & \ddots & \vdots \\ \frac{\partial g_1}{\partial u_m} & \frac{\partial g_2}{\partial u_m} & \cdots & \frac{\partial g_n}{\partial u_m} \end{bmatrix} \tag{2.36}$$

In OpenMDAO, the term $(\nabla_{\mathbf{X}} f)^\top$ is provided to the code. However, matrix derivatives are defined rowwsise instead, according to

$$\nabla_{\mathbf{X}} f = \begin{bmatrix} \frac{\partial f_{11}}{\partial X_{11}} & \frac{\partial f_{12}}{\partial X_{11}} & \cdots & \frac{\partial f_{1q}}{\partial X_{11}} & \frac{\partial f_{21}}{\partial X_{11}} & \cdots & \frac{\partial f_{pq}}{\partial X_{11}} \\ \frac{\partial f_{11}}{\partial X_{12}} & \frac{\partial f_{12}}{\partial X_{12}} & \cdots & \frac{\partial f_{1q}}{\partial X_{12}} & \frac{\partial f_{21}}{\partial X_{12}} & \cdots & \frac{\partial f_{pq}}{\partial X_{12}} \\ \vdots & \vdots & \ddots & \vdots & \vdots & & \vdots \\ \frac{\partial f_{11}}{\partial X_{1n}} & \frac{\partial f_{12}}{\partial X_{1n}} & \cdots & & & \cdots & \frac{\partial f_{pq}}{\partial X_{1n}} \\ \frac{\partial f_{11}}{\partial X_{21}} & \frac{\partial f_{12}}{\partial X_{21}} & \cdots & & & \cdots & \frac{\partial f_{pq}}{\partial X_{21}} \\ \vdots & \vdots & & \vdots & \vdots & \ddots & \vdots \\ \frac{\partial f_{11}}{\partial X_{mn}} & \frac{\partial f_{12}}{\partial X_{mn}} & \cdots & \frac{\partial f_{1q}}{\partial X_{mn}} & \frac{\partial f_{21}}{\partial X_{mn}} & \cdots & \frac{\partial f_{pq}}{\partial X_{mn}} \end{bmatrix} = \frac{\partial \operatorname{vech}(f)}{\partial \operatorname{vech}(\mathbf{X})}, \tag{2.37}$$

where vech defines the horizontal vectorization

$$\mathrm{vech}(\mathbf{X}) = [X_{11}, X_{12}, \dots X_{1n}, X_{21}, X_{22}, \dots X_{2n}, \dots, X_{m1}, X_{m2}, \dots X_{mn}]^{\top} .$$

The link between the two vectorizing operators is expressed as

$$\mathrm{vech}(\mathbf{X}) = \mathrm{vec}(\mathbf{X}^{\top}) = C \cdot \mathrm{vec}(\mathbf{X}), \tag{2.38}$$

with C the commutation matrix for $\mathbf{X}$.

2.5.5 Sparsity

In most cases, the jacobian matrix is mostly sparse; for large jacobians, it is necessary to reduce the computation time by taking this sparsity into account. SNOPT optimizer has been developed with this aim in mind (Gill et al. (2002)); it is based on SQP method.

3 Optimization of a spar

In this section, a model of a spar platform will be built and a trial optimization problem with OpenMDAO will be set up and run. It was originally made by de Renty (2020). The purpose of it is to get used to the methodology and to take in hand OpenMDAO, its logic and formalism, plus to run an optimization problem including hydrodynamic computations and see if the main physical trends are being captured. However, this problem being really simplified, its results should not be taken a references: the main purpose is to illustrate the process which will be explored further for another floater.

3.1 Problem description

A classical circular cylinder shaped spar with catenary mooring lines is under study here. The geometric parameters are defined in figure 10. The focus is made on the floater, independent from any effects due to the turbine mounted on it, which will be represented as a dead weight corresponding to the DTU 10 MW turbine.

The thickness t_w of the steel plates constituting the walls is taken as constant equal to 10 cm over the depth of the spar. The water depth is chosen as 320 m.

Waves in the plane (x, z) are the only source of excitation and only surge and pitch motions are under study. Therefore, the problem is reduced to a 2D problem.

The hydrodynamic loads are computed by HydroD using first order diffraction-radiation theory. Aerodynamics is reduced to a constant force equal to the rated thrust being applied at the hub height and the control system is not implemented. The floater is considered as a rigid body. The restoring coming from the mooring lines is linearized around the mean position of the spar. It is provided by de Renty (2020) as a 2×2 stiffness matrix most probably computed from the optimized spar from Hegseth et al. (2020b) under rated conditions.

Then, due to the linearity of the problem, the analysis is performed in the frequency domain.

The hydrodynamic environment is defined by a JONSWAP spectrum with parameters $(H_s, T_p, \gamma) = (6.2\,\mathrm{m}, 12.5\,\mathrm{s}, 3.3)$.

3.1.1 Detailed presentation

The geometry is built and meshed by GeniE. Then, the added mass and damping matrices A, B plus the excitation force per unit amplitude $F_{exc} = \Re(\bar{F}_{exc}e^{i\omega t})$ are obtained by HydroD based on the mesh file from GeniE. A guess for the viscous damping matrix B_{visc} is made, so that the equation of motion

$$(M + A)\ddot{\eta} + (B + B_{visc})\dot{\eta} + (K + K_{moor})\eta = F_{exc} \tag{3.1}$$

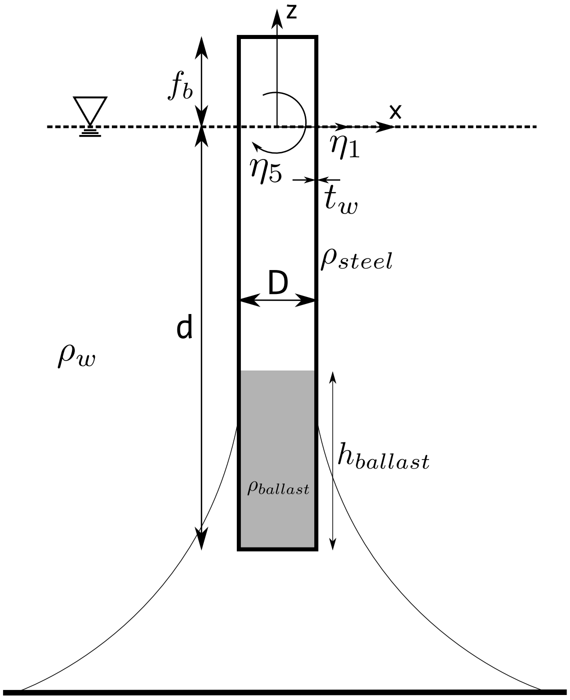

Figure 10: Description of the spar
(The location of the fairleads is purely illustrative.)

can be solved for $\eta = [\eta_1, \eta_5]^\top = \Re(\bar{\eta} e^{i\omega t})$ in frequency domain, where ω is the frequency of the incident wave, and t the current time.

Then, the mechanical transfer function $H(\omega) = [H_{\eta_1}(\omega), H_{\eta_5}(\omega)]^\top$, which gives the motions from the amplitude of the incident wave, is obtained as

$$H(\omega) = \left[(K + K_{moor}) - \omega^2(M + A) + i\omega(B + B_{visc})\right]^{-1} \cdot \bar{F}_{exc}(\omega). \tag{3.2}$$

Consequently, the transfer function for the combined motion of a strip dz located at a distance z from the origin, $s = \eta_1 + z\eta_5$ is $H_s = H_{\eta_1} + zH_{\eta_5}$ and the transfer function for the combined velocity is obtained as $H_{\dot{s}} = i\omega H_s$.

The next step is to find response spectrum for the combined velocity $S_{\dot{s}}(\omega) = |H_{\dot{s}}(\omega)|^2 S_w(\omega)$ where the wave spectrum S_w is chosen to be a JONSWAP spectrum with parameters (H_s, T_p). Eventually, the standard deviation for $\dot{s}$ is accessed by mean of $\sigma_{\dot{s}} = \sqrt{\int_0^{+\infty} S_{\dot{s}}(\omega) dw}$.

This now provides one with the new viscous damping coefficient which stems from the linearization of the drag force on the strip dz due to the motion of the spar only, $dF_D = -\frac{1}{2}\rho_w C_D D\dot{s}|\dot{s}|$ according to:

$$dF_D \simeq -\frac{1}{2}\rho_w C_D D\sqrt{\frac{\pi}{8}}\sigma_{\dot{s}}\dot{s} = -B_{visc}\dot{s}. \tag{3.3}$$

This new expression for B_{visc} will be compared to the previous one and iterations will be performed until sufficient convergence.

3.1.2 Objective function

In this report, the objective function to minimize will always be the LCoE. For the sake of simplicity, the mass of steel will be deemed to be the driving parameter of the LCoE and will therefore be the objective to minimize.

One can express it by:

$$m_{steel} = \left[\pi(D-t)t(d+f_b) + \frac{1}{2}\pi D^2 t\right]\rho_{steel} \tag{3.4}$$

3.1.3 Design variables

Since the purpose of this first optimization is not to reach an accurate and exhaustive model of a spar, but instead to perform a simple optimization, only two design variables have been selected: the diameter D and the draft d of the floater.

3.1.4 Constraints

Six constraints are being applied:

- The mass of the ballast must be obviously positive $m_{ballast} > 0$.
- It must be located under the free surface $d - h_{ballast} \geq 0$; it is again a straightforward condition.
- The mean pitch angle η_5 of the spar under loading conditions should be lower than 5°. Indeed, for high pitch angles, the turbine's efficiency decreases.
- The hydrostatic stiffness in pitch K_{55} has to be greater than 0 in order to actually get restoring and to ensure the system to be stable.
- The standard deviations for surge and pitch motions, σ_{η_1} and σ_{η_5} should be respectively under $5\,\mathrm{m}$ and $0.075°$. These criteria deal with the quality of the production of electricity as well as with the loads on the turbine and tower.

Then, to stick to the formalism defined in section 2.5, the problem writes

$$\begin{aligned}
&\text{minimize} && m_{steel} \\
&\text{with respect to} && x = (D, d) \\
&\text{subject to} && m_{ballast} \geqslant 0 \\
& && K_{55} \geqslant 0 \\
& && \eta_5 \leqslant 0 \text{ under } T_{rated} = 1.5\,\mathrm{MN} \\
& && \sigma_{\eta_1} \leqslant 5\,\mathrm{m} \\
& && \sigma_{\eta_5} \leqslant 0.075°.
\end{aligned} \tag{3.5}$$

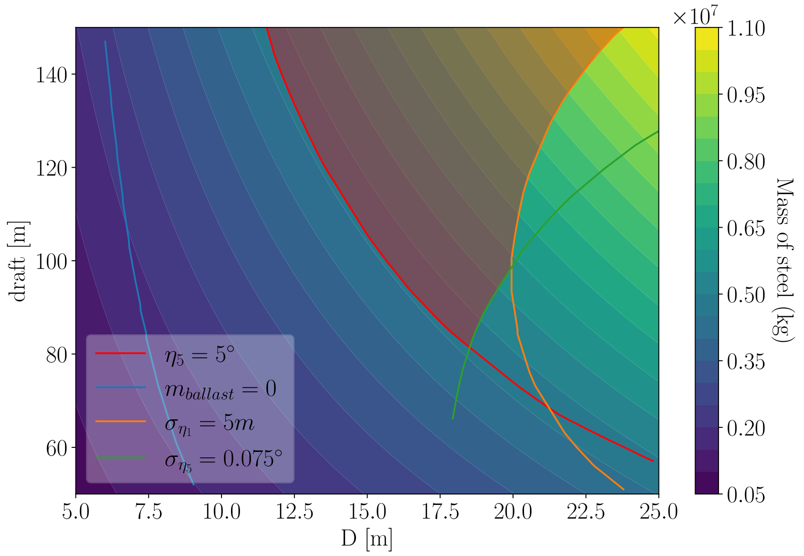

Figure 11: Design space for the optimization of the spar buoy

The feasible space, defined as the intersection of the constraint sets and the objective set, is represented in figure 11. One should notice that the mass of steel varies little along the static pitch constraint.

3.1.5 Computation of the derivatives

In this first example, finite differences across the whole model will be used for the sake of simplicity.

3.2 Results

Since this model is meant to be a training to take hand the procedure, only a few runs will be performed and trends will be analysed and compared to those obtained by de Renty who used McCamy&Fuchs equation to compute the hydrodynamic loads.

The model was run for two different cases, for which the results of the optimization are presented in table 1. Figure 12 provides a graphical representation for the optimization process in Run 1.

The statistics of the two runs are fairly similar, even though the two starting points are different. The optimal values of the objective function (the mass of steel) only differ by 0.7 % taking Run 1 as the reference, but a more significant shift is observed for the values of the optimal draft. This is explained by the fact that the most active constraint is the one on the static pitch, along which boundary the mass of steel varies very little in comparison to the variation in draft. To improve the agreement between the two runs, one could decrease the tolerance of the SLSQP solver, set to $\varepsilon = 1 \times 10^{-2}$.

Run	1	2
Starting point (m)	$(17, 130)$	$(25, 140)$
iterations	7	8
function evaluations	13	10
gradient evaluations	7	8
x^* (m)	$(12, 72, 132.50)$	$(12, 26, 137.40)$
$f(x^*)$ (t)	4668.93	4636.52
Static pitch angle (°)	4.76	5.00
$\sigma_{\eta 1}$ (m)	4.93	4.94
$\sigma_{\eta 5}$ (°)	0.074	0.071

Table 1: Statistics of the optimization of the spar

In his Master's thesis, de Renty found a different optimal point $x^* = (15.41\,\text{m}, 102.10\,\text{m})$ using McCamy&Fuchs equation, valid for fixed vertical circular cylinders, for the excitation loads and the analytic value of the added mass for an infinite cylinder (see equation 3.6). The calculations are then performed much faster than in the current case, but should not be as accurate.

$$\mathbf{A} = \rho_w \pi \frac{D^2}{4} \begin{bmatrix} d & d^2/2 \\ d^2/2 & d^3/3 \end{bmatrix}. \tag{3.6}$$

It could also be mentioned that even though Run 2 started outside of the feasible space, the optimization was performed correctly.

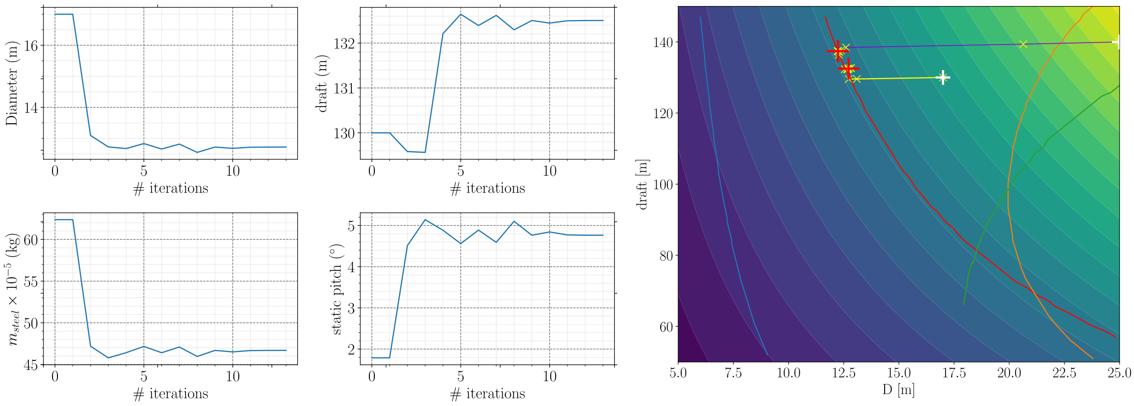

(a) Evolution of the diameter, draft, mass of steel and static pitch angle during Run 1

(b) Iteration paths for Runs 1 (yellow) and 2 (purple)

Figure 12: Graphical representation of the runs

4 Modelling of the floater OO-Star

The floater OO-Star is developed by the Norwegian company Dr.Techn.Olav Olsen AS. It is one of the two floaters finally selected by the program LIFES50+ and it was designed to support the DTU 10 MW turbine. The geometry on which the present study is based is slightly modified compared to the original one to make it more easy to modify it: the skirt under the pontoons has been removed and the pontoons are no longer tapered, which means they keep a constant width equal to the bottom diameter of the outer columns. A scheme of the updated geometry is proposed in figure 13a and its complete parametrization is given in report D4.2 Yu et al. (2018).

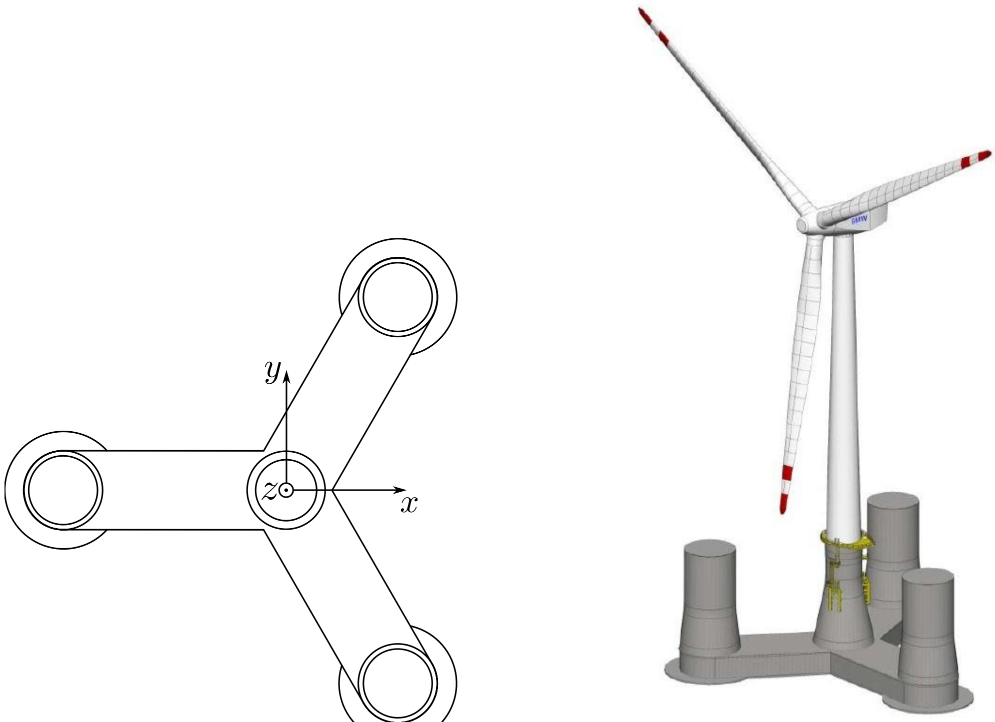

(a) Top view of the floater OO-Star

(b) 3D view of OO-Star, mounted by a turbine (Credits: Dr.techn.Olav Olsen AS)

Figure 13: Description of the geometry of OO-Star

4.1 Model components

Figure 14 gives the parametrization and physical components used to model the structure. The reference frame is such that the origin O lies at the intersection of the mean water level and the main axis of the tower, with the z axis pointing upwards.

The hull is a rigid body submitted to wave excitation, with added mass $A(\omega)$, and which motion is restrained in translation and rotation due to hydrodynamic restoring, frequency dependent mooring stiffness and radiation damping, and viscous

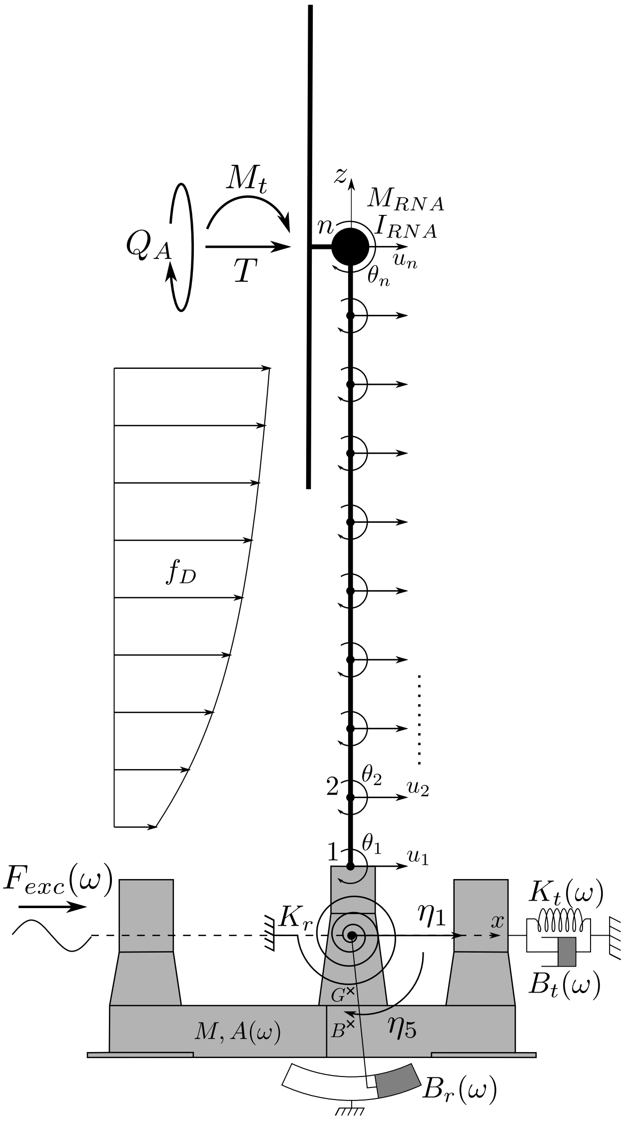

Figure 14: Modelling of the problem

damping (referred as $K_t(\omega)$, K_r, $B_t(\omega)$ and $B_r(\omega)$). Surge and pitch motions η_1, η_5 are the two degrees of freedom (dofs) of the hull, with regards to O.

The tower of the turbine is a flexible body, broken down into a set of n beam elements, with one translation dof u_i and one rotation dof θ_i at each node. No structural damping is considered here.

The nacelle and the rotor are reduced to a point mass M_{RNA} with inertia I_{RNA}, on which a thrust force $T(\omega)$ obtained from a spectrum is applied. Aerodynamic damping is also added, with a linear damper B_{aero}.

In the following sections, each aspect of the model will be tackled in details.

4.2 Hydrodynamics

The dimensions of the platform being large compared to the incoming wave lengths, the effects of diffraction and radiation will be significant. Furhtermore, a stochastic linearization of drag forces is performed.

4.2.1 Potential loads

One key aspect of this model is the implementation of diffraction-raditation loads on the structure, in order to get a more accurate estimation of the hydrodynamic loads, compared to the classical use of Morison formula. These are found thanks to HydroD (which in turn uses WAMIT), which requires primarily to define properly the meshing of the floater.

The hydrodynamic coefficients are compared to those found in deliverable D4.5 A.Pegalajar-Jurado et al. (2018). The added mass and damping matrices of the structure are plotted in figure 15; they follow the same path as the reference ones.

The counterpart to this choice is that successive calls to WAMIT are time-consuming. Therefore, a surrogate model of the hydrodynamic coefficients is used. To do so, the

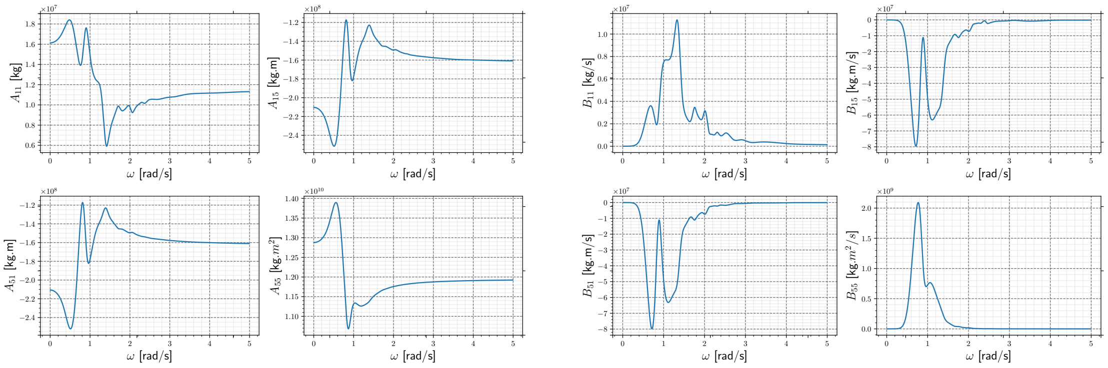

(a) Added mass coefficients (b) Damping coefficients

Figure 15: Hydrodynamic coefficients for OO-Star

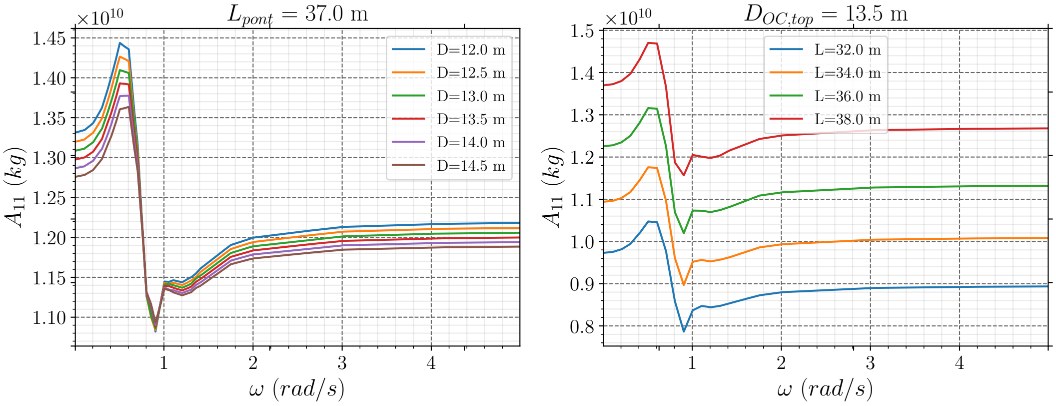

Figure 16: Interpolation of A_{55} over the design space

design space was sampled, and at each sampled point, a call to WAMIT has been realised. The result is a hydrodynamic database on which a linear interpolation is performed for any new point in the design space. Figure 16 gives an overview of the result of the procedure for the pitch-pitch added mass coefficient.

4.2.2 Viscous effects

Here, the structure is deemed to be brand new, which is to say that no marine growth is taken into account. The procedure for implementing viscous loads on the floater is strictly identical to the one from (de Renty de Renty, 2020). That is to say that the quadratic drag force on a cylinder strip moving with the combined velocity $\dot{s}$ submitted to the similarly oriented inflow velocity u, expressed as

$$dF_D = \frac{1}{2}\rho C_D D(u - \dot{r})|u - \dot{s}| \tag{4.1}$$

according to the classical Morison equation, now becomes

$$dF_{D,l} = -\frac{1}{2}\rho C_D D\sqrt{\frac{8}{\pi}}\sigma_{\dot{s}}\dot{s} \tag{4.2}$$

by mean of stochastic linearization. In the latter expression, the excitation term has been deleted since it is assumed negligible in front of the potential excitation loads. Furthermore, the velocity of the strips is computed as a combination of the surge and pitch rigid body motions weighted by the geometrical parameters.

Figure 17 displays the elements of the structure which are given drag properties in this analysis. There are five distinct groups: the pontoons (blue), the heave plates (red), the conical part of the central column (green), the conical part of the outer columns (purple) and their circular edge (yellow). With this definition, the triangular surface in the center of the floater is not given any viscous properties; however, the heave plates and the ends of the pontoons slightly overlap in such a way that the overlapping surface is almost equal to the triangular one (see greyed

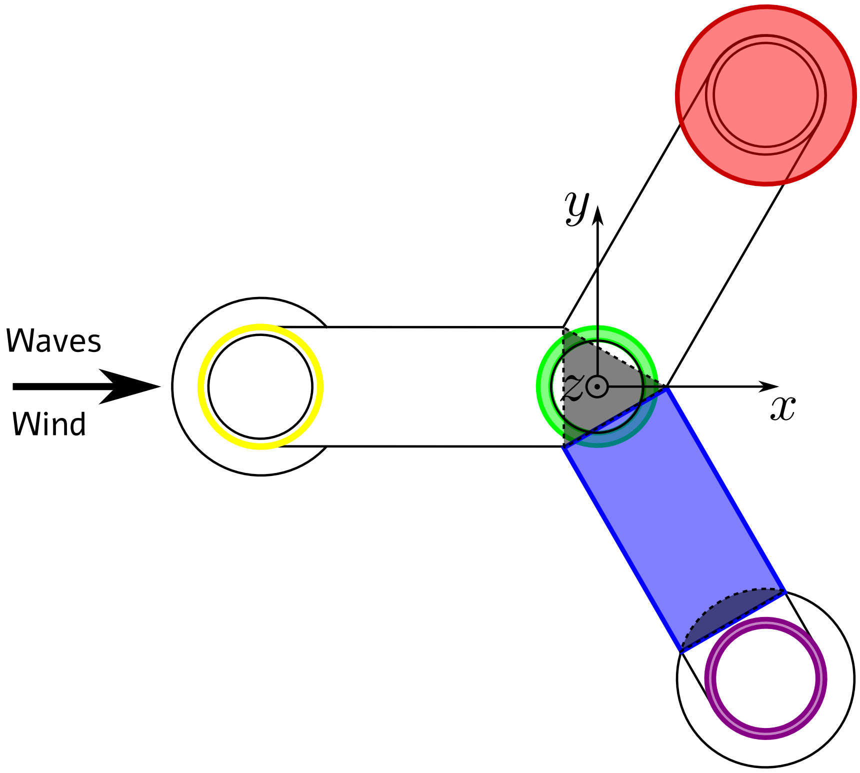

Figure 17: The different drag elements considered

Member	**Notation**	**Drag coefficient**
Pontoons	$C_{D,pont}$	2.05
Heave plates	$C_{D,hp}$	10.
Center column, conical part*	$C_{D,CC}$	0.716
Outer column, top part	$C_{D,OC,top}$	0.720
Outer column, conical part*	$C_{D,OC,con}$	0.713
Outer column, circular edge	$C_{D,OC,edge}$	0.706

Table 2: Drag coefficients for each member [2]

zones), which should then not affect heave motion. It is nonetheless not the case for pitch, which will be a little overdamped.

The different drag coefficient are provided in A.Pegalajar-Jurado et al. (2018) and re-written in table 2.

Even though equation 4.2 is made linear, it is a priori not easy to implement since the strip velocities are obtained solving the equations of motion, which in turn requires the knowledge of the damping coefficient, function of the standard deviations of the strip velocities. This behaviour is typically solved by implementing an iterative scheme, as displayed in figure 18. In OpenMDAO, a nonlinear block Gauss-Seidel solver is performing the iterative procedure.

---

[2] *refers to the elements for which the drag coefficient is averaged over the length of the conical element.

The details of the equations are provided in de Renty (2020), section 2.2.2.

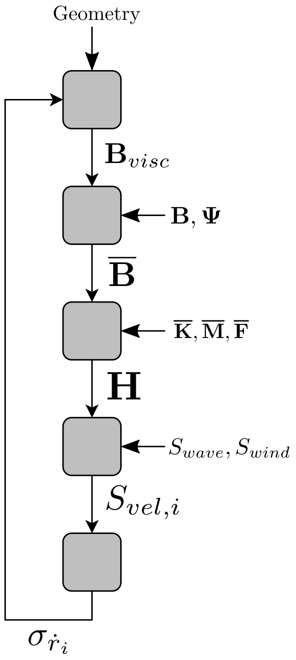

Figure 18: Iterative scheme for the viscous damping

4.3 Aerodynamics

4.3.1 First implementation

Initially, the aerodynamics was made very simple: a point thrust force was applied at hub height, which amplitude was provided through a thrust force spectrum obtained from simulations for different turbulent wind conditions in SIMA. No rotor was added at that point, and therefore no controller either. Aerodynamic damping was modelled by mean of a linear damper. Figure 19 illustrates this simplified model. Some first optimization results based on this model will be at the end of the report.

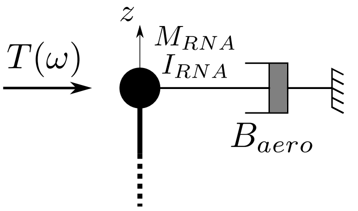

Figure 19: Simplified aerodynamic model (viewed at hub height)

4.3.2 More advanced model

The aerodynamic model relies on the BEM procedure combined with Glauert correction to account for compressibility effects for large values of the normal induction factor a_n (i.e. $a_n \geq 0.2 - 0.4$), Prandtl's tip loss factor, which stands for 3D effects at the blade tips, and hub loss correction factor. Tower shadow and wind shear are not included. The implementation is detailed in Ning et al. (2015).

The resultant loads of interest are the flapwise shear force F_y, the flapwise bending moment M_z and the edgewise bending moment M_y. They are found by integrating the normal and tangential loads from 2.7 over one blade:

$$F_y = \int_0^R F_n dr, \;\; M_z = \int_0^R rF_n dr, \;\; M_y = \int_0^R rF_t dr. \tag{4.3}$$

Then, the aerodynamic torque, thrust force and tilting moment for the rotor (made of three blades) are found by:

$$Q_A = 3M_y, \;\; T = 3F_y, \;\; M_t = \frac{3}{2}M_z, \tag{4.4}$$

where the factor 1/2 in the computation of M_t is explained in chapter 5.6 of Halfpenny (1998).

In addition to BEM, a rotor effective wind speed is used to describe the incoming wind field, which varies over the rotor area, by a single scalar parameter. This effective wind speed is dependent on the mean wind speed as well as on the type of resultant load (either thrust T, tilting moment M_t or aerodynamic torque Q_A).

The procedure to compute these wind speeds is described in Hegseth (2020) and rewritten here for clarity. It relies on a formula from Halfpenny (1998) which desribes the single-sided (i.e. given for positive frequencies) cross spectral density of the wind speed – which is sampled following the instantaneous position of the blade (known as rotational sampling) – seen by two blade elements j and k:

$$S_v^{(j,k)}(\omega) = \sum_{n=-\infty}^{+\infty} e^{in\psi} K_n^{(j,k)} \left(|\omega - n\dot{\varphi}|\right) S_U \left(|\omega - n\dot{\varphi}|\right). \tag{4.5}$$

This spectrum gives the distribution of energy for the local incoming wind speed seen by one blade element and affected by another one.

In the previous expression, S_U denotes the incoming wind speed spectrum, ψ the azimuth angle between the elements (i.e. $\psi = 2\pi/3$ for a three bladed rotor), and K_n is the n^{th} real coefficient of the Fourier transform of the coherence function γ:

$$K_n^{(j,k)}(\omega) = \frac{1}{\pi} \int_0^{\pi} \gamma(\omega, d_{j,k}) \cos(n\theta) d\theta \tag{4.6}$$

where γ gives the degree of correlation between the wind speed seen by two points in space separated by a distance d, for a given frequency of interest f. The coherence function is chosen according to IEC standards (IEC), and is displayed below:

$$\gamma(f, d) = \exp\left(-12\left[\left(\frac{fd}{U}\right)^2 + \left(\frac{0.12d}{L_c}\right)^2\right]^{1/2}\right), \tag{4.7}$$

with U the mean wind speed at hub height and L_c a coherence length parameter.

The incoming wind spectrum is also chosen based on IEC standards; it is a Kaimal spectrum for a class B wind turbine (i.e. with a turbulence intensity $I = \sigma_U/U = 0.14$):

$$S_U(\omega) = \frac{1}{2\pi} \frac{4\sigma_U^2 L/U}{\left(1 + 6\left(\frac{\omega}{2\pi}\right) L/U\right)^{5/3}}, \tag{4.8}$$

with $L = 8.1\Lambda$ the velocity component integral scale parameter and $\Lambda = 42\,\mathrm{m}$ for the current turbine, the longitudinal turbulence scale parameter.

Based on the local incoming wind speed spectrum provided by 4.5 and on the results from BEM, one can access the spectra of the loads on the rotor. When computing the sum 4.5, only harmonics multiples of three times the rotor speed remain: only the ones up to 6P were kept. Then, the transfer functions from incoming wind speed to rotor effective wind speed are found by:

$$v_T(\omega) = \sqrt{\frac{S_T(\omega)}{(3F_{y,v})^2 S_{wind}(\omega)}} \tag{4.9}$$

$$v_{M_t}(\omega) = \sqrt{\frac{S_{M_t}(\omega)}{(\frac{3}{2}M_{z,v})^2 S_{wind}(\omega)}} \tag{4.10}$$

$$v_{Q_A}(\omega) = \sqrt{\frac{S_{Q_A}(\omega)}{(3M_{y,v})^2 S_{wind}(\omega)}}. \tag{4.11}$$

In this latter expression, one should notice that the quantities $X_{,v}$ can be accessed by $X_{,v} = -X_{,\lambda}\frac{R\dot{\varphi}}{U^2}$.

Furthermore, the drag effects due to the wind flow on the tower are taken into account by one mean quadratic term due to the mean wind speed, and one stochastically linearized dynamic term corresponding to the turbulent variations of the wind speed. A wind shear with $\alpha = 0.14$ and a normal turbulent model (NTM) for a class B turbine are assumed – i.e. a turbulence intensity $I = 0.14$ – according to (IEC). The expressions of these two forces are given below:

$$f_{D,0}(z) = \frac{1}{2}\rho_{air} D(z) C_D u^2(z) \tag{4.12}$$

$$f_D(z) = \frac{1}{2}\rho_{air} D(z) C_D \sqrt{\frac{8}{\pi}}\sigma_u(z) u(z) \tag{4.13}$$

where $u(z) = U\left(\frac{z}{z_{G,RNA}}\right)^{\alpha}$ and $\sigma(z) = (0.75u(z) + 5.6)I$.

4.4 Dynamics

4.4.1 Linearization procedure

The procedure to formalize the equations of motion is closely following the one adopted by Hegseth et al. (2020b). The system is linearized around its operational point and the equations are solved in the frequency domain. A state-state formulation is used, both for the dynamics of the structure and for the control system. The association of these two in a closed loop leads to the complete aero-hydro-servo-elastic model.

A perturbation in the state and input variables around the operational point, respectively $\mathbf{x}$ and $\mathbf{u}$, is considered:

$$\mathbf{x} = \mathbf{x_0} + \Delta\mathbf{x}, \quad \mathbf{u} = \mathbf{u_0} + \Delta\mathbf{u}. \tag{4.14}$$

Along with the state-space formalism, the dynamic equations of motion are expressed as

$$\Delta\dot{\mathbf{x}} = \mathbf{A}\Delta\mathbf{x} + \mathbf{B}\Delta\mathbf{u}, \tag{4.15}$$

where $\mathbf{A}$ and $\mathbf{B}$ denote respectively the state matrix and the input matrix.

4.4.2 Generalized coordinates

The analysis will be performed using generalized coordinates, that is to say a set of predefined relevant modes $\boldsymbol{\Psi}$ to describe the displacement of the structure. At a given point of the vertical axis located at a distance z from the origin, the displacement at time t will be obtained by:

$$w(z,t) = \boldsymbol{\Psi}^\top(z) \cdot \mathbf{q}(t) \tag{4.16}$$

where $\mathbf{q}$ designates the corresponding time dependent wheight factors for each mode.

Here, the first three eigenmodes stemming from the eigenproblem seen before are selected: two rigid body modes ψ_1 and ψ_5 standing for surge and pitch, and one flexible mode ψ_7 for the bending of the tower, which was chosen to also include some pitch (see figure 20c). Consequently, the modal vector is expressed as:

$$\boldsymbol{\Psi} = \begin{bmatrix} \psi_1 \\ \psi_5 \\ \psi_7 \end{bmatrix} \tag{4.17}$$

Figure 20 describes these modes. In addition to them, the rotation of the rotor is also taken into account. In the rest of the study, the rotor speed will be designated by $\dot{\varphi}$.

The mathematical expressions for the two rigid body modes are elementary:

$$\psi_1 : z \mapsto 1 \tag{4.18}$$

$$\psi_5 : z \mapsto \frac{z}{z_{hub}} \tag{4.19}$$

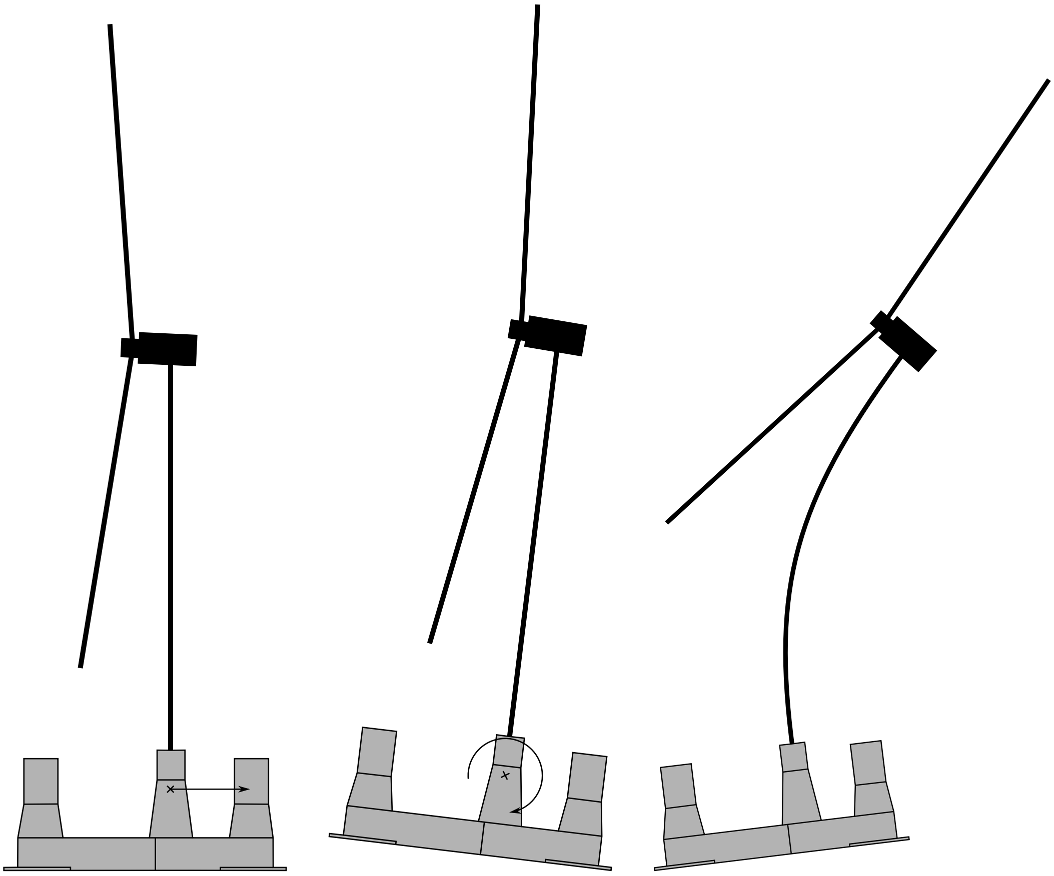

(a) Surge (b) Pitch (c) Bending

Figure 20: The three modes for the structures

The expression for the bending mode is obtained by interpolating the bending mode shape - found by solving the eigenvalue problem - with a fourth order polynomial by mean of a least square formulation. Since the floater is deemed to be rigid and the tower is considered as a cantilever beam linked to the floater, the fitting polynomial and its first derivative need to be constrained at the junction between the floater and the tower. Figure 21 displays the corresponding polynomial.

The uncommon aspect of the study comes from the non-orthogonality of the modes, which will give rise to some coupling effects between them.

The dynamic variables of the system are then expressed according to:

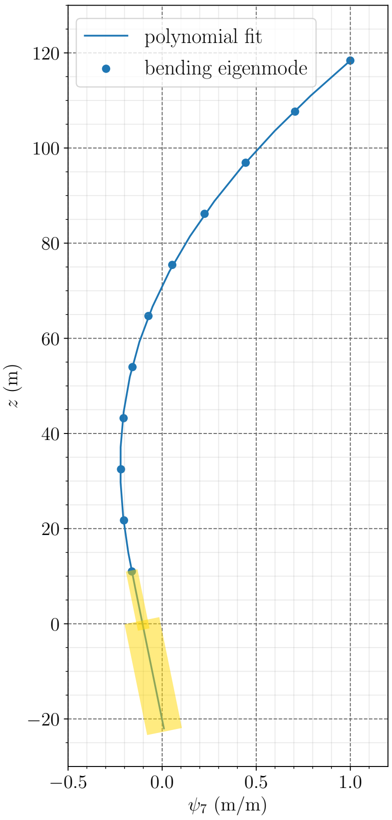

Figure 21: Fitted bending mode

$$\begin{aligned}\overline{\mathbf{M}}(\omega) = \int_{z_{base}}^{z_{G,RNA}} & m(z)\mathbf{\Psi}(z)\mathbf{\Psi}^{\top}(z)dz + m_{\text{plat}}\mathbf{\Psi}\left(z_{G,plat}\right)\mathbf{\Psi}^{\top}\left(z_{G,plat}\right) \\ & + m_{RNA}\mathbf{\Psi}\left(z_{G,RNA}\right)\mathbf{\Psi}^{\top}\left(z_{G,RNA}\right) + I_{55,plat}\mathbf{\Psi}_{,z}(0)\mathbf{\Psi}_{,z}^{\top}(0) \\ & + A_{11}(\omega)\mathbf{\Psi}(0)\mathbf{\Psi}^{\top}(0) + A_{15}(\omega)\mathbf{\Psi}(0)\mathbf{\Psi}_{,z}^{\top}(0) \\ & + A_{51}(\omega)\mathbf{\Psi}_{,z}(0)\mathbf{\Psi}^{\top}(0) + A_{55}(\omega)\mathbf{\Psi}_{,z}(0)\mathbf{\Psi}_{,z}^{\top}(0)\end{aligned} \tag{4.20}$$

$$\begin{aligned}\overline{\mathbf{B}}(\omega) = & (B_{11} + B_{visc,11})\mathbf{\Psi}(0)\mathbf{\Psi}^{\top}(0) + (B_{15} + B_{visc,15})\mathbf{\Psi}(0)\mathbf{\Psi}_{,z}^{\top}(0) \\ & + (B_{51} + B_{visc,51})\mathbf{\Psi}_{,z}(0)\mathbf{\Psi}^{\top}(0) + (B_{55} + B_{visc,55})\mathbf{\Psi}_{,z}(0)\mathbf{\Psi}_{,z}^{\top}(0)\end{aligned} \tag{4.21}$$

$$\begin{aligned}\overline{\mathbf{K}} = \int_{z_{base}}^{z_{G,RNA}} & EI(z)\mathbf{\Psi}_{,zz}(z)\mathbf{\Psi}_{,zz}^{\top}(z)dz + \int_{z_{base}}^{z_{G,RNA}} N(z)\mathbf{\Psi}_{,z}(z)\mathbf{\Psi}_{,z}^{\top}(z)dz \\ & + (K_{hydro,55} + K_{moor,55})\mathbf{\Psi}_{,z}(0)\mathbf{\Psi}_{,z}^{\top}(0) + K_{moor,11}\mathbf{\Psi}(0)\mathbf{\Psi}^{\top}(0) \\ & + K_{moor,15}\mathbf{\Psi}(0)\mathbf{\Psi}_{,z}^{\top}(0) + K_{moor,51}\mathbf{\Psi}_{,z}(0)\mathbf{\Psi}^{\top}(0),\end{aligned} \tag{4.22}$$

where derivatives are denoted by mean of a subscript:

$$\frac{\partial f}{\partial x \partial y} = f_{,xy}. \tag{4.23}$$

In equations 4.20 to 4.22, m is the mass per unit length of the tower, m_{plat} and

m_{RNA} are the masses of the platform and RNA respectively, $I_{55,plat}$ is the moment of inertia of the platform around the global y axis, EI is the flexural rigidity of the tower and N is the axial load in the tower stemming from the mass of the RNA and the tower weight:

$$N(z_i) = m_{RNA}g + \int_{z_i}^{z_{G,RNA}} m(z)gdz. \tag{4.24}$$

4.4.3 Equations of motion

All the the content from this section follows the developments from Hegseth et al. (2020b), with some more details given for the description of the motion.

The driving dynamic equations of motion for the system under study are:

$$\begin{cases} I_d\Delta\ddot{\varphi} = \Delta Q_A - N_{gear}\Delta Q_G \\ \overline{\mathbf{M}}\Delta\ddot{\mathbf{q}} + \overline{\mathbf{B}}\Delta\dot{\mathbf{q}} + \overline{\mathbf{K}}\Delta\mathbf{q} = \overline{\mathbf{F}}_w + \Delta\overline{\mathbf{T}} + \Delta\overline{\mathbf{M}}_t + \Delta\overline{\mathbf{F}}_D, \end{cases} \tag{4.25}$$

where $I_d = I_{rotor} + N_{gear}^2 I_{generator}$ is the inertia of the drivetrain, seen from the low speed shaft, $\overline{\mathbf{F}}_w$ denotes the generalized hydrodynamic excitation loads, $\overline{\mathbf{T}}$ stands for the generalized thrust force, $\overline{\mathbf{M}}_t$ corresponds to the generalized aerodynamic tilting moment and $\overline{\mathbf{F}}_D$ is the generalized drag force on the tower. The Δ symbol is used in agreement with equation 4.14.

These latter variables are found with:

$$\overline{\mathbf{F}}_w = F_{exc}\mathbf{\Psi}(0) + M_{exc}\mathbf{\Psi}_{,z}(0) \tag{4.26}$$
$$\overline{\mathbf{T}} = T\mathbf{\Psi}(z_{G,RNA}) \tag{4.27}$$
$$\overline{\mathbf{M}}_t = M_t\mathbf{\Psi}_{,z}(z_{G,RNA}) \tag{4.28}$$
$$\overline{\mathbf{F}}_D = \int_{z_{base}}^{z_{G,RNA}} f_D(z)\mathbf{\Psi}(z)dz \tag{4.29}$$

Using a first order Taylor expansion on the terms on the right-hand side of equation 4.25, one can obtain the new form:

$$\begin{cases} I_d\Delta\ddot{\varphi} = Q_{A,v}\left(v_{Q_A} - \sum_{i\in\{1,5,7\}}\Delta\dot{q}_i\right) + Q_{A,\dot{\varphi}}\Delta\dot{\varphi} + Q_{A,\theta}\Delta\theta - N_{gear}\Delta Q_G \\ \overline{\mathbf{M}}\Delta\ddot{\mathbf{q}} + \overline{\mathbf{B}}\Delta\dot{\mathbf{q}} + \overline{\mathbf{K}}\Delta\mathbf{q} = \overline{\mathbf{F}}_w + \sum_{x\in\{\dot{\varphi},\theta,v_T\}} \overline{\mathbf{T}}_{,x}\Delta x + \overline{\mathbf{M}}_{t,v}\Delta v_{M_t} + \overline{\mathbf{F}}_{D,v}\Delta v_T \end{cases} \tag{4.30}$$

assuming that the effective wind speed for the thrust force can be used for the drag force on the tower, which is not exact for the bottom part of the tower which the blades do not reach.

In the state-space framework and based on the degrees of freedom described previously, the state vector is defined by:

$$\mathbf{x}_s = \begin{bmatrix} \mathbf{q} \\ \dot{\mathbf{q}} \\ \dot{\varphi} \end{bmatrix} \tag{4.31}$$

The inputs for the structural system are split into two parts: one from the environmental loads - namely wind and waves - mentioned as disturbances and expressed by $\mathbf{u}_{s,d}$; the other ones correspond to the outputs of the control system - the generator torque Q_G and the collective blade pitch angle θ - and are condensed in the vector $\mathbf{u}_{s,c}$.

The dynamics of the generator and pitch actuator are left for future improvements, which means that no transient effects are captured when the blade pitch angle or the generator torque evolve. This analysis makes use of rotor effective wind speeds, as described in details in Appendix B of Hegseth (2020), in order to express the spatially-varying wind speed with one single scalar. The rotor effective wind speeds, which are dependent on the resultant load (either thrust F_T, tilting moment M_T or aerodynamic torque Q_A), are the uniform wind speeds which leads to the same resultant load as the full wind field. One could interprete them as weighted averages of the wind speed perceived by each blade element. In the current implementation, they are expressed as transfer functions which relate the actual wind speed to the effective one.

Therefore, the control and disturbance input vectors write:

$$\mathbf{u}_{s,c} = \begin{bmatrix} Q_G \\ \theta \end{bmatrix} \tag{4.32}$$

$$\mathbf{u}_{s,d}(\omega) = \begin{bmatrix} \mathbf{v}(\omega) \\ \overline{\mathbf{F}}_w(\omega) \end{bmatrix}, \tag{4.33}$$

where $\mathbf{v} = [v_T \ v_{M_t} \ v_{Q_A}]^\top$, the vector of effective wind speeds.

The rotor speed is the only output $\mathbf{y}_s$ of the structural model, which is provided as an input to the control system.

Now, equation 4.30 can be expressed in a dense form in the state-space formalism, displayed thereafter:

$$\begin{cases} \Delta\dot{\mathbf{x}}_s = \mathbf{A}_s\Delta\mathbf{x}_s + \mathbf{B}_{s,c}\Delta\mathbf{u}_{s,c} + \mathbf{B}_{s,d}\mathbf{u}_{s,d} \\ \Delta\mathbf{y}_s = \mathbf{C}_s\Delta\mathbf{x}_s \end{cases} \tag{4.34}$$

In this system, the state matrix is obtained with:

$$\mathbf{A}_s = \begin{bmatrix} \mathbf{0}_{3,3} & \mathbf{I}_3 & \mathbf{0}_{3,1} \\ -\overline{\mathbf{M}}^{-1}\overline{\mathbf{K}} & -\overline{\mathbf{M}}^{-1}\overline{\mathbf{B}} & \overline{\mathbf{M}}^{-1}\overline{\mathbf{T}}_{,\dot{\varphi}} \\ \mathbf{0}_{1,3} & -\frac{1}{I_d}Q_{A,v}\mathbf{1}_{1,3} & Q_{A,\dot{\varphi}} \end{bmatrix}, \tag{4.35}$$

the control and disturbance input matrices are computed according to:

$$\mathbf{B}_{s,c} = \begin{bmatrix} \mathbf{0}_{3,1} & \mathbf{0}_{3,1} \\ \mathbf{0}_{3,1} & \overline{\mathbf{M}}^{-1}\overline{\mathbf{T}}_{,\theta} \\ -\frac{1}{I_d}N_{gear} & \frac{1}{I_d}Q_{A,\theta} \end{bmatrix}, \quad \mathbf{B}_{s,d} = \begin{bmatrix} \mathbf{0}_{3,3} & \mathbf{0}_{3,3} \\ \left[\overline{\mathbf{T}}_{,v} + \overline{\mathbf{F}}_{D,v}, \overline{\mathbf{M}}_{t,v}, \mathbf{0}_{3,1}\right] & \mathbf{I}_3 \\ \left[0, 0, \frac{1}{I_d}Q_{A,v}\right] & \mathbf{0}_{1,3} \end{bmatrix}, \tag{4.36}$$

and finally the output matrix is simply expressed through:

$$\mathbf{C}_s = [0, 0, 0, 0, 0, 0, 1]\,. \tag{4.37}$$

4.5 Control

The procedure chosen for the controller is closely following the one from Hegseth et al. (2020b). Two controllers are acting independently, depending on the wind speed. For below rated wind speeds, a generator-torque controller is active; for above rated ones, a blade-pitch controller takes over. Both controllers ensure the classical behaviour of the turbine, described in figure 22.

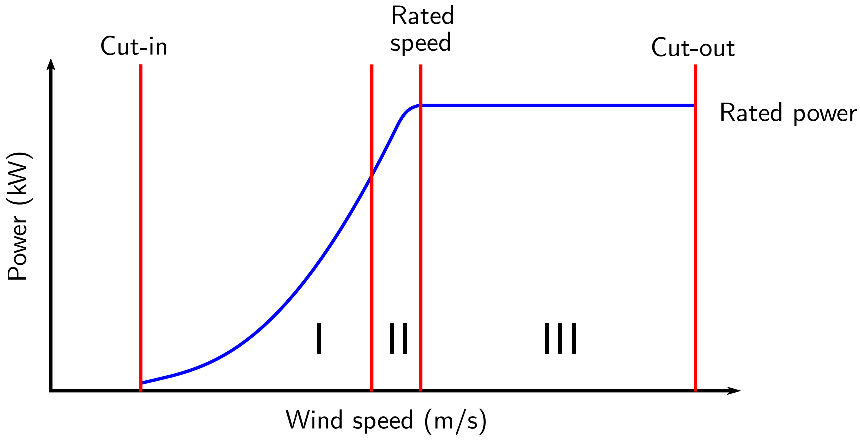

Figure 22: Classical power curve for a wind turbine

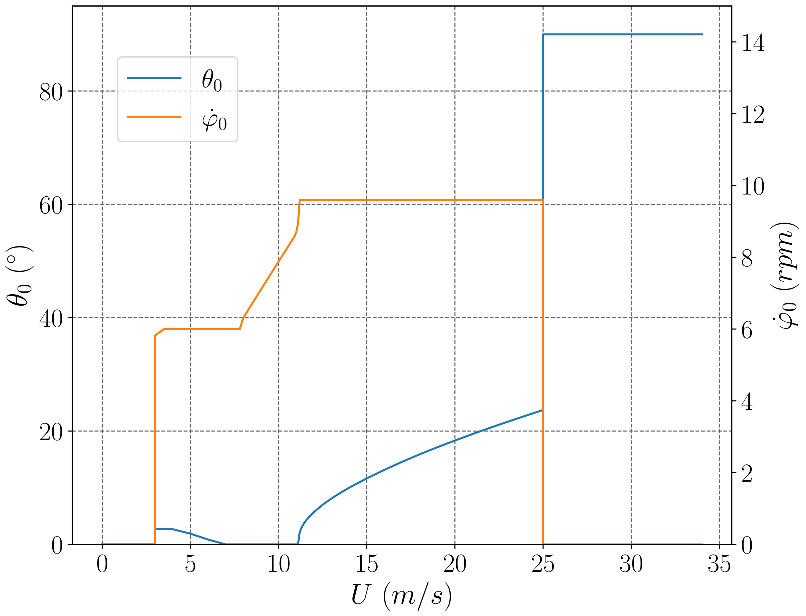

Figure 23: Mean values for θ and $\dot\varphi$

The rotor frequency is first filtered by a first order low-pass filter with corner frequency ω_{LP} to avoid high-frequency excitations of the control system:

$$\ddot\varphi_{LP} + \omega_{LP}\dot\varphi_{LP} = \omega_{LP}\dot\varphi. \tag{4.38}$$

The mean values for the rotor speed and the collective blade pitch angle were generated for the DTU 10 MW turbine by FAST v7, which notably does not account for blade torsion deformation. They are represented in figure 23 and figure 25 gives an overview of the control strategy.

4.5.1 Below rated wind speeds

As introduced above, for below rated wind speeds, the generator torque is set to counterbalance the aerodynamic torque; it is then enforced to evolve quadratically with the rotor speed so as to get a constant tip speed ratio $\lambda = R\dot\varphi_0/U$ which maximizes the power output:

$$Q_G = K_G\dot\varphi_{LP}^2. \tag{4.39}$$

K_G is the generator torque constant, and it can be obtained by:

$$\begin{aligned} K_G = \frac{Q_G}{\dot\varphi_{LP}^2} = \frac{1}{N_{gear}}\frac{P/\dot\varphi_0}{\dot\varphi_{LP}^2} \simeq & \frac{1}{N_{gear}}\frac{1}{2}\rho_{air}AC_pU^3/\varphi_0^3 \\ = & \frac{1}{N_{gear}}\frac{1}{2}\rho_{air}AC_pR^3/\lambda^3 \end{aligned} \tag{4.40}$$

Then, a change in the filtered rotor speed affects the generator torque according to:

$$\Delta Q_G = \frac{\partial Q_G}{\partial \dot{\varphi}}(\dot{\varphi}_0)\Delta\dot{\varphi}_{LP} = 2K_G\dot{\varphi}_0\Delta\dot{\varphi}_{LP} \tag{4.41}$$

In the meantime, the blade pitch angle is constant, equal to its optimum value.

4.5.2 Above rated wind speeds

Opposite the previous case, for below rated wind speeds, the generator torque is left free while the blade pitch angle is controlled by a first order proportional-integral (PI) controller:

$$\Delta\theta = \eta(k_p\Delta\dot{\varphi}_{LP} + k_i\Delta\varphi_{LP}), \tag{4.42}$$

with k_p and k_i the proportional and integral gains of the controller, and η the gain scheduling factor.

4.5.3 State-space formulation

The state-space framework here is such that the input vector is the output of the structural part – i.e. $u_c = y_s = [\dot{\varphi}]$ – and its outputs correspond to the inputs of this same structural part – $y_c = u_s = [Q_G,\ \theta]^\top$. The state vector is chosen to be $x_c = [\varphi_{LP},\ \dot{\varphi_{LP}}]^\top$. The control system is then described as:

$$\begin{cases} \Delta\dot{\mathbf{x}}_c = \mathbf{A}_c\Delta\mathbf{x}_c + \mathbf{B}_c\Delta\mathbf{u}_c \\ \Delta\mathbf{y}_c = \mathbf{C}_c\Delta\mathbf{x}_c \end{cases} \tag{4.43}$$

According to the set of equations which has been described above, the state, input and output matrices write:

$$A_c = \begin{bmatrix} 0 & 1 \\ 0 & -\omega_{LP} \end{bmatrix},\ B_c = \begin{bmatrix} 0 \\ \omega_{LP} \end{bmatrix},\ C_c = \begin{cases} \begin{bmatrix} 0 & 2K_G\dot{\varphi}_0 \\ 0 & 0 \end{bmatrix} & \text{(below rated)} \\ \eta\begin{bmatrix} 0 & 0 \\ k_i & k_p \end{bmatrix} & \text{(above rated)} \end{cases} \tag{4.44}$$

4.5.4 Tuning of the controller

This section is closely following the methodology from J.Jonkman et al. (2009).

For above rated wind speeds, the generator torque is expressed as

$$Q_G(\dot{\varphi}) = \frac{P_0}{N_{gear}\dot{\varphi}}, \tag{4.45}$$

and the aerodynamic torque, which variations with regards to rotor speed are assumed to be negligible, writes

$$Q_A(\theta) = \frac{P(\theta, \dot{\varphi}_0)}{\dot{\varphi}_0}, \tag{4.46}$$

where P and P_0 denote respectively the mechanical power and its rated value.

A first order Taylor expansion of these two expressions leads to:

$$Q_G = \frac{P_0}{N_{gear}\dot{\varphi}_0} - \frac{P_0}{N_{gear}\dot{\varphi}_0^2}\Delta\dot{\varphi}, \tag{4.47}$$

$$Q_A = \frac{P_0}{\dot{\varphi}_0} + \frac{1}{\dot{\varphi}_0}\frac{\partial P}{\partial \theta}\Delta\theta. \tag{4.48}$$

Inserting these two expressions in 4.25 and using 4.42 with $\hat{k} = \eta$, the following second order driving differential equation is derived:

$$\underbrace{I_d}_{m_c}\Delta\ddot{\varphi}_{LP} + \underbrace{\left[\frac{1}{\dot{\varphi}_0}\left(-\frac{\partial P}{\partial \theta}\right)N_{gear}\hat{k}_p - \frac{P_0}{\dot{\varphi}_0^2}\right]}_{c_c}\Delta\dot{\varphi}_{LP} + \underbrace{\left[\frac{1}{\dot{\varphi}_0}\left(-\frac{\partial P}{\partial \theta}\right)N_{gear}\hat{k}_i\right]}_{k_c}\Delta\varphi_{LP} = 0. \tag{4.49}$$

The natural frequency and the damping ratio of the controller are then found by:

$$\omega_{n,c} = \sqrt{\frac{k_c}{m_c}}, \tag{4.50}$$

$$\xi_c = \frac{c_c}{2\sqrt{k_c m_c}}. \tag{4.51}$$

Then, for fixed values of $\omega_{n,c}$ and ξ_c, and neglecting the negative damping term as in Hansen et al. (2005) one can express the two gains according to

$$\hat{k}_i = \frac{I_d\dot{\varphi}_0\omega_{n,c}^2}{N_{gear}\left(-\frac{\partial P}{\partial \theta}\right)}, \tag{4.52}$$

$$\hat{k}_p = \frac{2\xi_c I_d \omega_{n,c}\dot{\varphi}_0}{N_{gear}\left(-\frac{\partial P}{\partial \theta}\right)}. \tag{4.53}$$

With this procedure, the choice of the appropriate combination of $\hat{k}_p$ and $\hat{k}_i$ will depend on the sensitivity of aerodynamic power to rotor-collective blade pitch $\partial P/\partial\theta$, which computation is not straightforward. A common strategy is to approximate this term by a second order polynomial R function of the blade pitch angle:

$$\frac{\partial P}{\partial \theta} = \frac{\partial P}{\partial \theta}(\theta = 0)R(\theta). \tag{4.54}$$

Then, the two gains are expressed as:

$$\hat{k}_i = \overbrace{\frac{I_d\dot{\varphi}_0\omega_{n,c}^2}{N_{gear}\left(-\dfrac{\partial P}{\partial \theta}(\theta = 0)\right)}}^{k_i}\eta(\theta) \tag{4.55}$$

$$\hat{k}_p = \underbrace{\frac{2I_d\xi_c\omega_{n,c}\dot{\varphi}_0}{N_{gear}\left(-\dfrac{\partial P}{\partial \theta}(\theta = 0)\right)}}_{k_p}\eta(\theta), \tag{4.56}$$

with $\eta(\theta) = 1/R(\theta)$ the gain-scheduling factor.

Figure 24 displays the gain-scheduling factor as a function of θ, as fitted by Hansen and Henriksen (2013). It is expressed as

$$\eta = \frac{1}{1 + \theta/K_1 + \theta^2/K_2}, \tag{4.57}$$

with $K_1 = 198.32888°$ and $K_1 = 693.22213°^2$.

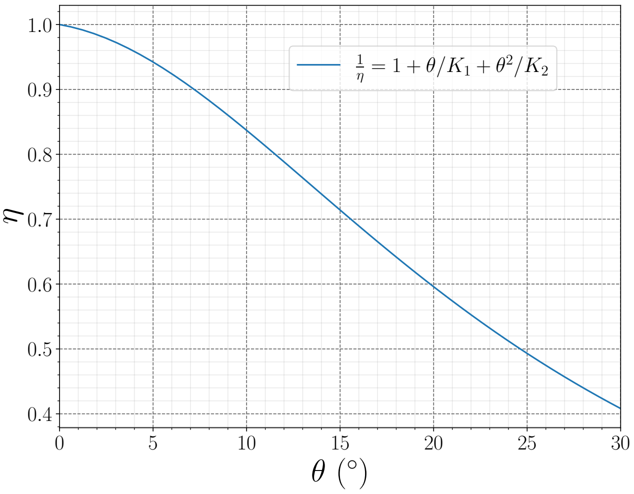

Figure 24: Gain-sheduling factor as a function of the blade pitch angle

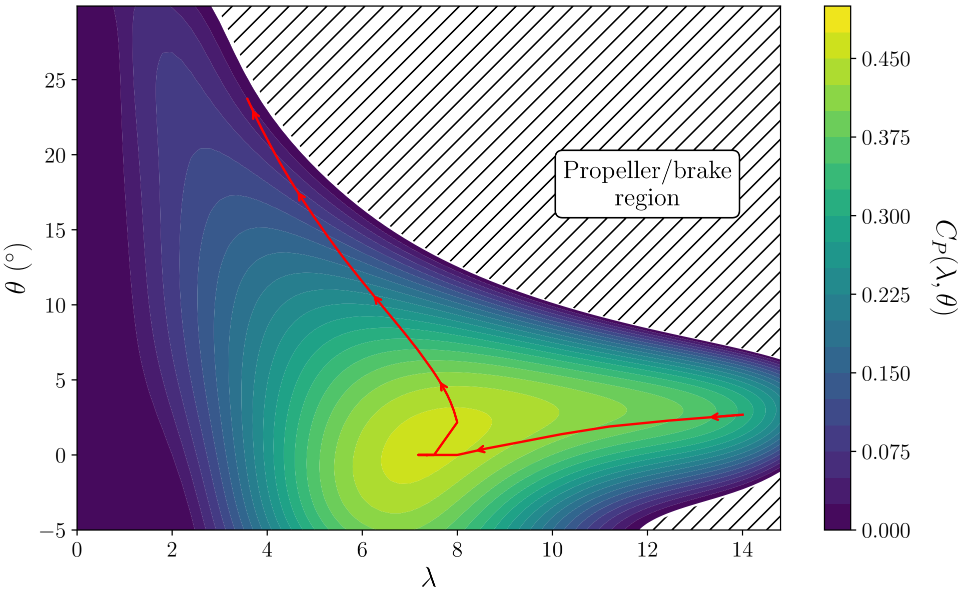

Figure 25: Power coefficient and control strategy (red line) in the plane (λ, θ)

In order to avoid an unstable behaviour of the turbine characterized by negative damping, T.J.Larsen and T.D.Hanson (2007) have proved that the controller needs to be slower than the motions of the structure. Applied to the present case, the controller natural frequency needs to be lower than the pitch and tower bending natural frequencies.

Another approach to access the two gains, which accounts for the dependency over the tip speed ratio as well, would be to compute $\partial P/\partial\theta$ by derivating the function $C_p = f(\lambda, \theta)$ plotted in figure 25 and generated by mean of BEM at the current operating point.

4.6 Global closed-loop system

Since the inputs of the inputs of the control system are the outputs of the structural one, and vice versa, a single closed-loop system can be obtained by building the state vector $\mathbf{x} = \left[\mathbf{x}_s^\top, \ \mathbf{x}_c^\top\right]^\top$:

$$\begin{cases} \Delta\dot{\mathbf{x}} = \mathbf{A}\Delta\mathbf{x} + \mathbf{B}\Delta\mathbf{u}_{s,d} \\ \Delta\mathbf{y} = \mathbf{C}\Delta\mathbf{x} \end{cases} \tag{4.58}$$

where the following matrices are used:

$$\mathbf{A} = \begin{bmatrix} \mathbf{A}_s & \mathbf{B}_{s,c}\mathbf{C}_c \\ \mathbf{B}_c\mathbf{C}_s & \mathbf{A}_c \end{bmatrix}, \quad \mathbf{B} = \begin{bmatrix} \mathbf{B}_{s,d} \\ \mathbf{0} \end{bmatrix}, \quad \mathbf{C} = \mathbf{I}_9. \tag{4.59}$$

In the linear framework used here, a sinusoidal load with frequency ω (which can be either waves or wind presently) will excite the structure and all its state variables at the same frequency. Therefore, the small variations of the state vector over time for a given excitation frequency ω can be written in the complex form

$$\Delta\mathbf{x}(t) = \Re\left(\Delta\tilde{\mathbf{x}}e^{i\omega t}\right). \tag{4.60}$$

Consequently, based on equation 4.58, the transfer function which relates the disturbance vector to the outputs of the system is expressed as:

$$\mathbf{H}(\omega) = \mathbf{C}\left(i\omega\mathbf{I}_9 - \mathbf{A}\right)^{-1}\mathbf{B}. \tag{4.61}$$

H is a 9×6 matrix which components of various types; the following subdivision should make it a bit clearer:

$$\mathbf{H} = \left[\begin{array}{c|c} \mathbf{H}_{q,wind} & \mathbf{H}_{q,wave} \\ \hline \mathbf{H}_{\dot{q},wind} & \mathbf{H}_{\dot{q},wave} \\ \hline \mathbf{H}_{\dot{\varphi},wind} & \mathbf{H}_{\dot{\varphi},wave} \\ \hline \mathbf{H}_{\varphi_{LP},wind} & \mathbf{H}_{\varphi_{LP},wave} \\ \hline \mathbf{H}_{\dot{\varphi}_{LP},wind} & \mathbf{H}_{\dot{\varphi}_{LP},wave} \end{array}\right] \tag{4.62}$$

The response spectral matrix is obtained according to:

$$\mathbf{S}_y(\omega) = \mathbf{H}(\omega) \cdot \mathbf{S}_u(\omega) \cdot \mathbf{H}(\omega)^H \tag{4.63}$$

where $.^H$ denotes the complex transpose or hermitian, and $\mathbf{S}_u$ is the input spectral matrix. This latter is expressed by:

$$\mathbf{S}_u = \begin{bmatrix} \mathbf{S}_{wind} & \mathbf{0}_{3,3} \\ \mathbf{0}_{3,3} & \mathbf{S}_{wave} \end{bmatrix} \tag{4.64}$$

where

$$\mathbf{S}_{wind} = S_{wind}\mathbf{I}_3, \;\; \mathbf{S}_{wave} = S_{wave}\mathbf{I}_3. \tag{4.65}$$

The input spectral matrix $\mathbf{S}_u$ is given as a diagonal matrix here under the assumption that wind and wave processes are uncorrelated.

Ultimately the response spectra for each output are found on the diagonal of the response spectral matrix.

The spectra for the blade pitch angle and the thrust force on the rotor can also be deduced from the list of outputs. Using 4.42 and

$$\Delta T = \sum_{x\in\{\dot{\varphi},\theta,v_T\}} T_{,x}\Delta x, \tag{4.66}$$

we define

$$\begin{aligned}
\mathbf{H}_{\theta,wind} =& \eta_k \left(k_p \mathbf{H}_{\dot{\varphi}_{LP},wind} + k_i \mathbf{H}_{\varphi_{LP},wind}\right)\cdot \mathbf{v}, \quad U \in [U_{cut-in}, U_{cut-out}] && (4.67)\\
\mathbf{H}_{\theta,wave} =& \eta_k \left(k_p \mathbf{H}_{\dot{\varphi}_{LP},wave} + k_i \mathbf{H}_{\varphi_{LP},wind}\right)\cdot \overline{\mathbf{F}}_w, \quad U \in [U_{cut-in}, U_{cut-out}] && (4.68)\\
\mathbf{H}_{T,wind} =& T_{,v}v_T + T_{,\theta}\mathbf{H}_{\theta,wind}\cdot\mathbf{v} + T_{,\dot{\varphi}}\mathbf{H}_{\dot{\varphi},wind}\cdot\mathbf{v} && (4.69)\\
\mathbf{H}_{T,wind} =& T_{,v}v_T + T_{,\theta}\mathbf{H}_{\theta,wave}\cdot\overline{\mathbf{F}}_w + T_{,\dot{\varphi}}\mathbf{H}_{\dot{\varphi},wave}\cdot\overline{\mathbf{F}}_w. && (4.70)
\end{aligned}$$

The corresponding spectra are then obtained according to

$$\begin{aligned}
\mathbf{S}_T =& |\mathbf{H}_{T,wind}|^2 S_{wind} + |\mathbf{H}_{T,wave}|^2 S_{wave} && (4.71)\\
\mathbf{S}_\theta =& |\mathbf{H}_{\theta,wind}|^2 S_{wind} + |\mathbf{H}_{\theta,wave}|^2 S_{wave}. && (4.72)
\end{aligned}$$

4.7 Structural model

4.7.1 Tower

The base of the tower is rigidly connected to the floater, so the motion at node 1 can be deducted from the motion at node 0, origin of the coordinate system and reference point for surge and pitch motions of the floater. Therefore, a master-slave relationship is established between these two, according to

$$\mathbf{v}_1 = \begin{bmatrix} u_1 \\ \theta_1 \end{bmatrix} = \begin{bmatrix} 1 & z_{base} \\ 0 & 1 \end{bmatrix} \cdot \begin{bmatrix} \eta_1 \\ \eta_5 \end{bmatrix} = \mathbf{B}\cdot\mathbf{v}_0, \tag{4.73}$$

where the altitude of the base of the tower is denoted as z_{base}. This relationship sets the tower as a cantilever beam connected to the floater.

One goal is to find the eigenfrequencie of the structure, and their corresponding mode shapes. To do so, one needs to assess the total mass and stiffness matrices of the system.

Each beam element i of the tower, located at altitude z, features the following mass and stiffness matrices:

$$\mathbf{K}_i(z) = \mathbf{K}_{el}(z) = \frac{2EI(z)}{l^3}\begin{bmatrix} 6 & -3l & -6 & -3l \\ -3l & 2l^2 & 3l & l^2 \\ -6 & 3l & 6 & 3l \\ -3l & l^2 & 3l & 2l^2 \end{bmatrix}, \tag{4.74}$$

$$\mathbf{M}_i(z) = \frac{\rho_{steel}A(z)l}{420}\begin{bmatrix} 156 & -22l & 54 & 13l \\ -22l & 4l^2 & -13l & -3l^2 \\ 54 & -13l & 156 & 22l \\ 13l & -3l^2 & 22l & 4l^2 \end{bmatrix}, \tag{4.75}$$

where E is steel's Young's modulus, I is the second moment of area of the cross section, A is the cross section area and l is the length of one element $l = H_{tower}/n$ $(H_{tower} = z_{hub} - z_{base})$

To account for the compression load P due to the tower own weight, one could add to the element stiffness the geometric stiffness defined as

$$\mathbf{K}_g = \frac{P}{30l}\begin{bmatrix} 36 & -3l & 36 & -3l \\ -3l & 4l^2 & 3l & -l^2 \\ 36 & 3l & 36 & 3l \\ -3l & -l^2 & 3l & 4l^2 \end{bmatrix}. \tag{4.76}$$

Especially at the base of the tower, the compression load is $P = (m_{RNA} + m_{tower})\, g = 18.973\,\mathrm{MN}$ so the ratio between the first diagonal terms for instance, with $n = 10$, is:

$$\frac{\mathbf{K}_{g,11}}{\mathbf{K}_{el,11}} = \frac{PH_{tower}^2}{10EIn^2} \simeq 2.4 \times 10^{-5}. \tag{4.77}$$

This quantity being very low compared to 1, it will be neglected.

The fore-aft bending moment at the tower base is accessed using Euler-Bernoulli beam theory, based on the tower deflection due to the flexible mode only (the rigid body modes do not contribute to any internal forces in the structure). Its expression is found as

$$\begin{aligned} M_y(z = z_{base}, t) &= -EI_y(z_{base})\frac{d^2w}{dz^2}(z_{base}, t) \\ &= -EI_y(z_{base})\frac{d^2\psi_7}{dz^2}(z_{base})q_7(t), \end{aligned} \tag{4.78}$$

where the coordinate system for a tower section is defined in figure 26.

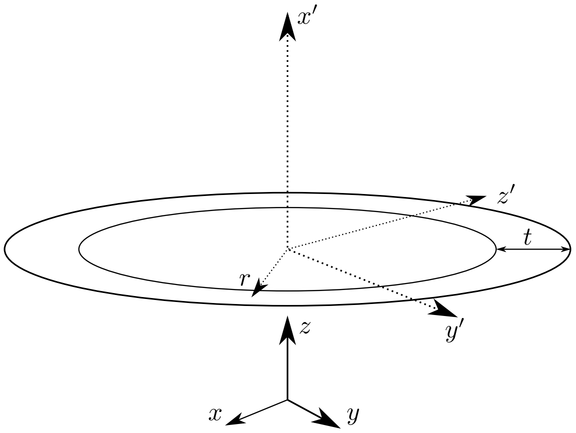

Figure 26: Global (filled lines) and local (dotted lines) coordinate systems in a tower section

This latter expression defines a transfer function:

$$H_{M_y} = -EI_y \frac{d^2\psi_7}{dz^2}(z_{base}). \tag{4.79}$$

Figure 27 gives an insight of it along the tower.

Its spectrum is then obtained as

$$S_{M_y}(\omega) = H^2_{M_y} S_{y,q_7}, \tag{4.80}$$

where S_{y,q_7} is the response spectrum of the bending degree of freedom.

Besides, the axial stress in a tower section is equal to

$$\sigma_x = \frac{N_x}{A} + \frac{M_y}{I_y}\frac{D}{2}, \tag{4.81}$$

where N_x is the normal load at the given cross section due to the tower and RNA weights, and $A = \pi/4\,(D^2 - (D-2t)^2)$ the tower cross section at altitude z.

Hence the corresponding transfer function

$$H_{\sigma_x} = -E\frac{D}{2}\frac{d^2\psi_7}{dz^2}(z_{base}). \tag{4.82}$$

4.7.2 Mooring system

$\mathbf{K}_{moor}$ is found by linearization of the restoring forces around the mean position of the platform for each environmental condition (see section 2.4 from de Renty de Renty (2020)).

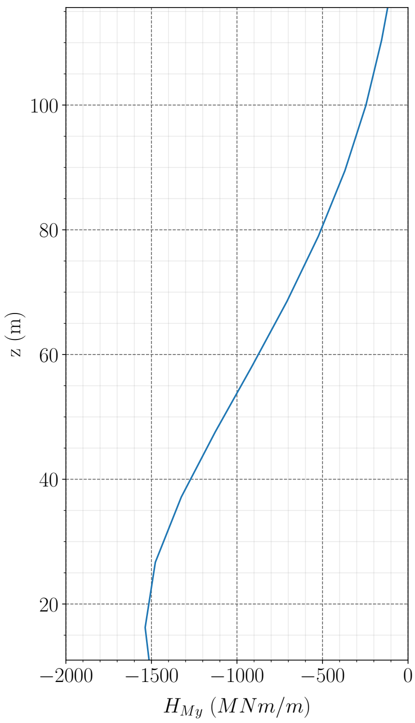

Figure 27: Transfer function for the bending moment over the tower lenght

This formulation should be sufficient for the mean position of the platform but will not be able to capture dynamic effects of the mooring lines, notably structural damping.

No hydrodynamic loads are applied on the lines.

4.7.3 Floater

For the platform, the stiffness matrix is obtained as

$$\mathbf{K}_{plat} = \mathbf{K}_{moor} + \mathbf{K}_{hydro}, \tag{4.83}$$

with $\mathbf{K}_{hydro}$ full of zeros except for the pitch restoring:

$$\mathbf{K}_{hydro,55} = \rho g I_{wp,y} + \rho g \nabla z_B - m_{plat} g z_{G,plat}. \tag{4.84}$$

However, in order to account not only for the mass of the platform only but also for the destabilizing term due to the presence of the turbine on top of it, the restoring coefficient in pitch is corrected according to:

$$\mathbf{K}_{hydro,55} = \rho g I_{wp,y} + \rho g \nabla z_B - (m_{plat} + m_{tower} + m_{RNA}) g z_{G,tot}. \tag{4.85}$$

The mass matrix of the platform is expressed as

$$\mathbf{M}_{plat} = \begin{bmatrix} m_{plat} & m_{plat} z_{G,plat} \\ m_{plat} z_{G,plat} & I_{yy,plat} \end{bmatrix} \tag{4.86}$$

and all the quantities are again detailed in de Renty (2020).

Finally, one needs to include the added mass matrix $\mathbf{A}(\omega)$ in the total mass matrix; its asymptotic value at high frequency $\mathbf{A}_\infty$ will be used.

4.7.4 Eigenvalue analysis

Now, the element matrices are assembled into global mass and stiffness matrices $\mathbf{M}$ and $\mathbf{K}$ with respect to the numbering of the nodes in figure 14. The reduction of the number of dofs, due to the master-slave connection between the floater and the tower gives rise to the following update of the matrices:

$$\tilde{\mathbf{M}} = \mathbf{H}^\top \cdot \mathbf{M} \cdot \mathbf{H} \tag{4.87}$$

$$\tilde{\mathbf{K}} = \mathbf{H}^\top \cdot \mathbf{K} \cdot \mathbf{H} \tag{4.88}$$

where the transformation matrix $\mathbf{H}$ is defined as

$$\mathbf{H} = \left[\begin{array}{c|c} I_2 & \\ B & \\ \hline & I_{n-4} \end{array} \right], \tag{4.89}$$

with I_p the identity matrix of order p.

For a structure under free oscillation, the displacement pattern at the nodes can be exressed as $r(z,t) = \boldsymbol{\Phi}(z)\cos(\omega t + \alpha)$ where Φ is the amplitude of the motion, ω is the oscillation frequency and α is a given phase angle Then, the mode shapes and their corresponding eigenfrequencies are found solving the eigenproblem

$$(\tilde{\mathbf{K}} - \omega^2 \tilde{\mathbf{M}}) \cdot \boldsymbol{\Phi} = 0. \tag{4.90}$$

The eigenfrequencies for this problem are recorded in table 3. The first three frequencies, sorted by increasing magnitude, correspond to surge motion, pitch motion and bending of the tower. It should be noted that since the mooring stiffness varies with the environmental conditions, the eigenfrequencies also vary according to these conditions. However, only the surge motion is affected in a significant way, so the third digit should be taken cautiously.

mode number	1	2	3
ω (rad s^{-1})	0.035	0.235	4.90

Table 3: First eigenfrequencies of the system, using a finite element model

These values should be compared to all the excitation frequencies applied on the structure, stemming from the waves, the wind and the rotating blades. Figure 28

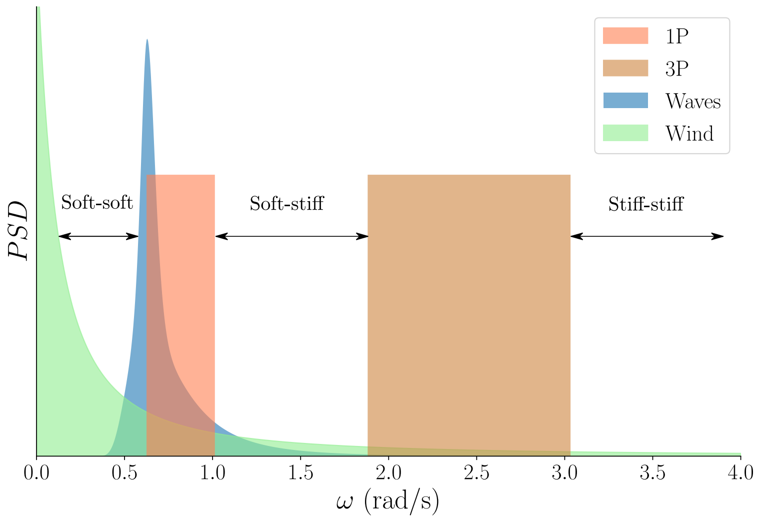

Figure 28: Available frequency ranges for the motions of the turbine
(Adapted from C.L.Bakmar (2009))

displays the available regions of the frequency axis that are left free. The spectra for the wind and the waves are respectively a Kaimal and a Jonswap spectra, with parameters arbitrarily chosen, for illustration purposes only.

As one can observe, the pitch and tower bending frequencies are well located in the regions almost free of any excitation. For the surge motion, the eigenfrequency will inevitably lie in a region slightly excited by wind. For OO-Star, the design of the tower is in the stiff-stiff region.

As a comparison, deliverable D4.5 A.Pegalajar-Jurado et al. (2018) provides the following eigenfrequencies for the structure, which is however entirely made of concrete:

mode number	1	2	3
ω (rad s^{-1})	0.034	0.199	4.687

Table 4: First eigenfrequencies of the system from A.Pegalajar-Jurado et al. (2018)

As a verification of the agreement between the modal formulation and the more classic one developed in section 4.7.4, the eigenvalues of the system are computed again based on the generalized matrices; they are stored in table 5.

mode number	1	2	3
ω (rad s^{-1})	0.035	0.228	4.46

Table 5: Eigenfrequencies of the system from generalized matrices

The agreement between the two models is satisfying; the eigenvalues for surge motion match very well; for pitch, the value from the generalized approach is 3% lower than its classical counterpart while for the bending mode, really sensitive to its polynomial fit, a -9% decrease is observed (the reference being the classical approach). One should keep in mind that the generalized formulation, which only accounts for the first three modes, should be a bit less accurate than its classical counterpart which considers additional modes. However, the former surpasses the latter in terms of computational efficiency.

4.8 Fatigue analysis

Fatigue analysis is an essential aspect of the study of any structure to assess its lifetime. Here, linear cumulative damage is assumed, which is to say that the damage resulting from N stress cycles with p amplitudes $\Delta\sigma_i$ individually repeated n_i times is:

$$D = \sum_{i=1}^{p} \frac{n_i}{N_i} \tag{4.91}$$

where N_i is the number of cycles of amplitude $\Delta\sigma_i$ until failure of the structure and $\sum_{i=1}^{p} n_i = N$.

The data N_i are provided by the S-N curves in air from DNV-GL (2014), displayed in figure 29. The focus is made on axial stress only.

The damage is computed by mean of Dirlik's formula from Dirlik (1985). Based on the stress response spectrum and some empirical factors, it fits to the power density function of the stress cycles a combination of an exponential and two Rayleigh distributions. The damage over a time period of T seconds, with a wall thickness t is expressed as

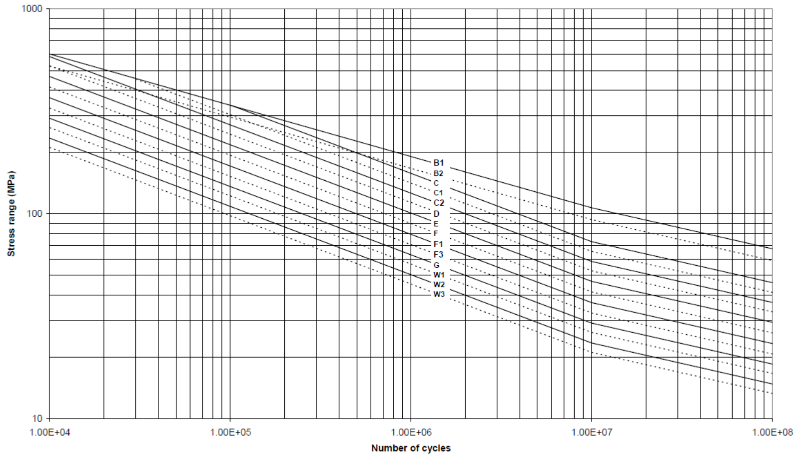

Figure 29: S-N curves in air from DNV-GL (2014)

$$\begin{aligned} D_{DK} = \frac{v_p T}{K}(2\sqrt{m_0})^m (G_1 Q^m \Gamma\left(1+m\right) \\ + (\sqrt{2})^m \left(G_2 R^m + G_3\right)\Gamma(1+\frac{m}{2})) \left(\frac{t}{t_{ref}}\right)^{mk}, \end{aligned} \tag{4.92}$$

where

$$\begin{aligned} G_1 &= \frac{2\left(x_m - \alpha_2^2\right)}{1+\alpha_2^2},\ G_2 = \frac{1-\alpha_2 - G_1 + G_1^2}{1-R},\ G_3 = 1 - G_1 - G_2, \\ Q &= \frac{1.25\left(\alpha_2 - G_3 - G_2 R\right)}{G_1},\ R = \frac{\alpha_2 - x_m - G_1^2}{1 - \alpha_2 - G_1 + G_1^2} \end{aligned} \tag{4.93}$$

and

$$\alpha_2 = \frac{m_2}{\sqrt{m_0 m_4}},\ x_m = \frac{m_1}{m_0}\sqrt{\frac{m_2}{m_4}},\ v_p = \frac{1}{2\pi}\sqrt{\frac{m_4}{m_2}}. \tag{4.94}$$

In equation 4.92, the parameters m and $K = \bar{a}$ are defining the part of the S-N curve below $N = 10^7$ cycles. t_{ref} and k are thickness reference parameters provided in DNV-GL (2014).

In the previous equations, m_n refers to the n^{th} moment of the stress response spectrum, defined by

$$m_{n,X} = \int_0^\infty \omega^n S_X(\omega) d\omega. \tag{4.95}$$

Summing the contribution of the 21 sea states listed in table 18 from Krieger et al. (2015a) (replicated in table 2 from de Renty (2020)) weighted by their corresponding probability of occurrence, one can access the 25 year fatigue damage for the structure.

4.9 SIMA model

A high-fidelity hydro-aero-servo-elastic numerical model of OO-Star has been provided and extended: it will be used to challenge the linear model developed here. This model was built on SIMA (Advanced Analyses of Marine Operations and Floating Systems), software developed notably at Marintek.

The hydrodynamic loads are based on the added mass, damping and hydrostatic stiffness matrices computed by HydroD. Viscous effects are modelled with Morison's equation, with the same subdivision of the floater as in the model developped in this report.

	Structural model	External loads
Blades	Beam elements with 26 foil-shaped cross sections	Turbulent wind with wind shear; BEM with Glauert's and Prandtl's corrections, dynamic wake, dynamic stall, tower shadow, skewed wake
Hub	Rigid body	No wind loads
Nacelle	Beam elements	No wind loads
Tower	Beam elements with 27 circular cylinder cross sections	Drag forces due to turbulent wind (in rotor region), or mean wind (below lowest blade passing point)
Hull	Rigid body; master slave connections to tower base and mooring lines	Potential flow theory + drag forces (same model as in figure 17)
Mooring lines	Beam elements made of a constant circular cylinder cross sections	Morison equation
Anchors	Fixed along the 6 dofs; flat bottom contact at the seabed	

Table 6: Details of the model in SIMA

The blades and the tower are modelled with beam elements. The hull is a rigid body connected to the tower by a master-slave link.

The wind conditions are given as a non-homogeneous three dimensional wind field generated with TurbSim, with the Normal Turbulence Model (NTM) implemented for a class B turbine. A Kaimal spectrum is used and a power law profile with exponent 0.14 models the vertical wind shear.

The controller for the DTU 10 MW is included with some adjustments made to account for the fact that the turbine is a floating one.

The model is detailed in figure 30 and in table 6. The black dots are supernodes between which are drawn lines, made of beam elements. The dotted lines represent master-slave connections between nodes. Three rigid bodies are added to the slender system: the hub, the nacelle and the floater (connected to a dummy line in order to include its properties in the force model). The shaft is split into two segments separated by a flex joint replicating the generator torque: on the left side is the rotating low speed shaft; on the right side, the high speed shaft is motionless. The contacts with the seafloor at the anchor location are defined by normal stiffness coefficient.

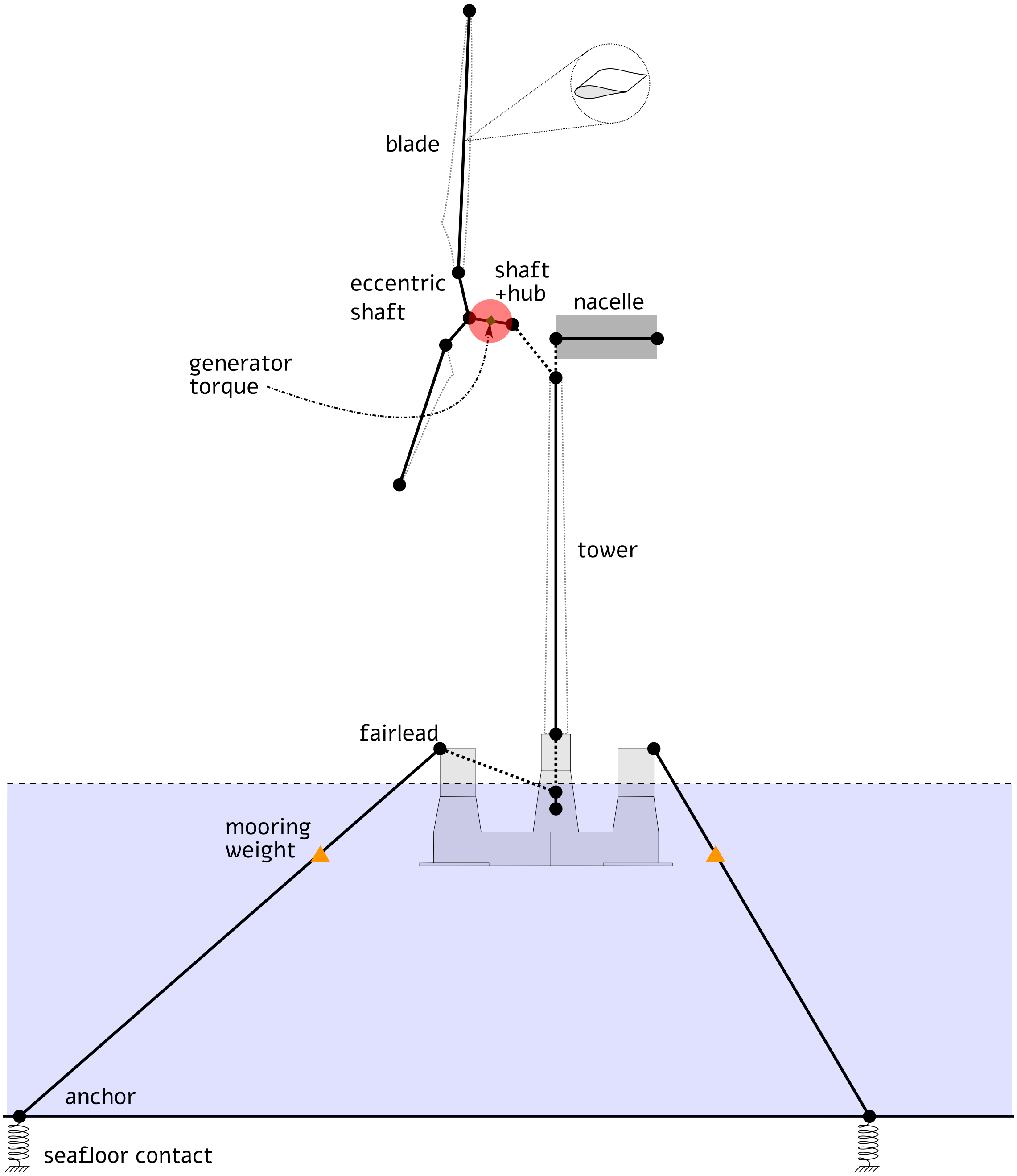

Figure 30: SIMA environment

4.10 Model validation

To check the validity of the previously defined model, the Response Amplitude Operators (RAO) for surge and pitch motions were compared to those computed by HydroD/WAMIT. These RAOs will be denoted as 'wave RAOs' to highlight the fact that they reflect the behaviour of the structure under wave loads only.

The geometry of the meshed structure, its total mass, radius of gyration r_y around the y-axis (defined such as $I_{yy} = \rho_w \nabla r_y |r_y|$) and center of gravity (CoG), including the turbine, were provided to HydroD as well as the mooring stiffness matrix for $U = 0\,\mathrm{m\,s^{-1}}$. Moreover, since WAMIT does not take into account viscosity, the drag coefficients were set to zero in SIMA and in the linear model to make the comparison easier.

In SIMA, a set of monochromatic waves with frequencies in the wave frequency range was provided as an input; the responses in surge and pitch were then Fourier transformed and the corresponding amplitude was reported.

The RAOs are plotted in figure 31; as one can see the match is really good for for both motions, with a slight shift on the pitch natural period. For surge, with natural frequency at $0.035\,\mathrm{rad\,s^{-1}}$, a jump in the RAO is observed at roundabout $0.2\,\mathrm{rad\,s^{-1}}$ corresponding to pitch natural frequency. Symmetrically, a peak is observed in the pitch RAO at surge natural frequency. These two behaviours are due to coupling effects between the two motions. They are however significantly damped once viscous damping is accounted for.

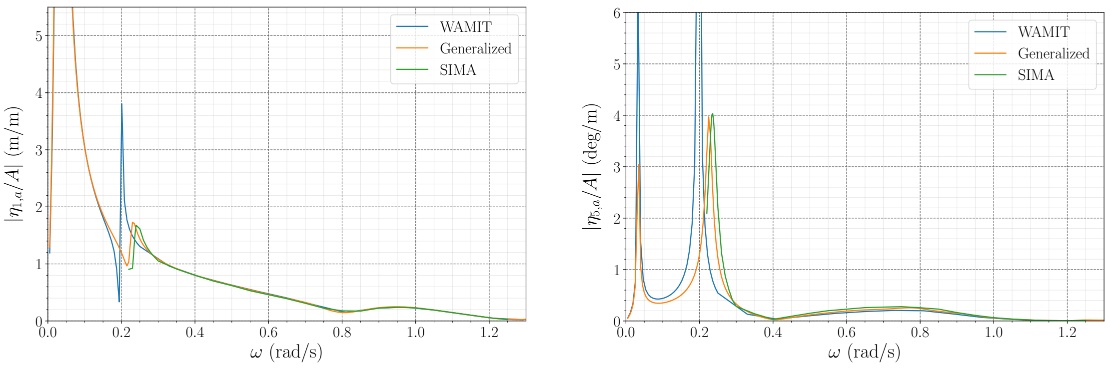

(a) Surge (b) Pitch

Figure 31: Comparison of the transfer functions from the linear model and WAMIT

5 Analysis and optimization of OO-Star

In this section, the previously exposed set up will be used to perform the analysis of the floater with variable geometries and environmental conditions. Ultimately, some optimization runs will be performed.

5.1 Model architecture in OpenMDAO

The model layout is diplayed in figure 32 following the Extended Diagram Structure Matrix (XDSM) developed in Lambe and Martins (2012). As the name suggests, this layout is an extension of the diagram structure matrix, also known as "n^2 diagram", widely used in engineering and project management in the second half of 20^{th} century. This one is specifically aimed at describing an optimization framework.

The rounded blue box stands for the optimizer, green boxes on the diagonal are the different analysis steps of the process, grey parallelograms are input and output data for each step and white parallelograms are fixed input parameters. The lines define the dependecies between the data. In the upper triangular part, the diagram reads from the top to the bottom and from left to right. In the lower triangular part, the direction of reading is the opposite to the previously exposed, meaning from the bottom to the top and from right to left, in such a way that the diagram defines a closed loop system. One should notably notice the presence of the iterative evaluation of the linear viscous damping coefficient with a subdiagonal box.

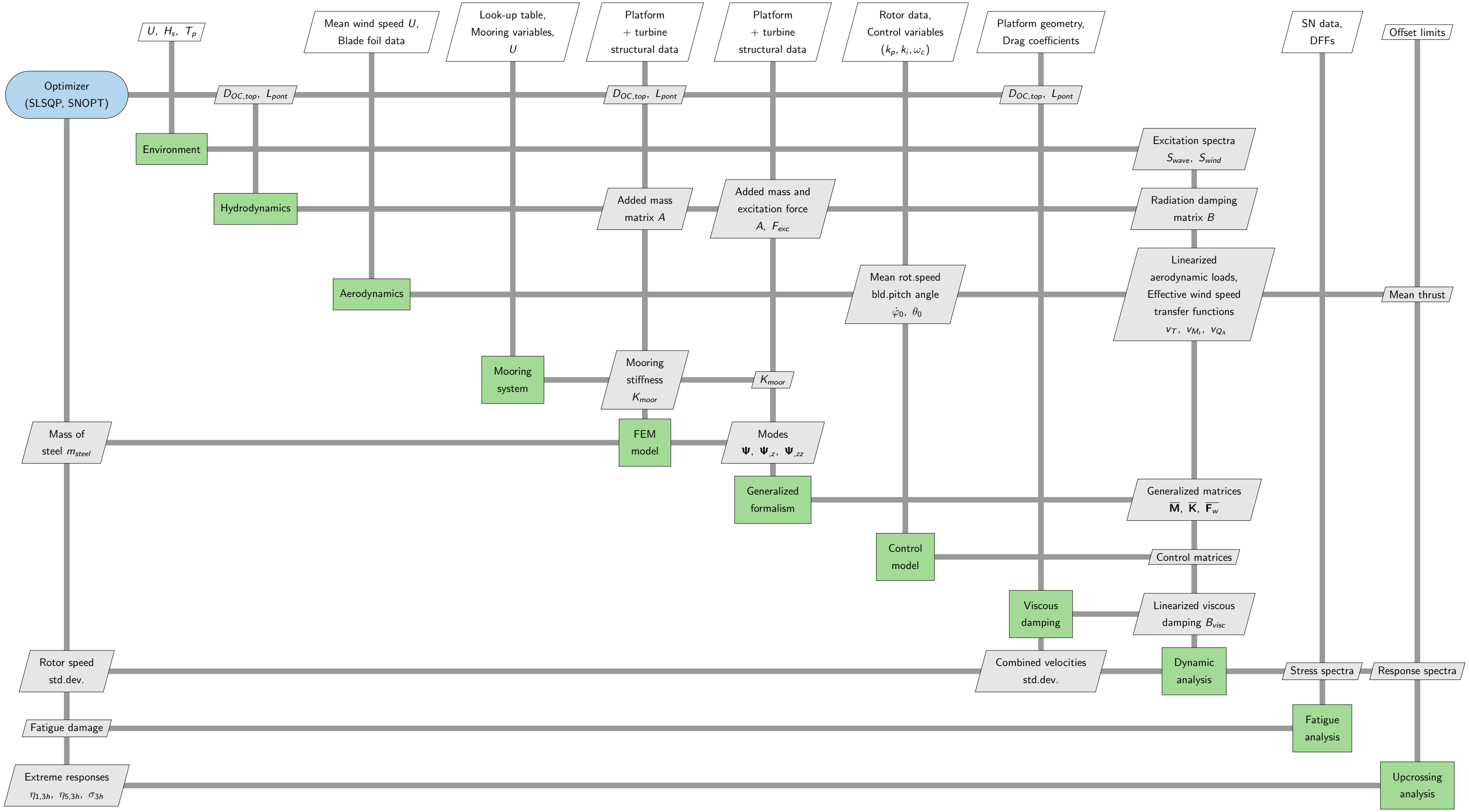

Figure 32: XDSM diagram of the model

5.2 Study of three different designs

Here, three different floaters, with variable pontoon length L_{pont} and top diameter of the outer columns $D_{OC,top}$, will be analysed. The purpose of it is to check the ability of this framework to capture some first trends in the behaviour of the structure.

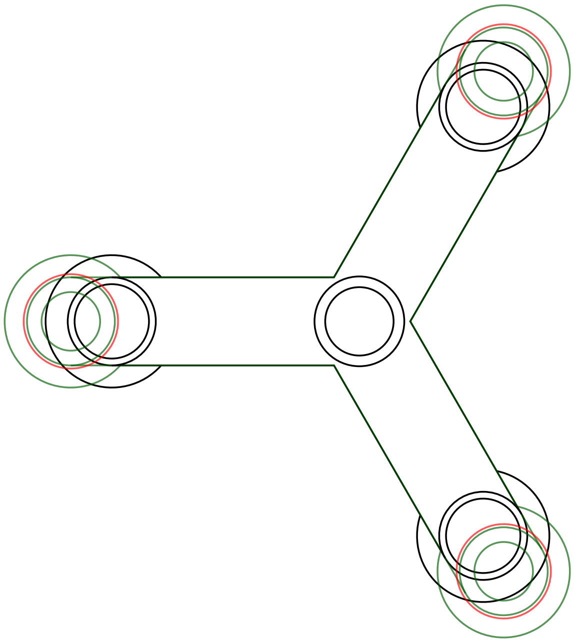

Figure 33: Top view of the three floaters: D1 in black, D2 in red, D3 in green.

5.2.1 Presentation

The three floaters selected for this study are defined as follows: D1 is the original design of the platform, D2 features an increase by 20% of L_{pont} and $D_{OC,top}$, and D3 has L_{pont} increased by 20% and $D_{OC,top}$ decreased by 20%. The numerical values for the geometry are presented in table 7 and figure 33 gives an insight of their aspect.

For each design, the linear model was run once, without optimization, under three different environmental conditions defined in Krieger et al. (2015b) for the fatigue analysis, and reported in table 8.

For the JONSWAP spectrum, the parameter $\gamma = 3.3$ was used.

In the meantime, 1-hour time-domain simulations for these three designs were run in SIMA. The spectra were directly computed from the time series.

Design	D1	D2	D3
L_{pont} (m)	37	44.4	44.4
$D_{OC,top}$ (m)	13.4	16.08	10.72

Table 7: Definition of the three designs for OO-Star

Name	U ($\mathrm{m\,s^{-1}}$)	H_s (m)	T_p (s)	(ω_p) ($\mathrm{rad\,s^{-1}}$)
EC1	8	1.67	8	0.785
EC2	12	2.2	11	0.571
EC3	20	8.31	14	0.449

Table 8: Definition of the three environmental conditions

	Surge	Pitch	Bending
D1	0.0350	0.228	4.46
D2	0.0328	0.316	4.19
D3	0.0344	0.190	4.24

Table 9: Eigenfrequencies from generalized matrices for each design in $\mathrm{rad\,s^{-1}}$

The results to compare are the motion spectra of the system, along with the spectra for the bending moment at the base of the tower, the rotor speed, the collective blade pitch angle and the thrust force over the rotor

As an indicator, table 9 gives the values of the eigenfrequencies from the generalized matrices for each design. It is interesting to notice how much the pitch motion varies with the geometry.

5.2.2 Results

SIMA's results are plotted with a solid line, while the ones from the linear model are represented by a dashed line.

Surge The spectra for surge are displayed in figure 34. Each row stands for one design *D*, specified on the left, and each column corresponds to one environmental condition *EC*. For each combination (*D*,*EC*), two windows are used; the one on the left displays the region of the spectrum with most energy; the window on the right displays the whole region of interest in logarithmic scale so as to highlight the different orders of magnitude of the peaks.

Wind is responsible for the excitation at low frequencies ($\omega \leq 0.1\,\mathrm{rad\,s^{-1}}$) while waves excite the structure around the peak frequency ω_p which varies depending on the sea-state, from $0.45\,\mathrm{rad\,s^{-1}}$ for EC3 to $0.79\,\mathrm{rad\,s^{-1}}$ for EC1 (see table 8). In each configuration, three main peaks are observed: one located at surge natural frequency, another one at pitch natural frequency and the last one located at wave peak frequency.

For the first two environmental conditions, the first peak is overestimated compared to SIMA's analysis; for EC3, the trend is slightly reversed, even though the order of magnitude between SIMA and the linear model is the same, but one should notice that the height of the peak in this case is significantly smaller than for EC1 and EC2.

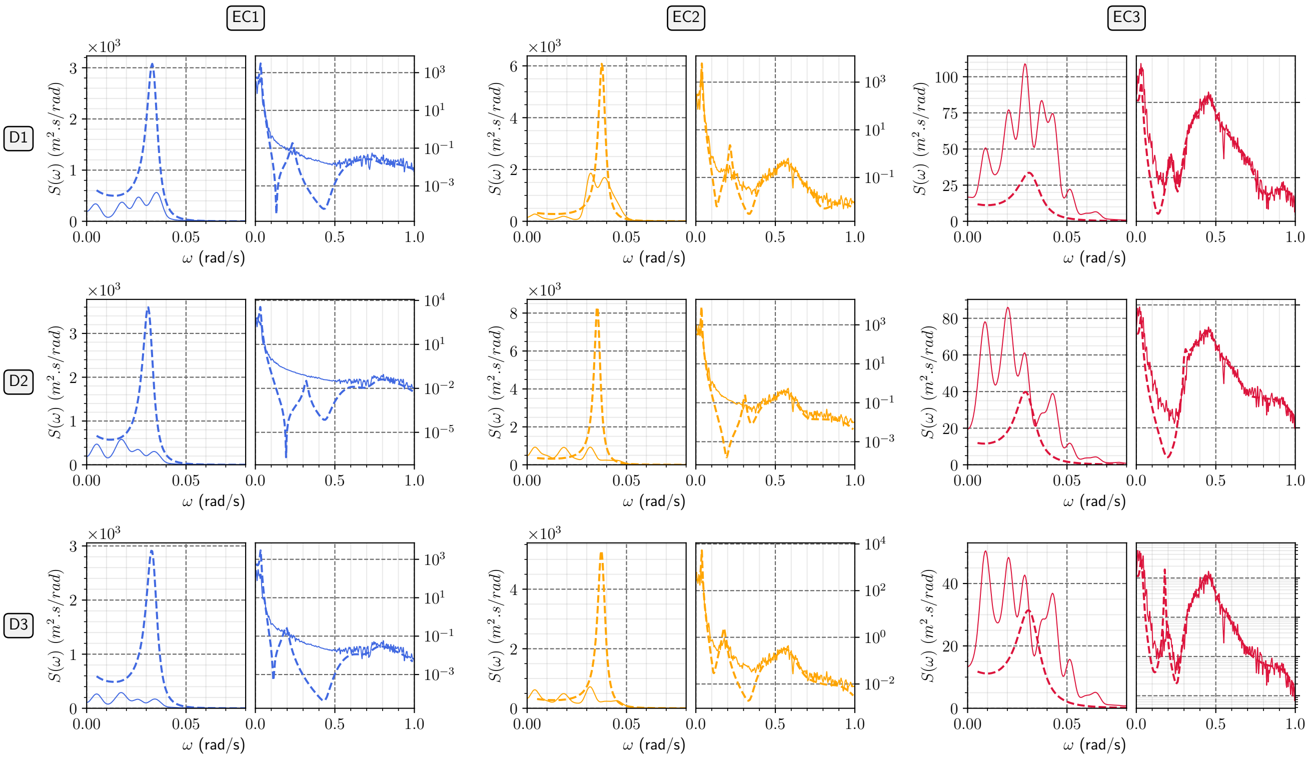

Figure 34: Spectra for surge motion

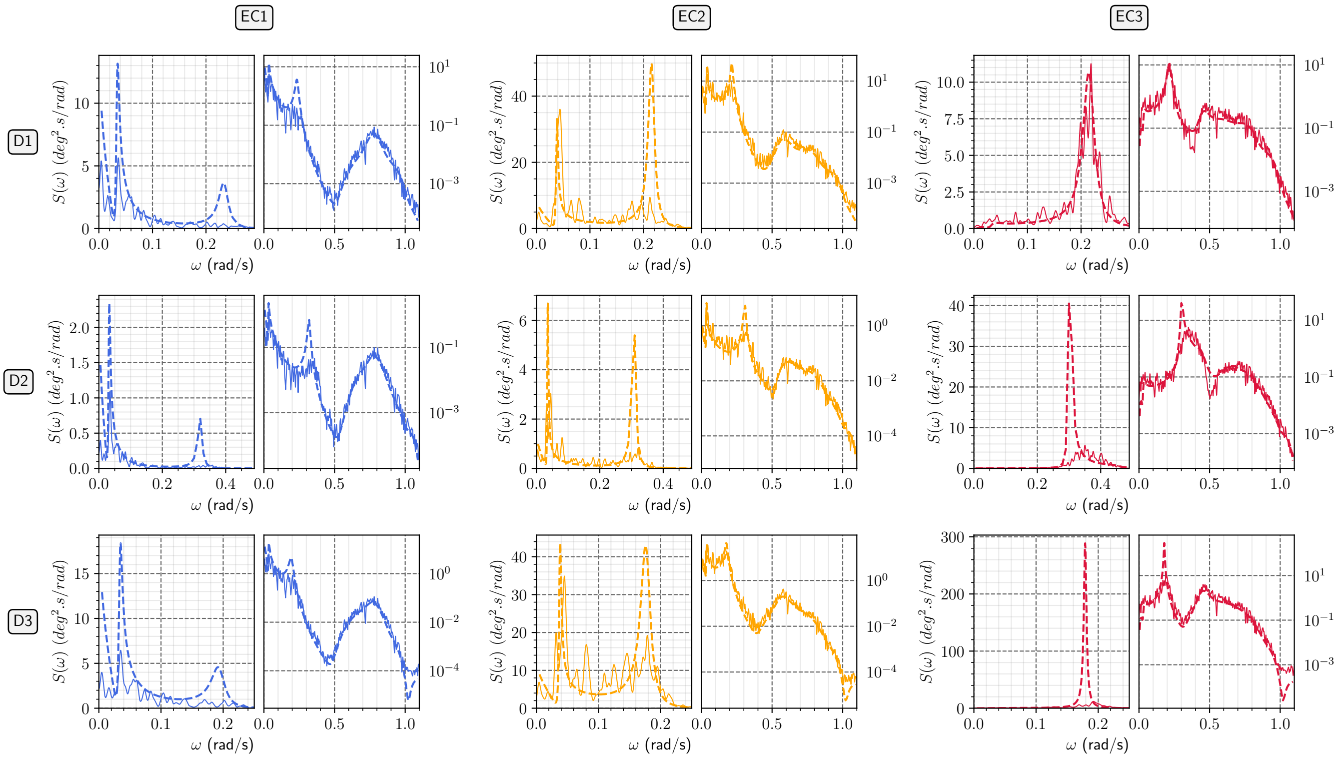

Figure 35: Spectra for pitch motion

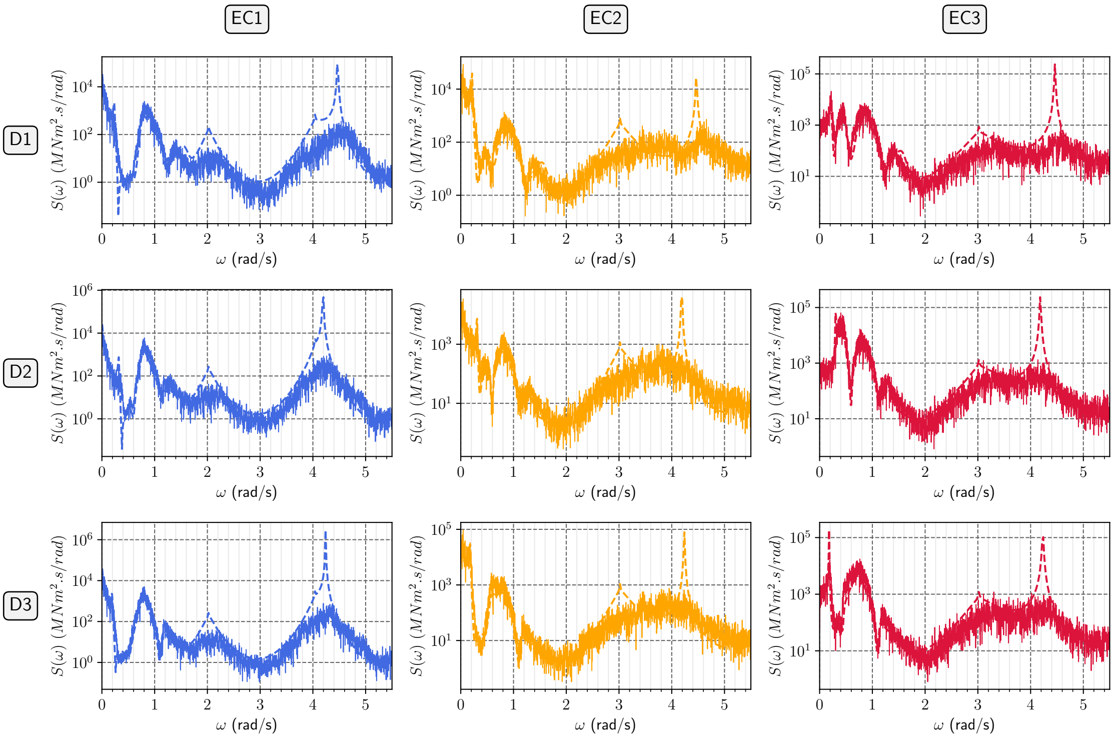

Figure 36: Spectra for the bending moment at the base

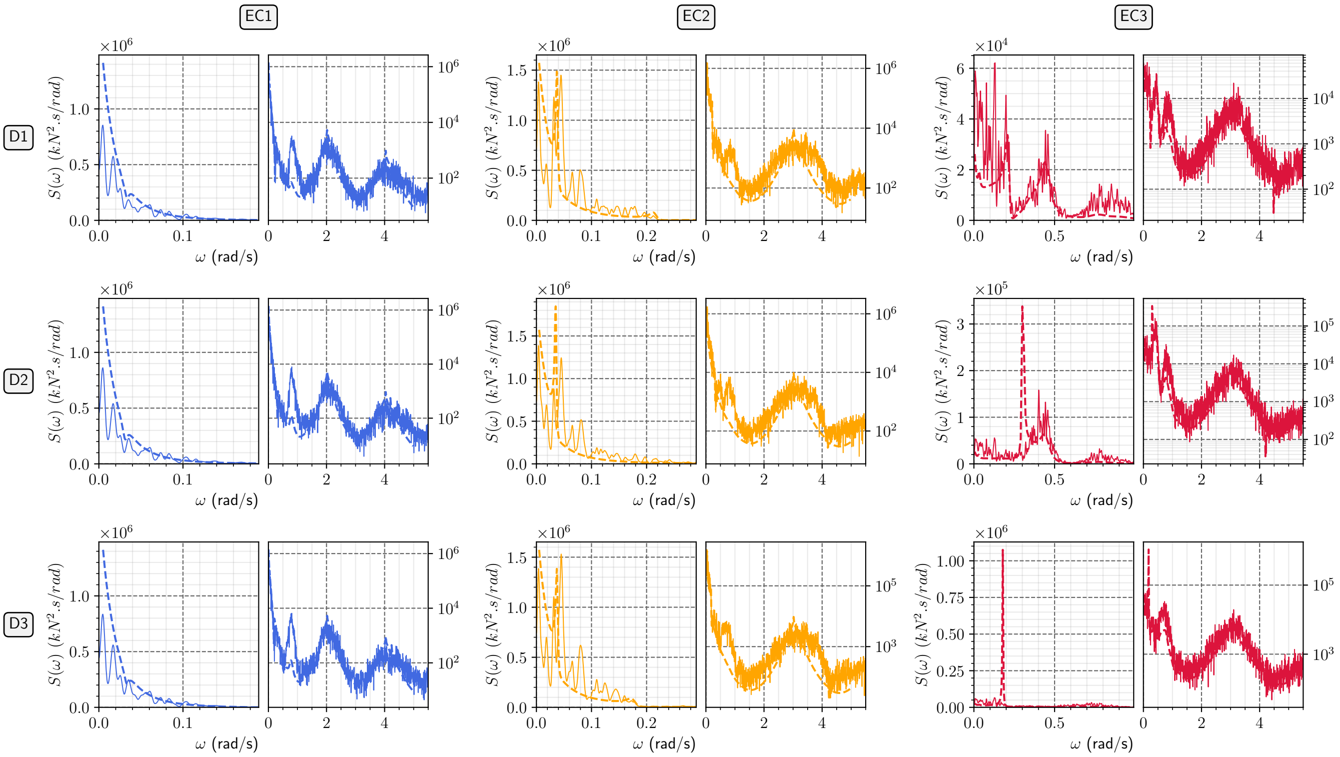

Figure 37: Spectra for the thrust force

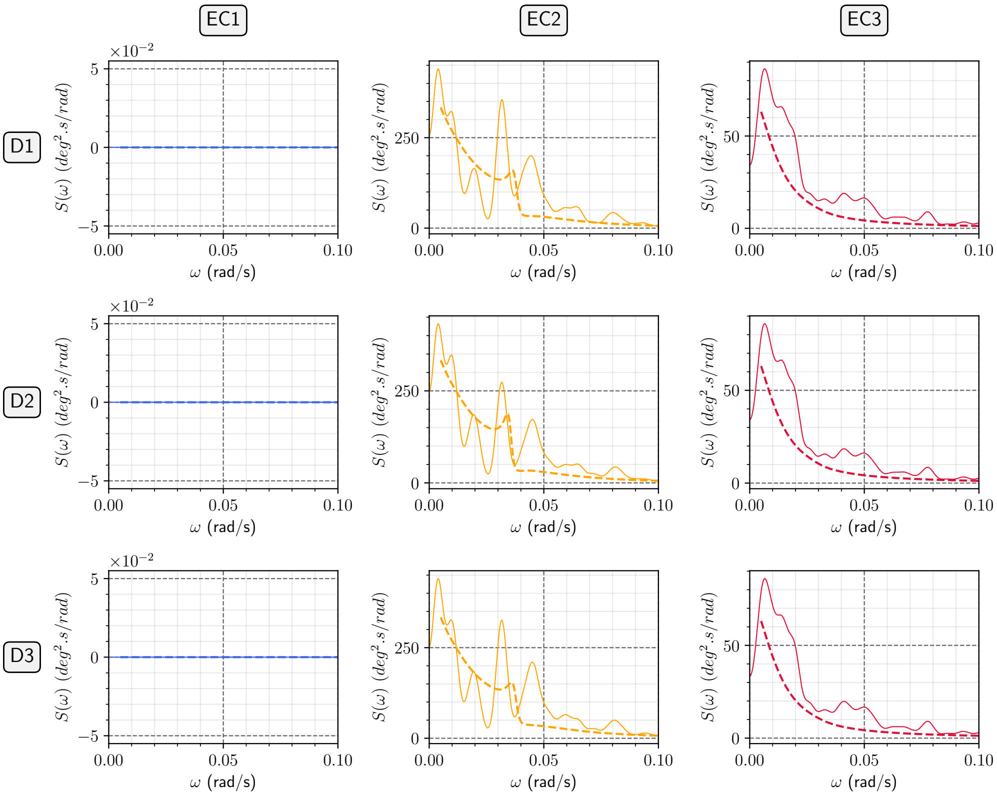

Figure 38: Spectra for the collective blade pitch angle

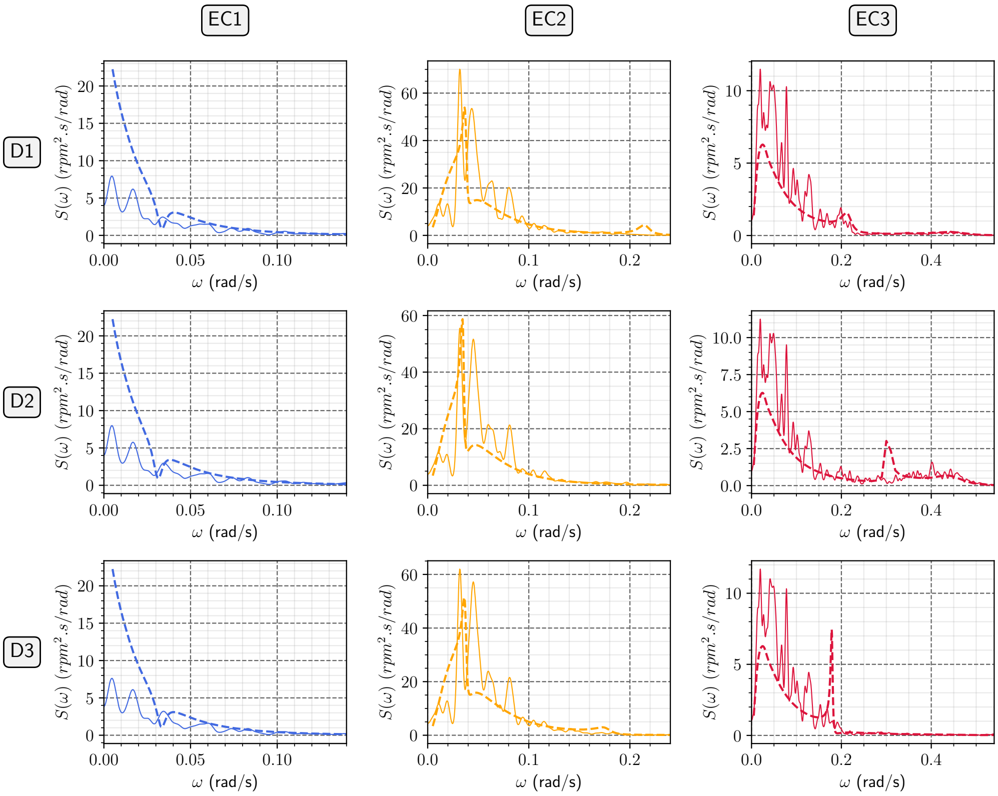

Figure 39: Spectra for the rotor speed

In that region region of the spectrum and for this specific motion (surge), the location of the peak is very dependent on the value of the mooring stiffness, while its magnitude mostly depend on viscous damping on the floater and on the dynamics of the mooring system. Due to the linearization of the former parameter, mean hydrodynamic loads are not captured which affects the evaluation of the mean position of the platform. Consequently the dynamics of the mooring lines, which relies a lot on the the position of the floater, cannot be assessed correctly. Furthermore, the mooring system in the present model does not feature any damping property.

In the wave frequency region, the agreement between SIMA and the linear model is really good; this was however expected since the modelling process for the wave excitation in both models are strictly the same.

The third corresponds to the displacement in surge induced by pitch motion (in other word the coupling between the two motions). It is captured by the two models, with an overestimation again for the linear model, due to a lack of aerodynamic damping associated with a too simple controller.

Pitch Figure 35 displays the pitch spectra. As for surge, three peaks are recorded. A first one close to $0.05\,\mathrm{rad\,s^{-1}}$, due to wind excitation and corresponding to the pitch angle induced by surge motion (coupling pitch-surge); this time, it is almost the largest peak. A second peak is present at pitch natural frequency, excited by wind (the very eastern part of the wind spectrum). Finally, the third peak, due to waves, is found around waves peak frequency.

Again, the agreement between SIMA and the linear model at wave frequency is very well assessed. As for the coupling surge-pitch at pitch natural frequency observed in the surge spectra, the peak at pitch natural frequency is overestimated by the linear model; again, the amplitude of the peak depends mostly on the gains for the PI controller of the collective blade pitch angle, associated with aerodynamic damping. The amplitude of this peak varies significantly with the environmental conditions, and more specifically the wind speed: indeed, the lower the wind speed, the narrower the width of the wind spectrum (see 41). Thus, for EC1, the excitation is not as important as for EC2 and EC3. It is interesting to notice that for D2, this peak – located at $0.316\,\mathrm{rad\,s^{-1}}$ as seen in 9 – merges with the wave excitation, leading to a trough in the spectrum at $\omega_p = 0.47\,\mathrm{rad\,s^{-1}}$. The result is a sort of equivalent excitation at a frequency located in-between pitch natural frequency and wave peak frequency.

The first peak is acceptably evaluated by the linear model, with a little overestimation however. One could notice that this peak almost does not exist with condition EC3. The reason for it is that for these environmental conditions, the dynamic part of surge is much lower that for the two other conditions, as seen in figure 34.

Bending moment The spectra for the bending moment at the tower base, available in figure 36 differ significantly from the first two ones (surge and pitch). They feature a large number of peaks which will be interpreted and discussed. Most of the energy content of the spectrum is located at wind frequencies.

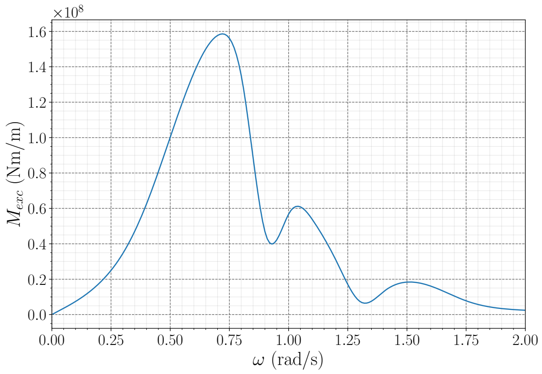

Figure 40: Wave excitation moment for design D1.

A first peak is observed at pitch natural frequency; for conditions EC2 and EC3, this peak is one of the two largest. It is associated with the pitch motion of the platform, which will generate acceleration in the tower and therefore a moment at its base. Again, because of underestimated aerodynamic damping, this peak is larger for the linear model than for SIMA.

In each case, a series of three peaks follows, corresponding to the contribution of waves to the bending moment. This contribution is highlighted in figure 40 which displays the excitation moment from diffraction-radiation. Their amplitude depend on the combination (D,EC).

The variation of the pressure close to the tower due to the periodic rotation of the blades is responsible for the excitation of the bending moment at $\omega_{3P} = 3\omega_{1P}$. This one is overestimated by the linear model, as explained in Hegseth et al. (2020b). For EC1, the peak at 6P is also visible, right before the largest peak at tower natural frequency, excited by some residual energy from either the 3P or the 6P excitations (see figure 37 at these frequencies). Even though this peak is captured by both models, it is largely exagerated by the linear model. The reasons for it are:

- the excitation loads at 3P are overestimated;
- the controller does not feature any damper for the tower mode;
- the connection between the floater and the tower is assumed perfectly rigid while for large values of the bending moment, deformations need to be accounted for;
- no structural damping has been taken into account when modelling the tower.

One should notice that designs D2 and D3 feature a natural period for the tower mode close to the 6P frequency for condition EC1, which gives rise to a larger response than for EC2 and EC3.

Thrust force The thrust force (figure 37) has logically most of its energy in the wind frequency region. The motions of the platform contribute to an increase in

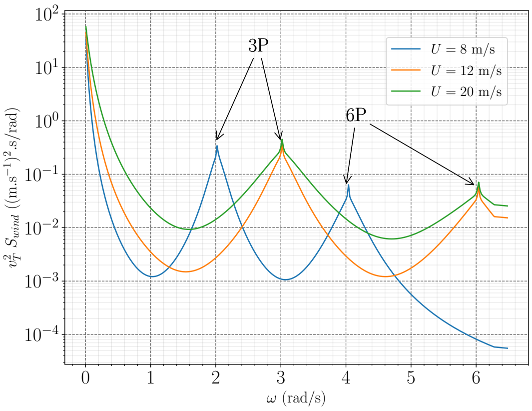

Figure 41: Effective wind spectra for the three environmental conditions

the thrust, hence the peaks at pitch natural frequency and waves peak frequency. These peaks are mostly visible for EC3 since the excitation due to wind has a lower order of magnitude: indeed, for $U = 20\,\mathrm{m\,s^{-1}}$, in order to maintain a constant power output (cf 22), thrust is significantly reduced compared to rated and close to be rated conditions. The pressure variation due the rotation of the blades is also responsible for an increase in the thrust at 3P. Again, because of an overestimation of pitch motion at pitch natural frequency, the thust force at this frequency is not well captured.

Blade pitch angle As implemented in the control part, for below rated wind speeds, the blade pitch angle is kept constant (figure 38). For above rated ones, all the energy is located at wind frequency. One can notice that the pitch actuators are more used close rated power than significantly above by comparing the orders of magnitude for EC2 and EC3. For EC2, the pitch controller is slightly affected by the surge motion of the platform, which modifies the wind speed seen by the rotor. This phenomenon is captured by both models. In total, the agreement between SIMA and the linear model is good.

Rotor speed As for the blade pitch angle, the excitation for the rotor speed (figure 39) comes mostly from wind, with however a small contribution from waves for EC3. Again, close to rated wind speed, the variations are larger than for $U = 20\,\mathrm{m\,s^{-1}}$, where the state is more steady.

5.3 Exploration of the design space

A prerequisite to any optimization attempt is the analysis of the system, its objective function and constraints, in the space defined by the chosen design variables. In the current model, this design space is the plane $(D_{OC,top}, L_{pont})$. Figure 42 displays the distribution of the mass of steel used in the floater over this space. Logically, the larger the design the heavier, so the objective is to get good performances of the floater while keeping its mass reasonably low.

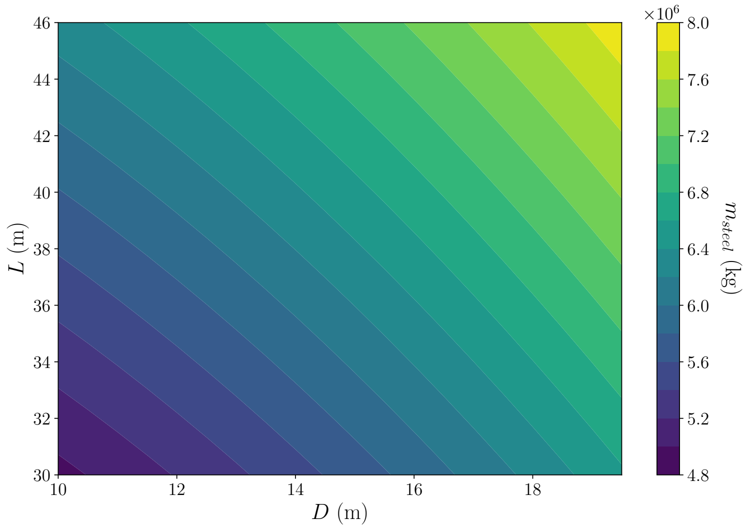

Figure 42: Mass of steel over the design space

Apart from the objective function – the mass of steel – the main variables of interest will be the expected three-hour maximum values for surge, pitch as well as for the tower base bending stress. Assuming that these processes are stationary, normally distributed and narrow-banded, their expected three-hour maximum amplitude are accessed via:

$$X_{3h} = \underbrace{\sqrt{m_{0,X}}}_{\hat{X}=\sigma_X} \left[\sqrt{2\log N_{3h}} + \frac{0.5772}{\sqrt{2\log N_{3h}}} \right] + \underbrace{X_0}_{\bar{X}}, \tag{5.1}$$

where X_0 is the mean value of X and N_{3h} the number of individual maxima in three hours in the response for X. It is obtained with

$$N_{3h} = \frac{T_{3h}}{T_z} = \frac{10800}{2\pi\sqrt{m_{0,X}/m_{2,X}}}, \tag{5.2}$$

$m_{i,X}$ defining the i-th moment of the response spectrum as defined in equation 4.95.

The mean values are accessed solving static equilibrium:

$$X_0 = \overline{\mathbf{K}}^{-1} \left(\overline{\mathbf{T}}_0 + \overline{\mathbf{F}}_{D,0} \right) \tag{5.3}$$

where all the parameters were defined previously.

In the case of the axial stress in the tower, the normal stress component N/A – N being defined in 4.24 and A being the local cross section of the tower – needs to be added to the mean value from 5.3

As the properties of the system response vary with the excitation, the exploration is performed for different environmental conditions, which are stored in table 8.

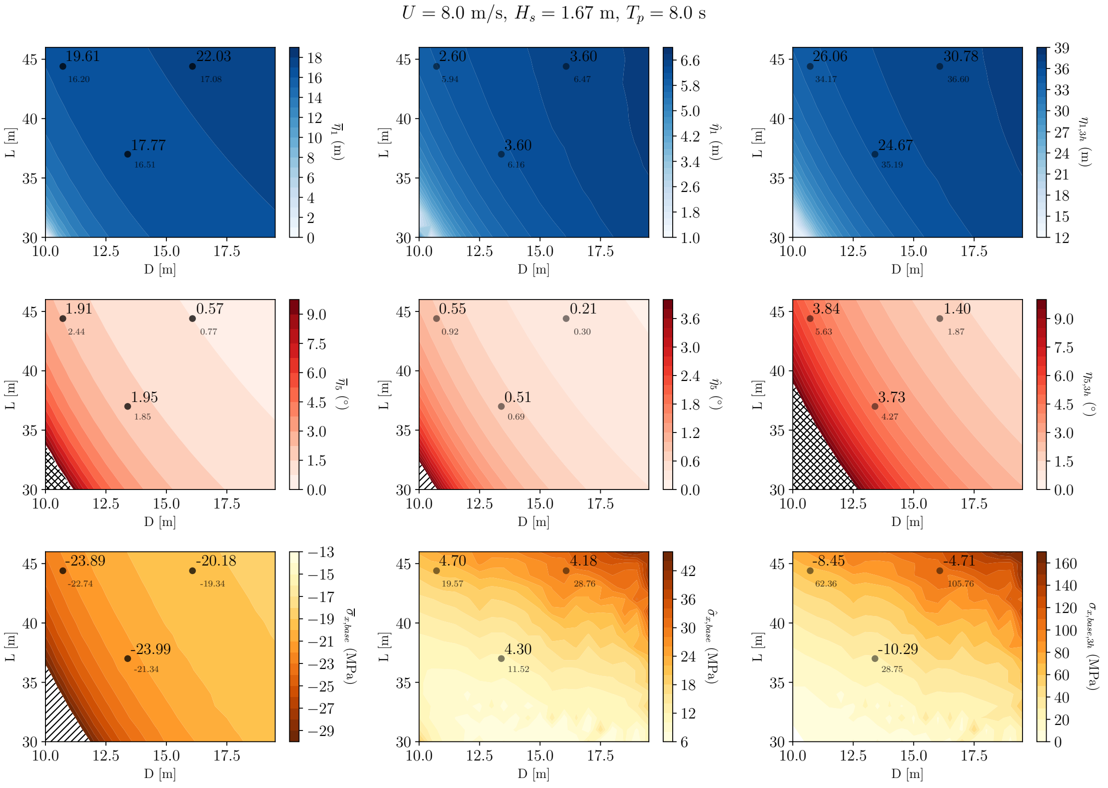

Figure 43: Design space analysis for EC1. Mean values in the first column, standard deviations in the central one, expected maximum three hour value on the right.

For each condition, the mean value, standard deviation and three-hour expected maximum value for surge, pitch and tower base bending stress are represented. The values obtained with SIMA are added to the graphs for the three designs reported in table 9; for conveniency, the corresponding value from the linear model is added in small characters. The areas for which linear theory is no longer valid due to excessively large values (mostly for pitch) are hashed with 'x' symbols; those out of scope are hashed with '/' symbols.

First, in terms of mean values, the larger the design, the larger its displacement in surge, the smaller its rotation in pitch and consequently the smaller the mean stress at the tower base. These trends follow what one could expect. Furthermore, comparing these trends between the three environmental conditions, the mean values are largest for the close to be rated condition EC2 where the thrust on the rotor reaches its maximum; then the results for EC1 are slightly larger than the ones for EC3, which is in agreement with the magnitude of the thrust force on the rotor for these wind speeds, as illustrated by figure 46.

The agreement between SIMA and the linear model is quite good for pitch and bending stress where the trends between the three designs are pretty much captured; nonetheless, a mismatch between the trends for designs 1 and 3 is often observed. For these two variables, the linear model tends to overpredict the mean response. Small designs will logically feature a larger mean pitch angle, and therefore a larger absolute value of the tower base bending stress since the arm of the

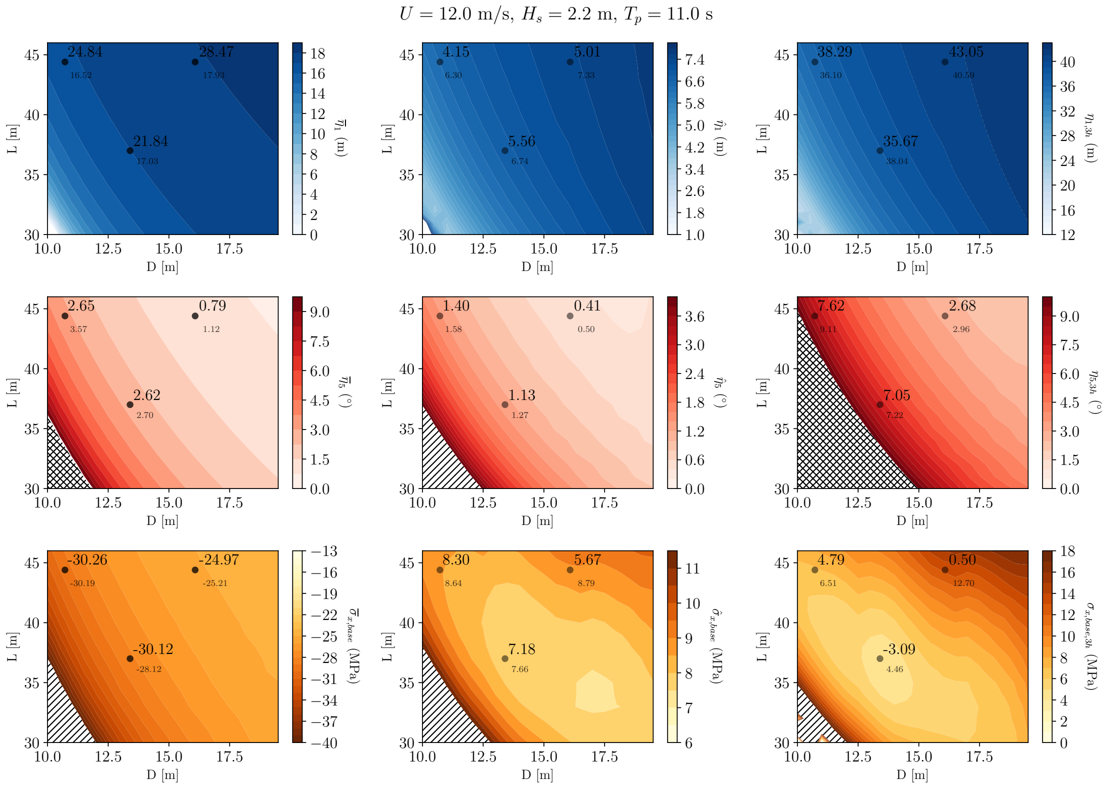

Figure 44: Design space analysis for EC2

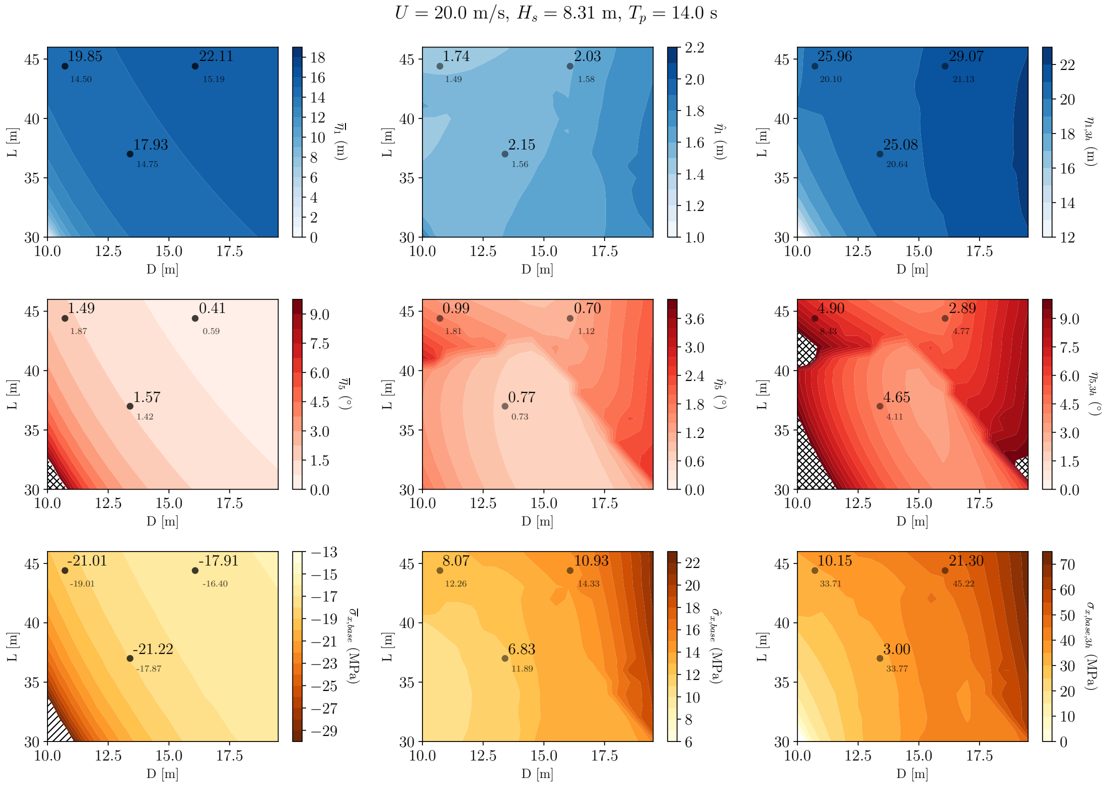

Figure 45: Design space analysis for EC3

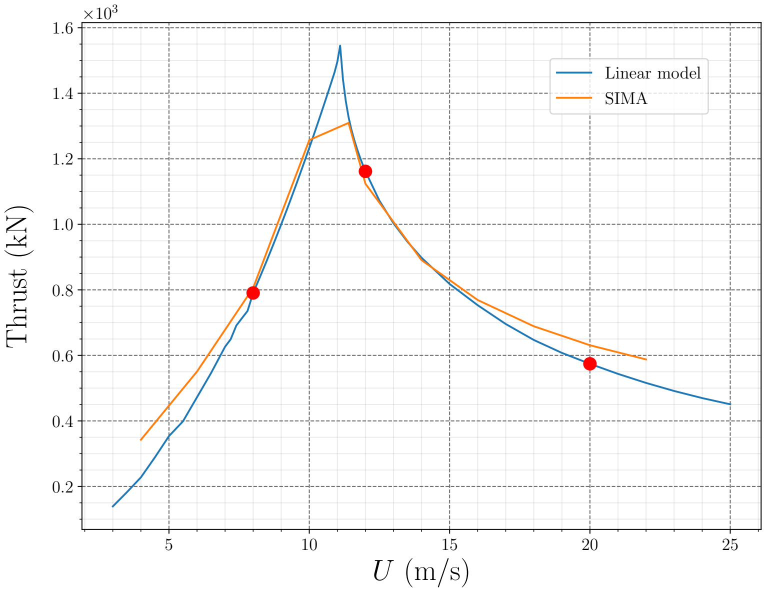

Figure 46: Thrust force on the rotor versus wind speed. The red dots are placed at the three environmental conditions elected for this analysis.

moment associated with the nacelle weight is increased. For surge, a more significant shift is observed between SIMA and the model which underestimates the response: designs D1 and D3 are considered as equivalent by the latter, while SIMA predicts an increased displacement for D3. This is probably connected to mean viscous loads, not included in the model due to linearization of the drag force: for D3, the frontal area of the floater is increased by 8.2% compared to D1, which would result in larger mean loads. In addition to this, the formulation of the mooring stiffness only accounts for the mean position due to wind, while for severe conditions like EC3, the viscous term shall contribute significantly to the mean position. However, one should keep it mind that surge is not the limiting motion in general (even though it matters notably for the design of the mooring lines), compared to pitch.

The focus will now be on the standard deviations. For the first two environmental conditions EC1 and EC2, the trends are comparable to the ones observed for the mean values: large designs lead to large displacements in surge and smaller responses for pitch and bending stress. The case of condition EC3 will be dealt with afterwards.

The evaluation of surge is again not really accurate; this time it is associated with the simplified model for the mooeing system, which does not account for dynamic effects linked to the floater frequency dependent position. For the first two environmental conditions, the standard deviation is overestimated while it is slighty underestimated for EC3: this is in agreement with figure 34, where large peaks are observed for EC1 and EC2 but smaller ones are displayed for EC3. Indeed, the inertia of design D2 is significantly larger than the ones from designs D1 and D3, which tends to reduce the amplitude of the variations around the mean position.

The assessment of pitch standard deviation is in turn pretty good but still slightly overestimated as the peaks in figure 35 suggest. The reasons for this were already explained in section 5.2.2: they are mostly connected to aerodynamic damping,

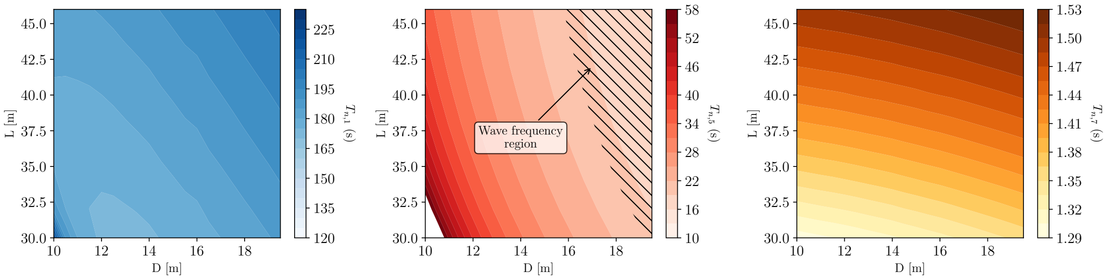

Figure 47: Natural periods over the design space

which is not sufficiently well modelled. The very large peak in the bottom right corner in figure 35 is actually part of a whole area in the neighbourhood of ($D = 11\,\mathrm{m}, L = 42\,\mathrm{m}$) with larger values than the adjacent regions, as displayed in figure 45. This pattern has been shown to be correlated to the specific wind speed $U = 20\,\mathrm{m\,s^{-1}}$ and appears to be very sensitive to variations of the PI gains. Under these conditions, the controller properties are found to be

$$\begin{aligned} T_{n,c} &= 2\pi/\sqrt{\frac{k_i \dfrac{\partial Q_A}{\partial \theta}(U=20)}{I_d}} = 48.40\,\mathrm{s} \\ \xi_c &= \frac{k_p \dfrac{\partial Q_A}{\partial \theta}(U=20) T_{n,c}}{4\pi I_d} = 0.90. \end{aligned}$$

Its natural period in the considered area is larger than the one for pitch (see figure 47), which excludes an instable behaviour resulting from a controller being too fast compared to pitch motion.

In the case of condition EC3, one should notice that the pattern features large values for large designs, which was not observed with the two other conditions. This is connected to the wave period which matches the floater natural period for large designs, as illustrated in figure 47.

As for the bending stress, the standard deviations are too large compared to SIMA, mostly for conditions EC1 and EC3 where the tower response is overamplified by the model as shown in figure 37. For condition EC2, this overestimation being less stressed, the agreement is better. For condition EC3, the trends are correctly captured at least, and in connection with pitch motion, large designs lead to increased values for stress. The same trend is given by the model for EC1 and EC2; this is linked to the fact that large designs feature lower natural periods for the bending mode, which are then more excited by the 3P peak of the wind spectrum. SIMA however predicts lower values for design D2. Again, this mismatch stems from the overestimation of the amplitude of the tower mode, associated with the too large values for the 3P excitation mostly and the lack of built-in tower damping in the controller.

The expected maximum three hour values are mostly driven by the standard de-

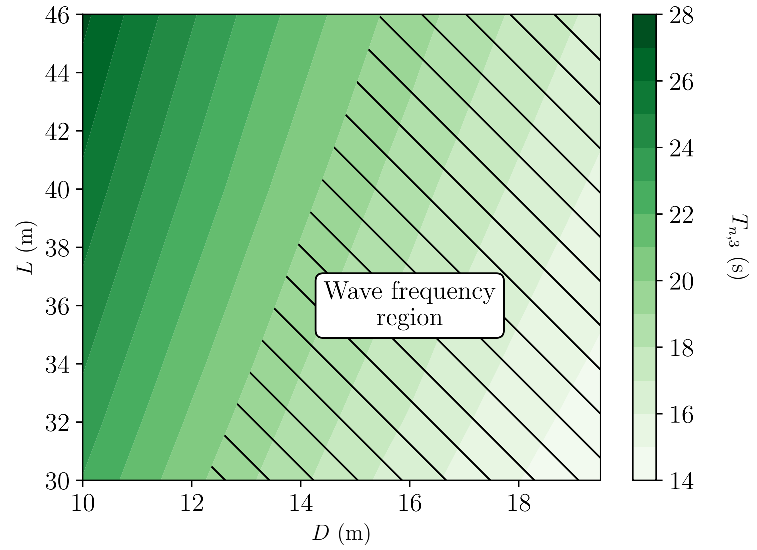

Figure 48: Heave natural period over the design space

viations, with some adjustments due to the mean values, as expressed in equation 5.3.

Another important parameter for the design of the platform is its natural frequency in heave, which needs to be pushed away from the wave frequency region. Even though heave is not included in the model, its natural period can be easily accessed by

$$T_3 = 2\pi\sqrt{\frac{\rho_w g \nabla + A_{33}(\omega_3)}{K_{33}}}. \tag{5.4}$$

Its computation is made iteratively so that the frequency at which the added mass in heave A_{33} is evaluated is equal to the natural frequency in heave. Figure 48 shows the value of T_3 over the design space, with a hashed region corresponding to the wave frequency range.

Due to the overestimation of the tower bending moment, the fatigue analysis has not been performed since it was leading to unrealistic values.

5.4 Some optimization attempts

For the sake of illustrating the optimization process, some runs have been performed with a simplified aerodynamic model, depicted in section 4.3.1. This has required to provide every single derivative with regards to the variables which depend on either $D_{OC,top}$ or L_{pont}.

The optimization was performed with environmental conditions EC1 and with two inequality constraints, on the expected three hour maximum values for surge and

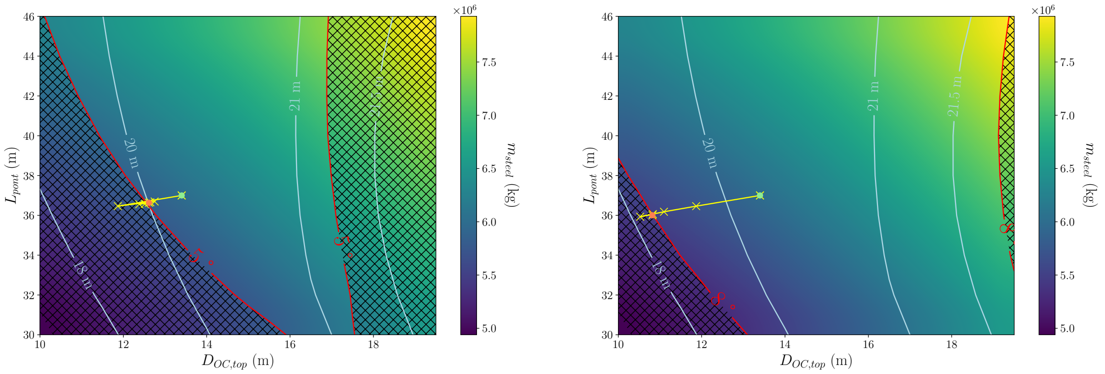

(a) $\eta_{5,3h} \leq 5°,\ \eta_{1,3h} \leq 20\,\mathrm{m}$

(b) $\eta_{5,3h} \leq 8°,\ \eta_{1,3h} \leq 20\,\mathrm{m}$

Figure 49: Optimization paths for two sets of constraints. Hashed areas are the forbidden zones for pitch; blue lines are the isolines for surge.

pitch. The results are shown in figure 49. The green dot is the starting point while the orange one corresponds to the optimized design.

As one can see in this simple case and for this set of constraints, the constraint on pitch is the most limiting one. In the first case (figure 49a), both constraints are active, while in the second case (figure 49b) only the constraint on pitch is. Case two leads to a lighter design but of course other parameters including the mean positions, the bending stress and rotor speed standard deviation needs to be assessed. Furthermore, a complete set of environmental conditions would be required.

The ultimate developments in the linear model proposed in this report would allow one to perform some optimization runs with the complete model. These were not executed due to lack of time.

6 Conclusion and recommendations for further work

In this report, a few theoretical aspects and recommended practices relevant for the design of FWTs were first reviewed. These aspects notably include a background to perform design optimization. A first illustrative attempt was made on a simple spar model, previously defined by de Renty (2020), with a good behaviour of the process for two design variables only.

The floater OO-Star has been introduced and its linearized physical model inspired by the work from Hegseth (2020) has been explained in details. It notably features automated hydrodynamic computations, validated against WAMIT, and an aerodynamic model relying on an effective wind speed formulation.

Validations on the response in surge, pitch and bending have been performed against a high-fidelity model in SIMA. The models has shown a good potential in the assessment of the motions of the system, with some inaccuracies to tackle however.

- The linearization of the hydrodynamic viscous effects results in a bad evaluation of the surge mean value.
- The simplified controller is not able to provide enough aerodynamic damping, leading to overestimations in the dynamic pitch angle.
- The mooring system , modelled with a stiffness matrix, function of the wind speed, does not capture dynamic effects due to floater motions. This leads to errors in the assessment of the dynamic variations of surge.
- The effective wind speed formulation overestimates the magnitude of the 3P excitation, leading to an overwhelming response of the first tower bending mode, which would also benefit from an implementation of a damping feature in the controller as well as from accounting for structural damping.

The exploration of the design space which has followed, relying on two geometrical design variables, has displayed good characteristics with the same limitations as exposed above. It has notably helped identifying critical regions for the design, where the pitch angle would go beyond the threshold for the validity of linear theory.

The stage of development of this tool is still to early to use it for actual design purposes in an engineering office but a few improvements could make it really interesting for the first conception steps of any new design.

As future work, one could try to solve the issues previously mentioned, with a specific focus on the controller. An accurate fatigue analysis would be feasible once the preditction of the tower bending stress is made more realistic. It would also be interesting to add some design variables (the first one being the draft of the platform), before actually performing optimization runs. Ultimately it would be a great improvement to build a generic tool which would be able to process any floater geometry, specified as an input.

Bibliography

Ang, A. (2019). Matrix derivative on matrix function of matrix variable. https://angms.science/.

A.Pegalajar-Jurado, F.J.Madsen, M.Borg, and H.Bredmose (2018). State-of-the-art models for the two LIFES50+ 10MW floater concepts. Technical report, DTU.

Ashuri, T., Zaaijer, M., Martins, J., van Bussel, G., and van Kuik, G. (2014). Multidisciplinary design optimization of offshore wind turbines for minimum levelized cost of energy. *Renewable Energy*, 68:893 – 905.

Ashuri, T., Zaaijer, M. B., Martins, J. R., and Zhang, J. (2016). Multidisciplinary design optimization of large wind turbines—technical, economic, and design challenges. *Energy Conversion and Management*, 123:56–70.

Bachynski, E. E. and Moan, T. (2012). Design considerations for tension leg platform wind turbines. *Marine Structures*, 29(1):89 – 114.

Benveniste, G., Lerch, M., de Prada, M., Kretschmer, M., Berqué, J., López, A., and Pérez, G. (2016). LCoE tool description, technical and environmental impact evaluation procedure. Technical report, IREC.

Butterfield, S., Musial, W., Jonkman, J., and Sclavounos, P. (2005). Engineering challenges for floating offshore wind turbines. *Copenhagen offshore wind conference.*

Chew, K.-H., Tai, K., Ng, E., and Muskulus, M. (2015). Optimization of offshore wind turbine support structures using an analytical gradient-based method. *Energy Procedia*, 80:100 – 107. 12th Deep Sea Offshore Wind R&D Conference, EERA DeepWind'2015.

de Renty, B. (2020). Gradient-based design optimization of a semi-submersible floating wind turbine.

Dirlik, T. (1985). Application of computer in fatigue analysis.

DNV-GL (2014). Dnv-rp-c203: Fatigue design of offshore steel structures. Technical report.

Faltinsen, O. M. (1993). *Sea Loads on Ships and Offshore Structures.* Cambridge University Press.

Fylling, I. and Berthelsen, P. A. (2011). WINDOPT: An optimization tool for floating support structures for deep water wind turbines. *Ocean Space Utilization; Ocean Renewable Energy*, 5:767–776.

G.F.Clauss and L.Birk (1996). Hydrodynamic shape optimization of large offshore structures. *Marine Structures.*

Gill, P., Murray, W., and Saunders, M. (2002). Snopt: An sqp algorithm for large-scale constrained optimization. *SIAM Journal on Optimization*, 12:979–1006.

Halfpenny, A. (1998). *Dynamic analysis of both on and offshore wind turbines in the frequency domain.* PhD thesis, University of London.

Hansen, M., Anca, D., Larsen, T., Stig, O., Sorensen, P., and Fuglsang, P. (2005). Control design for a pitch-regulated, variable speed wind turbine.

Hansen, M. and Henriksen, L. (2013). *Basic DTU Wind Energy controller.* Number 0028 in DTU Wind Energy E. DTU Wind Energy, Denmark.

Hansen, M. O. (2015). *Aerodynamics of Wind Turbines: third edition.* Earthscan, 3 edition.

Hegseth, J. M. (2020). *Efficient Modelling and Design Optimization of Large Floating Wind Turbines.* PhD thesis, NTNU.

Hegseth, J. M., Bachynski, E. E., and Martins, J. R. (2020a). Integrated design optimization of spar floating wind turbines. *Marine Structures*, 72.

Hegseth, J. M., Bachynski, E. E., and R.R.A.Martins, J. (2020b). Integrated design optimization of spar floating wind turbines. *Marine Structures 72.*

Häfele, J. and R.Rolfes (2016). Approaching the ideal design of jacket substructures for offshore wind turbines with a particle swarm optimization algorithm.

(IEC), I. E. C. (2014). Iec 61400-1 wind turbines – part 1: Design requirements. Technical report.

J.Jonkman, S.Butterfield, W.Musial, , and G.Scott (2009). Definition of a 5-mw reference wind turbine for offshore system development. Technical report, NREL.

J.M.Jonkman and D.Matha (2011). Dynamics of offshore floating wind turbines—analysis of three concepts. *Wind Energy*, 14(4):557–569.

Karimi, M., Hall, M., Buckham, B., and Crawford, C. (2017). A multi-objective design optimization approach for floating offshore wind turbine support structures. *Journal of Ocean Engineering and Marine Energy*, 3:69–87.

Krieger, A., Ramachandran, G. K. V., Vita, L., Alonso, P. G., Almería, G. G., Berque, J., and Aguirre, G. (2015a). Deliverable d7.2: Design basis. Technical report.

Krieger, A., Ramachandran, G. K. V., Vita, L., Alonso, P. G., Almería, G. G., Berque, J., and Aguirre, G. (2015b). Design basis. Technical report, DNVGL,IBER,TECNA.

Lambe, A. and Martins, J. (2012). Extensions to the design structure matrix for the description of multidisciplinary design, analysis, and optimization processes. *Structural and Multidisciplinary Optimization.*

Lemmer, F., Müller, K., Yu, W., Schlipf, D., and Cheng, P. W. (2017). Optimization of floating offshore wind turbine platforms with a self-tuning controller. *Ocean Renewable Energy*, 10.

Molin, B. (2002). *Hydrodynamique des Structures Offshore*. Technip, Paris.

Ning, A., Hayman, G., Damiani, R., and Jonkman, J. M. (2015). *Development and Validation of a New Blade Element Momentum Skewed-Wake Model within AeroDyn*.

Park, Y., Jang, B.-S., and Kim, J. D. (2015). Hull-form optimization of semi-submersible fpu considering seakeeping capability and structural weight. *Ocean Engineering*, 104:714 – 724.

Perez, R. and Perez, M. (2015). *A Fundamental Look At Supply Side Energy Reserves For The Planet*. International Energy Agency (IEA).

Sandner, F., Schlipf, D., Matha, D., and Cheng, P. W. (2014). Integrated optimization of floating wind turbine systems. *Ocean Renewable Energy*, 9B.

Thiagarajan, K. P. and Dagher, H. J. (2014). A review of floating platform concepts for offshore wind energy generation. *Journal of Offshore Mechanics and Arctic Engineering*, 136(2). 020903.

T.J.Larsen and T.D.Hanson (2007). A method to avoid negative damped low frequent tower vibrations for a floating, pitch controlled wind turbine. *Journal of Physics: Conference Series*, 75:012073.

Tracy, C. (2007). Parametric design of floating wind turbines.

Yu, W., Müller, K., and Lemmer, F. (2018). Public definition of the two LIFES50+ 10MW floater concepts. Technical report, USTUTT.